UNIVERSIDADE DE BRASÍLIA
FACULDADE DE TECNOLOGIA
DEPARTAMENTO DE ENGENHARIA CIVIL E AMBIENTAL

ANÁLISE DE GATILHOS DE LIQUEFAÇÃO ESTÁTICA EM BARRAGENS DE REJEITO: DA RUPTURA À DESCARACTERIZAÇÃO

ERICK RÓGENES SIMÃO SOARES

ORIENTADOR: DR. LEANDRO LIMA RASMUSSEN

TESE DE DOUTORADO EM GEOTECNIA

PUBLICAÇÃO: G.TD-208/2025

BRASÍLIA/DF: SETEMBRO/2025

UNIVERSIDADE DE BRASÍLIA
FACULDADE DE TECNOLOGIA
DEPARTAMENTO DE ENGENHARIA CIVIL E AMBIENTAL

ANÁLISE DE GATILHOS DE LIQUEFAÇÃO ESTÁTICA EM BARRAGENS DE REJEITO: DA RUPTURA À DESCARACTERIZAÇÃO

ERICK RÓGENES SIMÃO SOARES

TESE DE DOUTORADO SUBMETIDA AO DEPARTAMENTO DE ENGENHARIA CIVIL E AMBIENTAL DA UNIVERSIDADE DE BRASÍLIA COMO PARTE DOS REQUESITOS NECESSÁRIOS PARA A OBTENÇÃO DO GRAU DE DOUTOR

APROVADA POR:

_____
LEANDRO LIMA RASMUSSEN, Dr. (UnB)
(ORIENTADOR)

_____
ANDRÉ PACHECO DE ASSIS, Dr. (UnB)
(EXAMINADOR INTERNO)

_____
ALOMIR H. FÁVERO NETO, Dr. (BUCKNELL UNIVERSITY)
(EXAMINADOR EXTERNO)

_____
BRUNO GUIMARÃES DELGADO, Dr. (UFOP)
(EXAMINADOR EXTERNO)

DATA: BRASÍLIA/DF, 01 DE SETEMBRO DE 2025.

FICHA CATALOGRÁFICA

RÓGENES, ERICK
Análise de gatilhos de liquefação estática em barragens de rejeito: da ruptura à descaracterização [Distrito Federal] (2025)
xviii, 120 p., 297 mm (ENC/FT/UnB, Doutorado, Geotecnia, 2025)
Tese de Doutorado – Universidade de Brasília. Faculdade de Tecnologia.
Departamento de Engenharia Civil
2. Constitutive Modeling 2. CASM
4. NorSand 4. Static Liquefaction
II. ENC/FT/UnB II. Doutor

REFERÊNCIA BIBLIOGRÁFICA

RÓGENES, E. (2025). Análise de gatilhos de liquefação estática em barragens de rejeito: da ruptura à descaracterização. Tese de Doutorado, Publicação (G.TD-208/2025), Departamento de Engenharia Civil e Ambiental, Universidade de Brasília, Brasília, DF, 120 p.

CESSÃO DE DIREITOS

NOME DO AUTOR: Erick Rógenes Simão Soares
TÍTULO DA TESE DE DOUTORADO: Assessing static liquefaction in tailings dams: from failure to decharacterization
GRAU: Doutor / ANO: 2025

_____

Erick Rógenes Simão Soares
Rua do Comércio, 76, Centro
CEP 57515000 – Senador Rui Palmeira/AL - Brasil

UNIVERSITY OF BRASÍLIA
FACULTY OF TECHNOLOGY
DEPARTMENT OF CIVIL AND ENVIRONMENTAL ENGINEERING

ASSESSING STATIC LIQUEFACTION IN TAILINGS DAMS: FROM FAILURE TO DECHARACTERIZATION

ERICK RÓGENES SIMÃO SOARES

ADVISOR: DR. LEANDRO LIMA RASMUSSEN

PhD THESIS IN GEOTECHNICAL ENGINEERING

PUBLICATION: G.TD-208/2025

BRASÍLIA/DF: SEPTEMBER/2025

UNIVERSITY OF BRASÍLIA

FACULTY OF TECHNOLOGY

DEPARTMENT OF CIVIL AND ENVIRONMENTAL ENGINEERING

ASSESSING STATIC LIQUEFACTION IN TAILINGS DAMS: FROM FAILURES TO DECHARACTERIZATION

ERICK RÓGENES SIMÃO SOARES

PhD THESIS SUBMITTED TO THE DEPARTMENT OF CIVIL AND ENVIRONMENTAL ENGINEERING OF THE UNIVERSITY OF BRASÍLIA IN PARTIAL FULFILLMENT OF THE REQUIREMENTS FOR THE DEGREE OF DOCTOR

APPROVED BY:

_____
LEANDRO LIMA RASMUSSEN, Dr. (UnB)
(ADVISOR)

_____
ANDRÉ PACHECO DE ASSIS, Dr. (UnB)
(INTERNAL EXAMINER)

_____
ALOMIR H. FÁVERO NETO, Dr. (BUCKNELL UNIVERSITY)
(EXTERNAL EXAMINER)

_____
BRUNO GUIMARÃES DELGADO, Dr. (UFOP)
(EXTERNAL EXAMINER)

DATE: BRASÍLIA/DF, SEPTEMBER 1, 2025.

CATALOGING SHEET

RÓGENES, ERICK
Assessing static liquefaction in tailings dams: from failure to decharacterization [Federal District] (2025)
xix, 120 p., 297 mm (ENC/FT/UnB, PhD, Geotechnical Engineering, 2025)
PhD Thesis – University of Brasília. Faculty of Technology.
Department of Civil and Environmental Engineering.

1. Constitutive Modeling 2. CASM
3. NorSand 4. Static Liquefaction
I. ENC/FT/UnB II. Doctorate

REFERÊNCIA BIBLIOGRÁFICA

RÓGENES, E. (2025). Assessing static liquefaction in tailings dams: from failure to decharacterization. PhD Thesis, Publication (G.TD-208/2025), Department of Civil and Environmental Engineering, University of Brasília, Brasília, DF, 120 p.

COPYRIGHT LICENSE

Erick Rógenes Simão Soares
Rua do Comércio, 76, Centro
CEP 57515000 – Senador Rui Palmeira/AL - Brazil

DECLARAÇÃO DE ISENÇÃO DE RESPONSABILIDADE

É importante ressaltar que o presente trabalho tem como único objetivo ampliar o entendimento sobre a representatividade de modelos numéricos na simulação do fenômeno da liquefação estática. O estudo não tem a intenção, em nenhum momento, de determinar a causa da ruptura do caso utilizado como base, nem de questionar ou revisar as análises realizadas por painéis de especialistas que avaliaram o evento, incluindo as publicações de Arroyo e Gens (2021) e Robertson et al. (2019). Além disso, não visa definir se seria possível realizar intervenções para evitar a ruptura.

Os autores não fazem qualquer julgamento sobre a representatividade dos modelos apresentados em relação às condições reais da barragem antes ou durante o evento de ruptura. Este estudo deve ser entendido exclusivamente como uma investigação acadêmica e educacional, sem qualquer intenção de emitir declarações ou considerações sobre a responsabilidade ou as causas da ruptura da barragem. O trabalho não deve ser interpretado como base para qualquer tipo de investigação sobre a responsabilidade pelo ocorrido.

Os modelos numéricos e os resultados apresentados neste estudo são de natureza teórica e devem ser considerados exclusivamente dentro do contexto acadêmico proposto. Não devem ser utilizados por terceiros como fundamento para decisões práticas, políticas, jurídicas ou de engenharia, sem a devida avaliação de especialistas ou sem considerar o contexto real e técnico completo do evento. Em caso de qualquer uso indevido ou interpretação além do escopo acadêmico, os autores não se responsabilizam pelas consequências práticas ou jurídicas que possam decorrer dessa interpretação.

DISCLAIMER

It is important to emphasize that this work has the sole purpose of expanding the understanding of the representativeness of numerical models in simulating the phenomenon of static liquefaction. The study does not, at any point, aim to determine the cause of the failure of the case used as the basis, nor to question or review the analyses carried out by expert panels who evaluated the event, including the publications by Arroyo and Gens (2021) and Robertson et al. (2019). Furthermore, it does not aim to define whether interventions could have been made to prevent the failure.

The authors make no judgment regarding the representativeness of the models presented in relation to the actual conditions of the dam before or during the failure event. This study should be understood exclusively as an academic and educational investigation, with no intention of making any statements or considerations about the responsibility or causes of the dam failure. The work should not be interpreted as the basis for any investigation into the responsibility for the event.

The numerical models and results presented in this study are theoretical in nature and should be considered exclusively within the proposed academic context. They should not be used by third parties as the basis for practical, political, legal, or engineering decisions without the proper evaluation of experts or without considering the full real and technical context of the event. In the case of any misuse or interpretation beyond the academic scope, the authors do not assume responsibility for any practical or legal consequences that may arise from such interpretation.

DEDICATION

To the four most important people in my life: Alessandra, Henry, Neto, and Renilda.

ACKNOWLEDGMENTS

I am deeply grateful to everyone who, in some way, contributed to this important stage of my life.

To my spouse Alessandra, for her affection, companionship, and patience throughout this journey.

To my parents, Neto and Renilda, for their unconditional love and care. Without them, I would not have made it this far.

To my supervisor, Professor Leandro, for his guidance, understanding, encouragement, and availability, even outside regular working hours. Thank you also for the friendship we built along the way.

To Professor Alomir, for welcoming me so warmly and providing full support during my exchange period.

To DF+ Engenharia, for the essential support and encouragement in the development of this research.

Finally, I thank God for everything.

AVALIAÇÃO DA LIQUEFAÇÃO ESTÁTICA EM BARRAGENS DE REJEITOS: DA RUPTURA À DESCARACTERIZAÇÃO

RESUMO

A liquefação estática em barragens de rejeitos pode causar danos econômicos e ambientais severos. Após falhas recentes, cresce a necessidade de intervenções em estruturas existentes para eliminar suas características de alteamento a montante, por meio de um processo conhecido como descaracterização. No entanto, a ausência de metodologias bem estabelecidas torna incerta a eficácia dessas intervenções. Na prática, observa-se um uso crescente de modelos constitutivos capazes de representar esse fenômeno, caracterizado por um amolecimento brusco, e avaliar estruturas suscetíveis à liquefação. Diversos modelos constitutivos vêm sendo aplicados na modelagem da liquefação estática de rejeitos, mas o grau de influência da escolha do modelo nos resultados da análise ainda precisa ser esclarecido. Este estudo investiga essas incertezas por meio da retroanálise da ruptura de uma barragem de rejeitos, utilizando dois modelos constitutivos: Clay and Sand Model (CASM) e NorSand. Além de reproduzir a ruptura observada, simulações adicionais foram realizadas com gatilhos hipotéticos, como carregamento na crista e aumento da gravidade. Os resultados foram comparados quanto aos mecanismos de ruptura, trajetórias de tensões e níveis de perturbação necessários para a liquefação. Ambos os modelos geraram padrões de ruptura semelhantes, com pequenas diferenças na sensibilidade à liquefação. Os resultados indicam que o fator mais relevante na avaliação da suscetibilidade à liquefação estática é a capacidade do modelo em representar a perda súbita de resistência associada ao aumento da pressão de poros, sendo a formulação matemática específica um aspecto secundário. Com o modelo calibrado, foram avaliadas quatro estratégias de descaracterização: reforço composto por aterro estabilizador e material de confinamento (simultâneo ou não), escavação do reservatório e uma solução híbrida de reforço com escavação. As simulações foram realizadas em condições não drenadas e com acoplamento hidromecânico para avaliar efeitos do tempo. Os resultados mostram que as soluções simultâneas e híbridas foram as mais eficazes, prevenindo a liquefação mesmo em cenários de carregamento não drenado. Em contraste, a construção não simultânea e a escavação isolada resultaram em ruptura. As simulações acopladas confirmaram a viabilidade de todas as estratégias quando considerados os efeitos do tempo. Esses resultados reforçam a importância

de análises dependentes do tempo na avaliação de estratégias de descaracterização para barragens em condições críticas.

ASSESSING STATIC LIQUEFACTION IN TAILINGS DAMS: FROM FAILURES TO DECHARACTERIZATION

ABSTRACT

Static liquefaction in tailings dams can cause severe economic and environmental damage. Following recent failures, there is an increased need for interventions in existing structures to eliminate their upstream characteristics through a process known as decharacterization. However, the absence of well-established methodologies has left the effectiveness of such interventions unclear. In practice, the use of constitutive models capable of capturing this strain softening phenomenon and assessing structures susceptible to liquefaction is increasing. Numerous constitutive models exist and have been applied to model static liquefaction of tailings materials, but the extent of the influence exerted by the choice of constitutive model on analysis outcomes remains to be determined. This study investigates these uncertainties through back-analysis of a tailings dam failure, using two constitutive models: the Clay and Sand Model (CASM) and NorSand. Besides reproducing the observed failure, additional simulations tested hypothetical triggers, such as crest loading and increased gravity. Results were compared in terms of failure mechanisms, stress paths, and disturbance levels needed to trigger liquefaction. Both models produced similar failure patterns, with minor differences in liquefaction sensitivity. The findings highlight that the key factor in evaluating liquefaction susceptibility is the model's ability to capture sudden strength loss due to pore pressure buildup, while the specific mathematical formulation plays a secondary role. The calibrated model was then used to assess four decharacterization strategies: buttressing with stabilizing fill and backfill (built concurrently or not), reservoir excavation, and a hybrid buttress-excavation solution. Simulations were performed under both undrained and hydromechanically coupled conditions to assess time-dependent behavior. Results show that simultaneous buttressing and the hybrid approach were the most effective, preventing liquefaction even under extreme undrained conditions. In contrast, non-concurrent fill and backfill construction and isolated excavation triggered liquefaction. Coupled simulations confirmed the viability of all strategies when transient effects were considered. These findings underscore the importance of time-dependent analyses in the assessment of decharacterization strategies for dams in critical conditions.

TABLE OF CONTENTS

1 - INTRODUTION 1

1.1 - MOTIVATION 1

1.2 - PROBLEM 2

1.3 - OBJECTIVES 4

1.4 - THESIS ORGANIZATION 4

2 - STATIC LIQUEFACTION SIMULATION 7

2.1 - CRITICAL STATE THEORY 9

2.2 - STATIC LIQUEFACTION 12

2.3 - CONSTITUTIVE MODEL 15

2.3.1- CLAY AND SAND MODEL - CASM 18

2.3.2- NORSAND 22

2.4 - FINITE ELEMENT METHOD 25

3 - MODELING APPROACH 30

3.1 - BACK ANALYSIS AND HYPOTHETICAL TRIGGERS 32

3.2 - DECHARACTERIZATION 32

4 - PLAXIS AND CASM: IMPLEMENTATION, VERIFICATION AND CALIBRATION 36

4.1 - IMPLEMENTATION 36

4.2 - VERIFICATION 39

4.3 - PARAMETRIC ANALYSIS 42

4.4 - CALIBRATION METHODOLOGY 45

4.4.1- Step 1 - Determination of parameters M, Γ and λ 45

4.4.2- Step 2 - Determination of the elastic parameters ν and k 46

4.4.3- Step 3 - Determination of the plastic parameter – m 47

4.4.4- Step 4 - Determination of the spacing ratio - r. 48

4.4.5- Step 5 - Determination of the plastic parameter – n. 48

4.4.6- Calibration for tailing materials 49

5 - CASE STUDY: TAILINGS DAM FAILURE 54

5.1 - MODEL SETUP 55
5.1.1- TAILINGS – MECHANICAL BEHAVIOR 56
5.1.2- OTHER MATERIALS – MECHANICAL BEHAVIOR 61
5.1.3- HYDRAULIC BEHAVIOR 62
5.1.4- FINITE ELEMENT MESH AND BOUNDARY CONDITIONS 62
5.1.5- MODELING SEQUENCE 63
5.2 - PRE-FAILURE STATE 65
5.3 - LIQUEFACTION BACK ANALYSIS 66
5.3.1- CASM SIMULATION 68
5.3.2- NORSAND SIMULATION 72
6 - HYPOTHETICAL TRIGGERS 76
6.1 - DAM LOADING 77
6.2 - GRAVITY INCREASE 81
7 - DECHARACTERIZATION NUMERICAL SIMULATION 86
7.1 - MODEL SETUP 86
7.1.1- BUTTRESS STRATEGY 1 88
7.1.2- BUTTRESS STRATEGY 2 88
7.1.3- EXCAVATION 89
7.1.4- HYBRID BUTTRESS-EXCAVATION 90
7.2 - RESULTS AND DISCUSSIONS 92
7.2.1- BUTTRESS STRATEGY 1 92
7.2.2- BUTTRESS STRATEGY 2 97
7.2.3- EXCAVATION 100
7.2.4- HYBRID BUTTRESS-EXCAVATION 104
8 - CONCLUSIONS 109
8.1 - SUGGESTIONS FOR FUTURE RESEARCH 112

LIST OF TABLES

Table 2.1 – CASM parameters. 18
Table 2.2 – CASM equations. 19
Table 2.3 – Norsand parameters. 23
Table 2.4 – NorSand equations. 23
Table 4.1 – CASM parameters applied in the validation simulations. 39
Table 4.2 – Calibrated CASM model parameters. 52
Table 5.1 – CASM model parameters applied to the tailings, taken from Arroyo and Gens (2021). 56
Table 5.2 – NorSand model parameters applied to the tailings, taken from Robertson et al. (2019). 57
Table 5.3 – Mechanical parameters employed to characterize the materials of the embankment and foundation, taken from Arroyo and Gens (2021). 61
Table 5.4 – Hydraulic parameters, taken from Arroyo and Gens (2021). 62
Table 7.1 – Parameters adopted for the buttress. 87

LIST OF FIGURES

Figure 2.1 - Simplified mineral beneficiation process illustrating tailings generation as a by-product of ore production. 7
Figure 2.2 - Methods for raising tailings dams. 8
Figure 2.3 - Impact of Tailings Dam Failures: (a) tailings from the Fundão disaster reaching the Atlantic Ocean, and (b) urban areas impacted by the Jagersfontein dam failure. 9
Figure 2.4 - Typical behavior observed in dense and loose samples when sheared at the same confinement level (modify from Wood, 2004, and Laloui and Loria, 2020). 10
Figure 2.5 - Critical state line: (a) representation in the space of stress and void ratio, (b) projection in the *q-p'* plane, and (c) projection in the *e-ln(p')* plane. 11
Figure 2.6 - (a) State parameter concept, and (b) typical undrained stress path for loose and dense samples. 12
Figure 2.7 - Typical undrained stress path for samples with the same void ratio but different confining stresses, illustrating the concept of the instability line (after Andrade, 2009). 14
Figure 2.8 - Conceptual stress path to illustrate the transition from a stable to an unstable state, delineated by the instability line, caused by a liquefaction trigger (after Ledesma et al., 2022). 14
Figure 2.9 – Definition of the Reference Consolidation Line (RCL) in CASM. 20
Figure 2.10 – Effect of Lode angle variation on the CSL in the *q-p'* plane. 21
Figure 2.11 – Definition of the infinite Normal Consolidation Line (NCL) in NorSand. 24
Figure 2.12 - Flowchart of the Finite Element Method. 26
Figure 2.13 - Steps involved in the initial stiffness method for solving nonlinear problems. . 29
Figure 3.1 - Decharacterization strategies: (a) buttress, (b) excavation, and (c) hybrid buttress-excavation solution. 34
Figure 3.2 - Real-world examples of decharacterization projects: (a) Cross-section of an upstream-raised tailings dam; (b) Engineering strategy for stabilization using decharacterization fill and embankment buttresses; (c) Partial removal of tailings (modified from Neves and Felitti, 2024) 35
Figure 4.1 - Flowchart for automatic substepping integration. (after Cirone, 2020) 38
Figure 4.2 - Boundary condition and problem setup used for CASM implementation validation. 39
Figure 4.3 - Verification of CASM implementation in conventional triaxial tests. 40

Figure 4.4 - Verification of CASM implementation in isotropic compression and oedometer paths: (a) mean effective stress – axial strain, and (b) deviatoric stress - mean effective stress. 41
Figure 4.5 - Verification of CASM implementation in unloading paths followed by undrained recompression..... 41
Figure 4.6 - Verification of hydro-mechanically coupled triaxial tests using CASM: (a) deviatoric stress – axial strain, and (b) deviatoric stress – mean effective stress. 42
Figure 4.7 - Comparison of triaxial compression test results using the Cam-Clay and CASM models with $r = 2$, $n = 2$, and $m = 2$. 42
Figure 4.8 - Changes in the yield surface shape due to variations of parameters: (a) n, and (b) r. 43
Figure 4.9 - Sensitivity of CASM in undrained triaxial compression tests to variations of n: (a) deviatoric stress – axial strain, and (b) deviatoric stress – mean effective stress.. 43
Figure 4.10 - Sensitivity of CASM in undrained triaxial compression tests to variations of r : (a) deviatoric stress – axial strain, and (b) deviatoric stress – mean effective stress.. 44
Figure 4.11 - Sensitivity of CASM to variations of the parameter m in undrained triaxial compression tests..... 44
Figure 4.12 - Sensitivity of CASM to variations of the parameter m in oedometer compression tests..... 45
Figure 4.13 – (a) Plot to obtain parameter M, and (b) plot to obtain parameters Γ and λ. 46
Figure 4.14 – Graph to obtain the parameter κ. 46
Figure 4.15 – Critical State Line - p'-q plot. 49
Figure 4.16 – Critical State Line - ln(p')-v plot. 50
Figure 4.17 – Residual undrained strength..... 51
Figure 4.18 – Peak undrained strength..... 51
Figure 4.19 – Calibrated versus laboratory p'-q curves..... 52
Figure 4.20 – Calibrated versus laboratory ε_{ax}-q curves. 53
Figure 5.1 – Tailings dam failure: (a) before the failure, (b) after the failure (satellite images from Google Earth), and (c) frontal video images capturing the dam failure and flow (https://www.youtube.com/watch?v=sKZUZQytads). 54
Figure 5.2 - Dam geometry and material distribution of the case study. 55
Figure 5.3 - Numerical results for undrained anisotropic triaxial compression tests on fine tailings. 58

Figure 5.4 - Numerical and laboratory results for undrained anisotropic triaxial compression tests on mixed tailings. 58
Figure 5.5 - Numerical and laboratory results for undrained anisotropic triaxial compression tests on coarse tailings. 59
Figure 5.6 - Numerical results for oedometric compression tests. 60
Figure 5.7 - Finite element mesh. 63
Figure 5.8 - Model geometry of dam construction simulation in different stages. 64
Figure 5.9 - Pore pressure in pre-failure stage. 65
Figure 5.10 - Stress distribution in the pre-failure stage: (a) stress ratio ($\eta = q/p'$) and (b) mobilized stress ratio (η/M_θ). 66
Figure 5.11 - Details of the liquefied zone induced by drilling. 67
Figure 5.12 - Mobilized stress ratio resulting from liquefaction failure triggered by the borehole using CASM. 69
Figure 5.13 - Evolution of state parameter due to liquefaction failure triggered by the borehole using CASM: (a) initial condition and (b) failure condition. 70
Figure 5.14 - Numerical results of liquefaction failure triggered by the borehole using CASM: (a) incremental displacements and (b) deformed mesh scaled by a factor of 10. 70
Figure 5.15 - Local soil response to liquefaction failure triggered by the borehole using CASM: (a) fine tailings (points A, C, and D), (b) coarse tailings (point B), and mixed tailings (points E and F). Representative points are located on the failure surface (see Figure 5.14a). The coordinates of the points, in meters, are indicated in the plot legends. 71
Figure 5.16 - Numerical results of liquefaction failure triggered by the borehole using NorSand: (a) and (b) Mobilized stress ratio, and (c) incremental displacements. 72
Figure 5.17 - Evolution of state parameter due to liquefaction failure triggered by the borehole using NorSand: (a) initial condition and (b) failure condition. 73
Figure 5.18 - Local soil response to liquefaction failure triggered by the borehole using NorSand in comparison with CASM results: (a) fine tailings (points A, C, and D), (b) coarse tailings (point B), and mixed tailings (points E and F). Representative points are located on the failure surface (see Figure 5.16a and Figure 5.14c). The coordinates of the points, in meters, are indicated in the plot legends. 74
Figure 6.1 - Evolution of liquefaction failure triggered by dam loading across different calculation steps, mobilized stress ratio using CASM: (a) onset of failure, and (b) end of simulation. 77

Figure 6.2 - Evolution of liquefaction failure triggered by dam loading across different calculation steps, incremental displacements using CASM: (a) onset of failure, and (b) end of simulation. 78
Figure 6.3 - Evolution of liquefaction failure triggered by dam loading across different calculation steps, mobilized stress ratio using NorSand: (a) onset of failure, and (b) end of simulation. 79
Figure 6.4 - Evolution of liquefaction failure triggered by dam loading across different calculation steps, incremental displacements using NorSand: (a) onset of failure, and (b) end of simulation. 79
Figure 6.5 - Local soil response to liquefaction failure triggered by dam loading: (a) fine tailings (points A, C, and D), (b) coarse tailings (point B), and mixed tailings (points E and F). Representative points are located on the failure surface (see Figure 6.2b and Figure 6.4d). The coordinates of the points, in meters, are indicated in the plot legends. 80
Figure 6.6 - Evolution of liquefaction failure triggered by gravity increase across different calculation steps, results using CASM: mobilized stress ratio. (a) onset of failure, (b) intermediate stage, and (c) end of simulation. 82
Figure 6.7 - Evolution of liquefaction failure triggered by gravity increase across different calculation steps, results using CASM: incremental displacements. (a) onset of failure, (b) intermediate stage, and (c) end of simulation. 82
Figure 6.8 - Evolution of liquefaction failure triggered by gravity increase across different calculation steps, results using NorSand: mobilized stress ratio. (a) onset of failure, (b) intermediate stage, and (c) end of simulation. 83
Figure 6.9 - Evolution of liquefaction failure triggered by gravity increase across different calculation steps, results using NorSand: incremental displacements. (a) onset of failure, (b) intermediate stage, and (c) end of simulation. 84
Figure 6.10 - Local soil response to liquefaction failure triggered by gravity increase: (a) fine tailings (points A, C, and D), (b) coarse tailings (point B), and mixed tailings (points E and F). Representative points are located on the failure surface (see Figure 6.7c and Figure 6.9c). The coordinates of the points, in meters, are indicated in the plot legends. 85
Figure 7.1 - Numerical model applied for decharacterization simulations. 86
Figure 7.2 - Simulation stages for buttress strategy 1. 89
Figure 7.3 - Simulation stages for buttress strategy 2. 90
Figure 7.4 - Simulation stages for excavation of the reservoir and raises. 91
Figure 7.5 - Simulation stages for hybrid buttress-excavation strategy. 91

Figure 7.6 - Mobilized stress ratio resulting from buttress strategy 1 under undrained condition. 92
Figure 7.7 - Incremental shear strains resulting from Buttress strategy 1 under undrained condition at stage 14. 93
Figure 7.8 - Vertical displacement resulting from Buttress strategy 1 under undrained condition at Stage 14. Of note, negative values mean settlement. 94
Figure 7.9 - Mobilized stress ratio resulting from Buttress strategy 1 under hydromechanical coupled condition. 95
Figure 7.10 - Local soil response for decharacterization by buttress strategy 1: (a) undrained, (b) and (c) hydromechanical coupled. Representative points are located on the failure surface (see Figure 7.6 and Figure 7.9). The coordinates of the points, in meters, are indicated in the plot legends. 96
Figure 7.11 - Mobilized stress ratio resulting from Buttress strategy 2 under undrained condition. 97
Figure 7.12 - Vertical displacement resulting from Buttress strategy 2 under undrained condition at stage 6. Of note, negative values mean settlement. 97
Figure 7.13 - Mobilized stress ratio resulting from buttress strategy 2 under hydromechanical coupled condition. 98
Figure 7.14 - Local soil response for decharacterization by buttress: (a) and (b) undrained, and (c) hydromechanical coupled. Of note, M1 refers to the non-simultaneous reinforcement and fill, while M2 refers to the simultaneous condition. Representative points are located on the failure surface (see Figure 7.6, Figure 7.9, Figure 7.11 and Figure 7.13). The coordinates of the points, in meters, are indicated in the plot legends. 99
Figure 7.15 - Numerical results for excavation simulation under undrained condition: incremental displacements per step. 101
Figure 7.16 - Numerical results for excavation simulation under undrained condition: mobilized stress ratio. 101
Figure 7.17 - Mobilized stress ratio resulting from excavation strategy under hydromechanical coupled condition. 102
Figure 7.18 - Vertical displacement per stage induced by excavation under hydromechanical coupled condition. Of note, negative values mean settlement. 102
Figure 7.19 - Local soil response for decharacterization by excavation: (a) undrained and coupled at point A, (c) undrained (d) coupled. Representative points are located on the failure

surface (see Figure 7.16 and Figure 7.17). The coordinates of the points, in meters, are indicated in the plot legends. 103
Figure 7.20 - Numerical results for buttress at elevation 899.0 m follow by excavation: incremental vertical displacements per step. Of note, negative values mean settlement. 105
Figure 7.21 - Numerical results for buttress at elevation 899.0 m follow by excavation: mobilized stress ratio. 105
Figure 7.22 - Numerical results for buttress at elevation 910.0 m follow by excavation: mobilized stress ratio. 106
Figure 7.23 - Numerical results for buttress at elevation 910.0 m follow by excavation: vertical displacements per stage. Of note, negative values mean settlement. 107
Figure 7.24 - Local soil response for de-characterization by buttress and excavation: (a) buttress stages; (b) and (c) excavation stages. Notably, M1 refers to excavation without a buttress, M2 to a buttress at elevation 899 m, and M3 to a buttress at elevation 910 m. Representative points are located on the failure surface (see Figure 7.21 and Figure 7.22). The coordinates of the points, in meters, are indicated in the plot legends. 108

LIST OF SYMBOLS, NOMENCLATURE, AND ABBREVIATIONS

A	Area of the finite element
ANM	*Agência Nacional de Mineração*
ANCOLD	Australian National Committee on Large Dams
$[B]$	Matrix that relates displacements to strains
$[B]^T$	Matrix that relates stresses to forces
c'	Effective cohesion
C_a	Power-law CSL parameter
C_b	Power-law CSL parameter
C_c	Power-law CSL parameter
CASM	Clay and sand model
CSL	Critical state line
$[C]$	Compressibility matrix
$[C^e]$	Elastic compressibility matrix
$[C^p]$	Plastic compressibility matrix
DLL	Dynamic-link library
$[D]$	Constitutive matrix
$\{dF\}$	Nodal force increment vector
$\{dF_{ext}\}$	Nodal external force increment vector
$\{dF_{int}\}$	Nodal internal force increment vector
$\{dp'\}$	Mean effective stress increment vector
$\{dq\}$	Deviatoric stress increment vector
$\{du\}$	Nodal displacement increment vector
$\{d\sigma\}$	Stress increment vector
$\{d\varepsilon\}$	Strain increment vector
$\{d\varepsilon_p^e\}$	Volumetric elastic strain increment vector
$\{d\varepsilon_p^p\}$	Volumetric plastic strain increment vector
$\{d\varepsilon_q^e\}$	Deviatoric elastic strain increment vector
$\{d\varepsilon_q^p\}$	Deviatoric plastic strain increment vector
E	Young's modulus
E_{50ref}	Reference modulus that relates plastic straining due to primary deviatoric loading
E_{oedref}	Reference modulus that relates plastic straining due to primary compression
e	Void ratio
$e_{current}$	Current void ratio
e_{CSL}	Void ratio on the CSL
f	Yield surface
FS	Factor of safety
$FS_{Gravity}$	Factor of safety based on gravity
FS_{Load}	Factor of safety based on load
FS_{Local}	Local safety factor
G	Shear modulus
g	Plastic potential
g_a	Van Genuchten parameter
g_l	Van Genuchten parameter
g_n	Van Genuchten parameter
G_{ref}	shear modulus at the reference mean effective stress
H	Plastic hardening modulus in NorSand
h	Plastic strain component which controls the hardening law

H_p	Plastic modulus
K	Bulk modulus
K_0	Geostatic stress ratio
k_x (m/s)	Horizontal hydraulic conductivity
k_y (m/s)	Vertical hydraulic conductivity
$[K]$	Global stiffness matrix
$[K^e]$	Stiffness matrix of the finite element
M_θ	Slope of CSL in *q-p'* plane
M_{tc}	Slope of CSL in *q-p'* plane for triaxial compression condition;
M_i	Stress ratio at the image condition
m	Parameter that controls the plastic potential shape in CASM
m_s	Parameter that controls the variation of stiffness with confining stress
N	Volumetric coupling coefficient;
n_e	Parameter that controls the relationship between G and p'
n	Parameter that controls the yield function shape in CASM
OCR	over-consolidation ratio
p'	Mean effective stress
p'_0	Pre-consolidation stress
p'_{ref}	Reference mean effective stress
p_i	Mean stress in the image condition
$p_{i,max}$	Variable responsible for controlling the maximum dilatancy in NorSand
q	Deviatoric stress
r	Spacing ratio
S	Boolean that controls T_s
s	Stress variable that measures the size of the elastic domain
SRF	Strength reduction factor
S_{up}	Peak undrained strength
S_{ur}	Residual undrained strength
S_{res}	Residual degree of saturation
T_s	Additional softening term in NorSand
τ_f	Shear strength at failure
τ_{mob}	Mobilized shear strength
$UDSM$	User Defined Soil Model
V	Volume of the finite element
α	Parameter controlling the difference of M_θ between triaxial compression and extension
Γ	CSL void ratio at p' = 1 kPa, in *e-ln(p')* plane
χ_i	Dilatancy at the image condition
χ_{tc}	Dilatancy constant for triaxial compression condition
η	Ratio of the deviatoric stress to the mean effective stress
η_{IL}	η at instability line
η_{K0}	η at the K0 condition
η_L	Stress ratio limit defined by $p_{i,max}$.
κ	Slope of elastic line in *e-ln(p')* plane
λ	Slope of CSL in *e-ln(p')* plane
ϕ'	Effective friction angle
ψ	State parameter
ψ_{dil}	Dilation angle

ψ_i	State parameter at the image condition
σ'_1	Major principal stresses
σ'_2	Intermediate principal stresses
σ'_3	Minor principal stresses
σ'_n	Normal stress at the failure plane
σ'_{v0}	Initial vertical stress
ε_q	Deviatoric strain
ε_p	Volumetric strain
θ	Lode angle
ν	Poisson's ratio
γ	Unit weight

1 - INTRODUTION

This chapter introduces the context and background of the thesis, presenting the motivation behind the research, the main problems addressed, and the specific objectives pursued. It also outlines the overall organization of this thesis to guide the reader through the following chapters.

1.1 - MOTIVATION

Static liquefaction is a phenomenon where soils transition from a solid to a fluid state. This phenomenon has become a major topic in the geotechnical community, primarily due to recent failures of tailings dams, which are structures used to contain the byproducts of mining activities. Notable incidents include Mount Polley in 2014 (Morgenstern et al., 2015), Fundão in 2015 (Morgenstern et al., 2016), Cadia in 2018 (Jefferies et al., 2019), Dam 1 in 2019 (Robertson et al., 2019; Arroyo and Gens, 2021), and Jagersfontein in 2022 (Marais et al., 2024).

All the aforementioned failures share a commonality in their use of the upstream method. In this construction technique, the dam is raised in stages on top of already deposited tailings, forming a stepped structure. The upstream method is more vulnerable to failure and highly susceptible to liquefaction (Piciullo et al., 2022). Unlike earth dams, which undergo a compaction control process, upstream tailings dams construction involves the hydraulic deposition of materials, which often results in saturated and loose tailings that are susceptible to static liquefaction (Martin and McRoberts, 1999; Mánica et al., 2021). This is an important consideration, as the behavior of tailings is important for stability, since these materials are part of the dam's structural zone (Fourie et al., 2022).

With the expansion of mining activities, the number of ruptures in tailings dams has increased in recent years (Lyu et al., 2019; Owen et al., 2020). These ruptures cause extensive economic and environmental damage, as well as loss of lives. To prevent future occurrences, efforts have been made to better characterize tailings through field and laboratory tests (Viana da Fonseca et al., 2022; Wagner et al., 2023; Silva et al., 2024; Consoli et al., 2024). Additionally, advanced numerical simulations, which incorporate numerical techniques and constitutive models, have been employed to comprehensively understand the behavior of these

structures (Ledesma et al., 2021; Sun et al., 2021; Ng et al., 2022; Shuttle et al., 2022; Costa et al., 2023; Mofrad et al., 2023; Liu et al., 2024; Rógenes et al. 2024,2025; Gomes et al. 2024; Nazareth et al. 2025; Fávero et al. 2025).

1.2 - PROBLEM

Despite experimental and numerical advancements, uncertainties persist when performing static liquefaction triggering analyses. Reid et al. (2022, 2023) and Reid and Fourie (2024) discussed some of these uncertainties, including the effect of intermediate stress on the critical state line (CSL) and, consequently, on undrained strength, as well as the geostatic stress ratio (K_0), and the in-situ void ratio. These uncertainties are largely due to the lack of relevant and representative experimental data from field tests (e.g., CPTu and pressuremeter tests) and laboratory tests (e.g., triaxial, direct simple shear, and oedometer tests), which impacts the calibration of constitutive models (Jefferies and Been, 2015; Shuttle and Jefferies, 2016; Mánica et al., 2021; Arroyo and Gens, 2021; Gomes et al., 2022, 2024). In addition to uncertainties related to experimental data and calibrations, several studies also highlight the importance of selecting an appropriate constitutive model to simulate tailings behavior in liquefaction analyses (Mánica et al., 2021; Liu et al., 2024; Reid and Fourie, 2024). The uncertainty regarding the choice of constitutive model is one of the focuses of this work.

Additionally, to the undermentioned problems, given recent failures, it has become standard to assume that all tailings susceptible to liquefaction will liquefy (Ancold, 2019; Ledesma et al. 2024). Consequently, there is a pressing need to address the safety of existing upstream-raised tailings dams. In this regard, Brazilian regulations have adopted stricter criteria for dam safety, mandating the decharacterization of dams built using the upstream method due to the uncertainties related to characterizing such structures (Schaper et al. 2021; ANM, 2022). Decharacterization involves interventions in existing structures to eliminate their upstream dam characteristics, which requires either the removal of upstream raises or the construction of a new downstream structure. However, the challenge lies in the absence of well-established methodologies or strategies for dam decharacterization, leaving the true impact of such interventions largely unexplored.

To assess structures susceptible to static liquefaction, an increasingly common practice involves employing constitutive models capable of capturing brittle behavior and sudden

strength loss, such as the Clay and Sand Model-CASM (Mánica et al., 2021; Arroyo and Gens, 2021; Rógenes et al. 2024,2025; Gomes et al. 2024; Nazareth et al. 2025; Fávero et al. 2025), NorSand (Morgenstern et al., 2016; Jefferies et al., 2019; Robertson et al., 2019), Modified Pastor-Zienkiewicz (Ledesma et al., 2022), and Sanisand (Liu et al., 2024). These constitutive models have enabled the back-analysis of failure cases (Mánica et al., 2021; Liu et al., 2024; Rógenes et al. 2024; Fávero et al. 2025), assessment of vulnerability to different triggers (Ledesma et al., 2022; Rógenes et al. 2024), identification of key factors influencing liquefaction-induced failures (Reid et al., 2022), and modelling the runout of failure (Fávero et al. 2025).

Despite the range of models available, it remains uncertain how much the choice of constitutive model itself influences the results obtained in the analysis. Therefore, there is a growing interest in studies that compare constitutive models capable of accurately representing the liquefaction phenomenon. In this context, Liu et al. (2024) compared the NorSand and Sanisand models for the Fundão dam rupture case, identifying that both models produced compatible results. However, this conclusion was reached using similar calibration methods. It is recognized that the calibration process relies on interpretation and the chosen methodology, which can vary according to the selected constitutive model. Additionally, results may vary based on engineering judgment, even when the same database is used, as noted by Reid and Fourie (2024). Consequently, the question remains whether distinct constitutive models, calibrated in different ways yet still accurately representing the static liquefaction phenomenon, could yield the same failure mechanisms.

Furthermore, previous studies are limited to retroanalysis of dam failures, identification of potential liquefaction triggers, and sensitivity studies. However, there is a lack of advanced numerical analysis to simulate failure mechanisms during dam decharacterization processes. Moreover, trigger analyses are commonly conducted under undrained conditions, so the effect of time on the development of the mechanism is not incorporated into the analyses.

Given the context outlined above, the primary questions this work seeks to address are:

- **Question 1:** How does the choice of constitutive model influence the analysis?
- **Question 2:** Would it be possible to implement a decharacterization strategy without triggering static liquefaction failure?
- **Question 3:** What impact does time have on the triggering mechanisms during decharacterization?

1.3 - OBJECTIVES

To address the previously mentioned question, this study investigates the influence of constitutive model choice in static liquefaction analysis. It extends the comparisons made by Liu et al. (2024) to include CASM and NorSand models applied to the well-documented tailings dam failure in Brazil. Moreover, it compares static liquefaction analyses using calibrations developed by different researchers to represent the same material, thereby enhancing the understanding of how constitutive models affect the results. Furthermore, the comparison methodology is extended to go beyond the scope of back analysis, incorporating the vulnerability assessment methodology recently proposed by Ledesma et al. (2022).

This work also aims to provide valuable insights into the failure mechanisms that may arise from possible dam decharacterization techniques and to assess the most suitable strategy for intervening in existing upstream-raised dams. Additionally, the influence of time on the development of the liquefaction mechanism will be evaluated through hydromechanical coupling analyses.

The specific objectives of this study are summarized as follows:

- To compare the results obtained using the CASM and NorSand models in the back-analysis of a tailings dam failure;
- To extend the comparison to hypothetical triggering scenarios;
- To understand the mechanisms that may develop from different dam decharacterization interventions;
- To analyze the effect of time on the development of liquefaction mechanisms during decharacterization works.

1.4 - THESIS ORGANIZATION

This work is organized into eight chapters. Chapter 1 introduces the study by outlining the problem under investigation, the motivation for the research, and its general and specific objectives. In Chapter 2, a comprehensive literature review is provided, covering the process of tailings generation, methods of disposal in dams, and recent failures attributed to liquefaction. Additionally, it discusses the theoretical framework essential for conducting numerical analyses

of liquefaction, including the principles of critical state theory, the definition of static liquefaction, constitutive models, and numerical methods for simulating this phenomenon.

In Chapter 3, the numerical approach adopted throughout the research is presented. A tailings dam case study was used as a basis for comparing the CASM and NorSand models and assessing decharacterization strategies. These models were chosen because they were used by different panels (Robertson et al., 2019; Arroyo and Gens, 2021) to represent the behavior of the dam tailings. The analyses were conducted using the finite element software Plaxis2D (Brinkgreve et al., 2020). It is worth noting that while NorSand is available in the Plaxis library, CASM was implemented as a user-defined soil model (Rógenes et al. 2024a), the details of this implementation are presented in Chapter 4.

In Chapter 5, the back analyses of a tailings dam failure are presented, which were conducted using the CASM constitutive model, applying the methodology and parameters proposed by Arroyo and Gens (2021). For comparison, the back analysis was also performed using NorSand, employing parameters proposed by Robertson et al. (2019) to represent the same historical case.

In Chapter 6, two other analyses will be shown. These analyses were conducted through the simulation of hypothetical triggers: crest loading and gravity increase. The influence of the adopted constitutive model was analyzed through the mechanisms generated, stress paths, and levels of disturbances necessary to trigger liquefaction.

The calibrated model for the back analysis of the tailings dam failure was applied in simulations of different decharacterization strategies, which are presented in Chapter 7. Stress paths were meticulously analyzed during these simulations, and emerging failure mechanisms were thoroughly examined. Ultimately, potential failure mechanisms were identified, enabling the determination of the most effective decharacterization strategy. Furthermore, undrained and transient hydromechanical coupling analyses were compared to examine the effect of time on the development of liquefaction triggers. Finally, in Chapter 8, the conclusions and suggestions for future research are presented.

Finally, it is emphasized that the objective of this study was to compare the application of different constitutive models in representing the phenomenon of static liquefaction. Thus, the study does not aim to determine the cause of the rupture in the case study used as a basis, nor does it question the analyses previously conducted by Arroyo and Gens (2021) and Robertson et al. (2019). It is also highlighted that the authors do not make any judgment as to

whether the presented models are representative of the actual conditions of the dam before and during the failure.

2 - STATIC LIQUEFACTION SIMULATION

Mining plays a fundamental role in society by providing the essential raw materials for the production of a wide range of products. From everyday items such as cars and mobile phones to indispensable healthcare equipment like ultrasound devices and cutting-edge technologies such as rockets, mining supports various sectors of the economy. Thus, it is undeniable that this activity constitutes an essential pillar for human and technological development (Carvalho, 2017; Hodge et al., 2022).

The mining process is outlined in Figure 2.1. It involves the extraction of natural materials, such as soils and rocks (including ore and natural waste). The ore is subjected to a beneficiation process to separate the commercially valuable material, known as ore concentrate, from the economically non-viable material, referred to as tailings. Tailings, the by-products of mining, are a man-made material and must be managed in a controlled manner to minimize environmental impacts. The primary methods of tailings disposal are through dams and stockpiles (Vick, 1990; Piciullo et al., 2022).

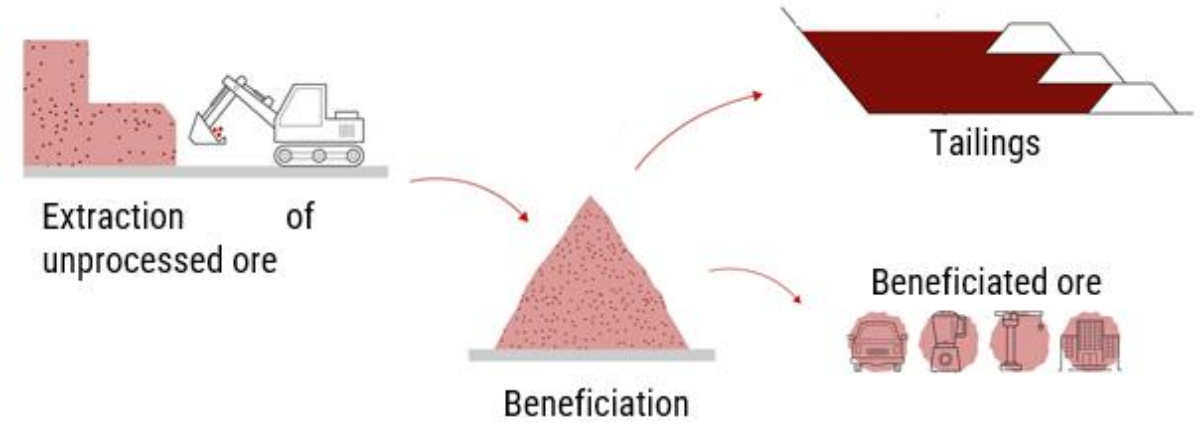

Figure 2.1 - Simplified mineral beneficiation process illustrating tailings generation as a by-product of ore production.

In the beneficiation process, water is commonly used, resulting in tailings with a high water content. As a result, disposal in dams becomes the most economical and widely adopted method. This approach eliminates the need to remove water from the material, thereby avoiding

an increase in operational costs (Vick, 1990; Williams, 2021; Cacciuttolo and Valenzuela, 2022).

The construction of tailings dams begins with the development of a starter dyke. As the reservoir fills, the structure could be raised to accommodate additional tailings. Based on the method used for these raises, tailings dams are classified into three types: upstream, centerline, or downstream, as shown in Figure 2.2 (Vick, 1990; Piciullo et al., 2022). It is also worth noting that a tailing dam can be constructed in a single phase, following a procedure like that used for constructing dams for other purposes, such as water reservoirs.

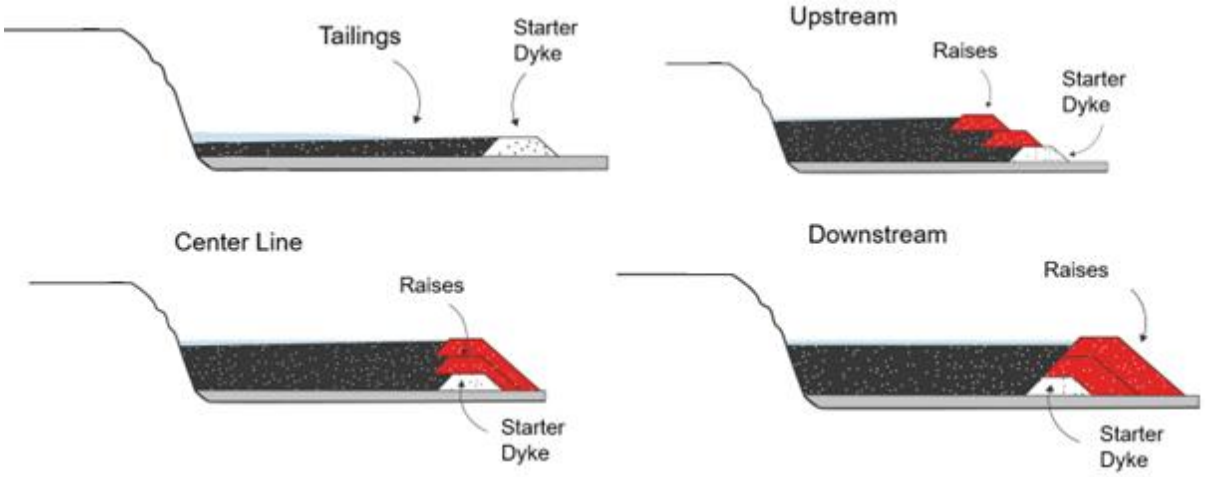

Figure 2.2 - Methods for raising tailings dams.

The upstream method is the least costly and, therefore, the most frequently used (Adamo et al., 2020; Piciullo et al., 2022). However, tailings dams constructed using the upstream method are found to be more vulnerable to failure (Piciullo et al., 2022). This vulnerability is evident due to recent failures of upstream-raised dams, such as Mount Polley in 2014 (Morgenstern et al.,2015) Fundão in 2015 (Morgenstern et al., 2016), Cadia in 2018 (Jefferies et al., 2019), Dam 1 in 2019 (Robertson et al., 2019; Arroyo and Gens, 2021), and Jagersfontein in 2022 (Marais et al. 2024). These disasters result in the loss of human lives and significant environmental impacts as shown in Figure 2.3.

All the previously mentioned cases failed due to static liquefaction, a phenomenon in which the tailings, initially in a solid state, suddenly begin to behave like a fluid. Unlike earth dams, which undergo a compaction control process, upstream tailings dams construction involves the hydraulic deposition of non-cohesive materials, which often results in saturated

and loose tailings that are susceptible to static liquefaction (Martin and McRoberts, 1999; Mánica et al., 2021).

To assess structures susceptible to static liquefaction, an increasingly common practice is to use numerical simulations, which require constitutive models capable of capturing brittle behavior and sudden strength loss that occur during static liquefaction. These constitutive models are typically based on elastoplasticity and critical state theory. The following subsections will discuss the concepts related to these analyses.

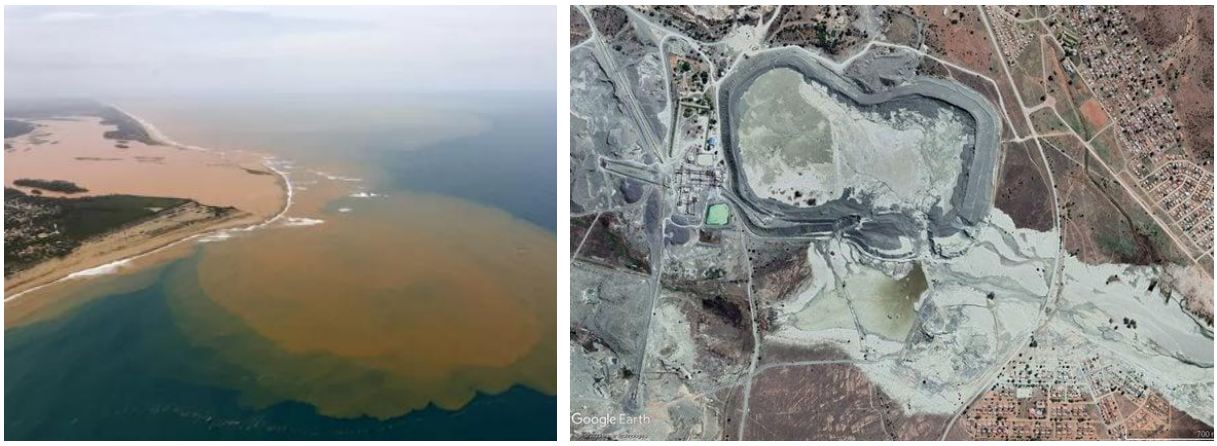

(a) (b)

Figure 2.3 - Impact of Tailings Dam Failures: (a) tailings from the Fundão disaster reaching the Atlantic Ocean, and (b) urban areas impacted by the Jagersfontein dam failure.

2.1 - CRITICAL STATE THEORY

The behavior of granular materials is strongly influenced by the initial void ratio and the stress state. Experimental observations have shown that the same material, when tested under different stress conditions and initial densities, can exhibit markedly different responses. These observations led to the development of the critical state theory (Casagrande, 1936; Roscoe et al., 1958; Schofield and Wroth, 1968; Wood, 1990; Jefferies and Been, 2015).

To illustrate this variation, consider two samples of the same material, subjected to the same stress state but with different void ratios: one in a loose condition and the other in a dense condition. The typical behavior observed is shown in Figure 2.4, where it can be seen that the loose sample tends to reduce its initial volume (i.e., contraction) and continuously gains strength until reaching a residual plateau. In contrast, the dense sample shows a tendency to expand its

initial volume (i.e., dilation), followed by a peak strength that then decreases until reaching a residual condition.

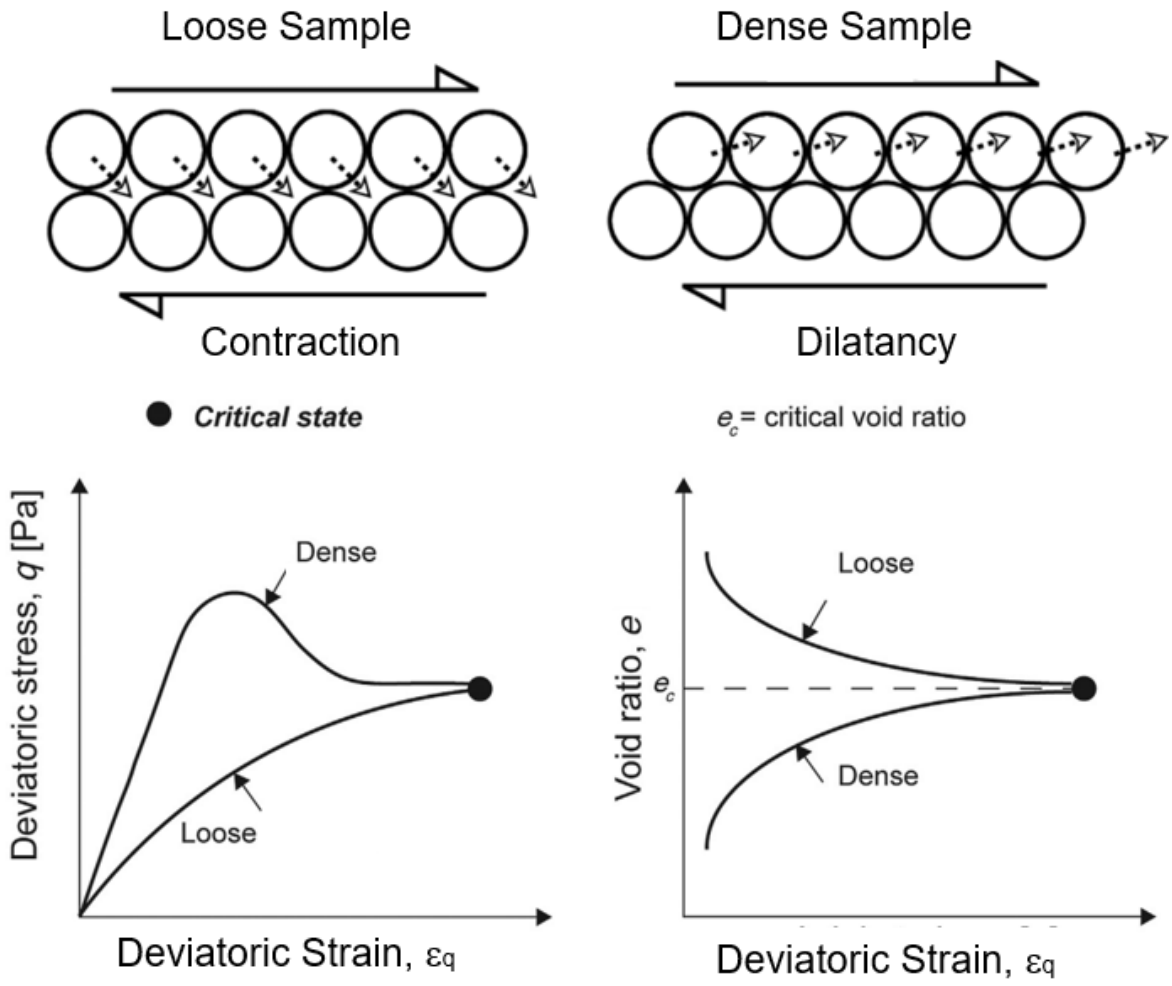

Figure 2.4 - Typical behavior observed in dense and loose samples when sheared at the same confinement level (modify from Wood, 2004, and Laloui and Loria, 2020).

It is also observed that, despite these two samples having different initial states, both ultimately reach the same condition after shearing, in terms of both stress variation and void ratio. This final condition is known as the critical state, which can be expressed by:

$$\frac{\partial p'}{\partial \varepsilon_q} = \frac{\partial q}{\partial \varepsilon_q} = \frac{\partial e}{\partial \varepsilon_q} = 0 \qquad \text{Equation 2-1}$$

where p' is the mean effective stress, q is the deviatoric stress, e is the void ratio, and ε_q is the shear strain.

The critical state theory postulates the existence of a region in the stress and void ratio space where the material reaches the critical state. This region is represented by a curve called the Critical State Line (CSL), as shown in Figure 2.5a. The projection of the CSL onto the *q-p'* and *e-ln(p')* planes can be approximated by straight lines, as illustrated in Figure 2.5b and Figure 2.5c (Wood, 1990).

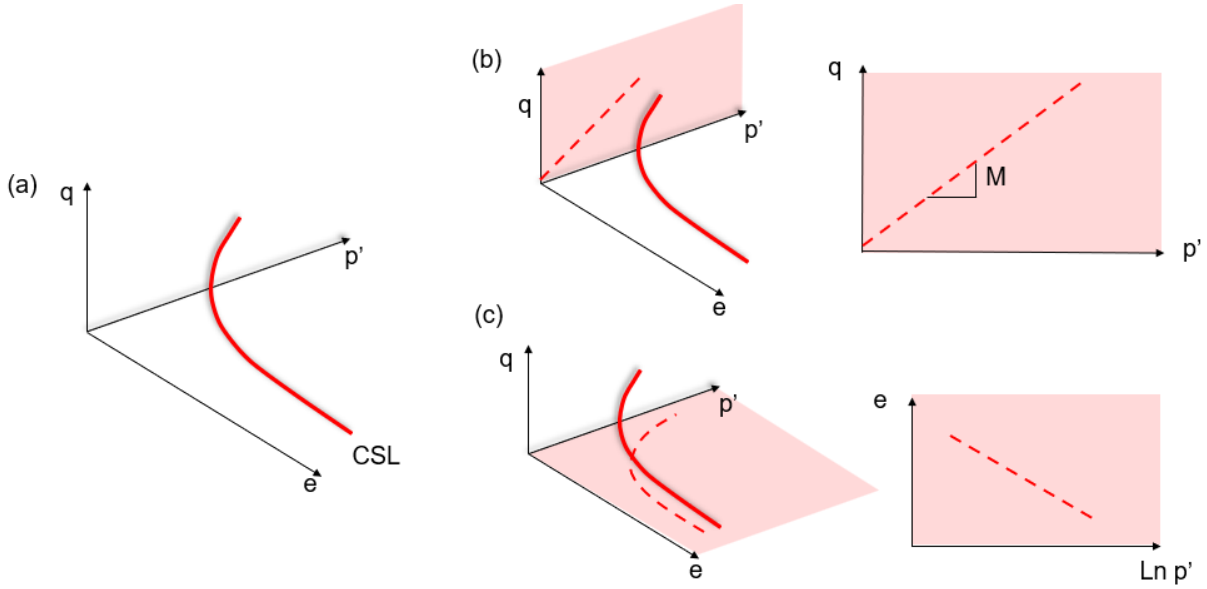

Figure 2.5 - Critical state line: (a) representation in the space of stress and void ratio, (b) projection in the *q-p'* plane, and (c) projection in the *e-ln(p')* plane.

The projection of the CSL onto the *e-ln(p')* plane plays an important role in interpreting the material's behavior, as it can be used to differentiate whether the sample will exhibit a contractive or dilatant behavior (under drained shearing). Based on this, Been and Jefferies (1985) developed the concept of the state parameter (ψ), which is defined as the difference between the current void ratio ($e_{current}$) and the void ratio on the CSL (e_{CSL}) for the same stress state:

$$\psi = e_{current} - e_{CSL} \qquad \text{Equation 2-2}$$

Figure 2.6a illustrates the concept of the state parameter. If the material is above the CSL in *e-ln(p')* plane, it has a positive state parameter and is in a loose condition, showing a tendency to contract when drained sheared. In an undrained case (constant volume), the tendency for volume reduction results in the generation of positive excess pore pressure, which causes a decrease in the mean effective stress and, consequently, a reduction in strength, as represented by the continuous path in Figure 2.6b. On the other hand, if the material is below the critical state line, it has a negative state parameter and is in a dense condition. In this case, when drained sheared, the material will tend to expand, or, in an undrained condition, generate negative excess pore pressure, which increases the mean effective stress and, consequently, leads to a gain in strength, as illustrated by the dotted path in Figure 2.6b.

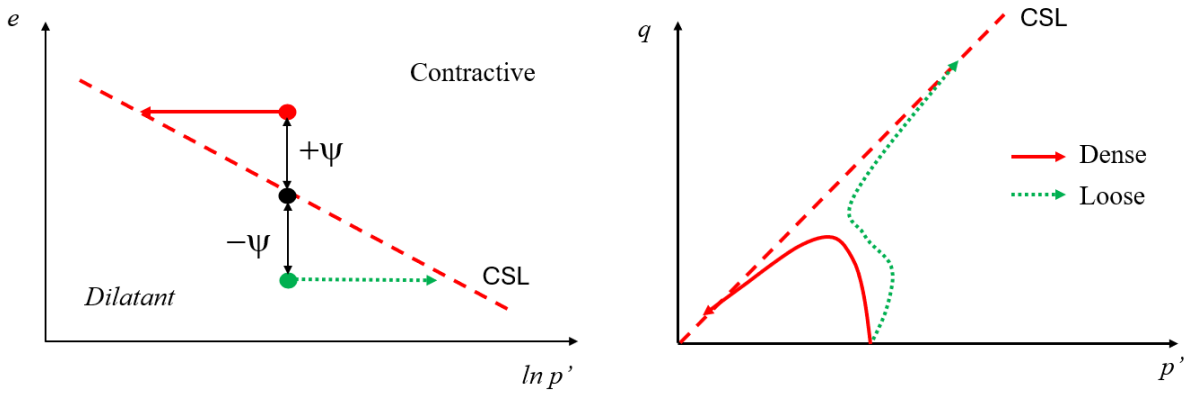

Figure 2.6 - (a) State parameter concept, and (b) typical undrained stress path for loose and dense samples.

2.2 - STATIC LIQUEFACTION

Granular soils, such as sand or silty soils, under loose conditions, tend to experience volume reduction when subjected to drained shearing. When these loose materials are saturated and subjected to monotonic shear loading, a rupture process can initiate (due to the boundary condition) and trigger the undrained mechanism known as static liquefaction, where 'static' refers to the monotonic nature of the trigger (Kramer, 1996; Sadrekarimi, 2014; Jefferies and Been, 2015). The tendency for volume reduction leads to an increase in pore pressure and, consequently, a reduction in effective stress. This mechanism results in a loss of particle contact, decreasing the material's strength and stiffness (Borja, 2006; Bedin et al., 2012; Jefferies and Been, 2015; Zhu et al., 2021).

The undrained behavior mentioned earlier can occur even in typically drained materials, due to boundary conditions imposed during laboratory testing or field conditions, such as the material being surrounded by fine layers, among other possible factors.

An important concept related to static liquefaction is the instability line, which represents the point at which the material exhibits a reduction in strength until it reaches the critical state condition. In Figure 2.7, the difference between the instability line and CSL is illustrated. This figure shows the behavior of five isotropically consolidated samples at the same specific volume but with different confining stresses. Although all samples reach the failure line, only samples C, D, and E exhibit a contractive behavior, since they have a positive state parameter.

The presence of loose and saturated granular materials is a common condition found in tailings dams, resulting from treatment and disposal procedures of mining by-product materials. Various destabilizing processes can initiate static liquefaction within these dams, collectively called triggers (Martin and McRoberts, 1999; Olson and Stark, 2003; Sadrekarimi, 2014). Some examples of triggers are dam raising, foundation displacement, or an increase in the water table level (Figure 2.8), and a comprehensive overview of triggers can be found in the works of Martin and McRoberts (1999), Jefferies and Been (2015), Santamarina et al. (2019), and Fourie et al. (2022). What these triggers have in common is their potential to subject certain zones within the dam to stress paths that lead to an unstable equilibrium condition delineated by the instability line, as exemplified in Figure 2.8 (Lade and Pradel, 1990; Chu and Leong, 2002; Lade and Yamamuro, 2011; Ledesma et al., 2022).

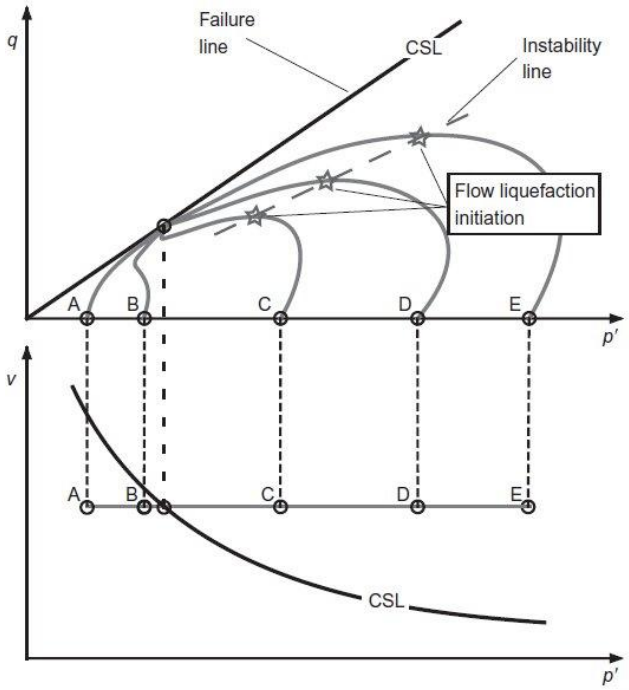

Figure 2.7 - Typical undrained stress path for samples with the same void ratio but different confining stresses, illustrating the concept of the instability line (after Andrade, 2009).

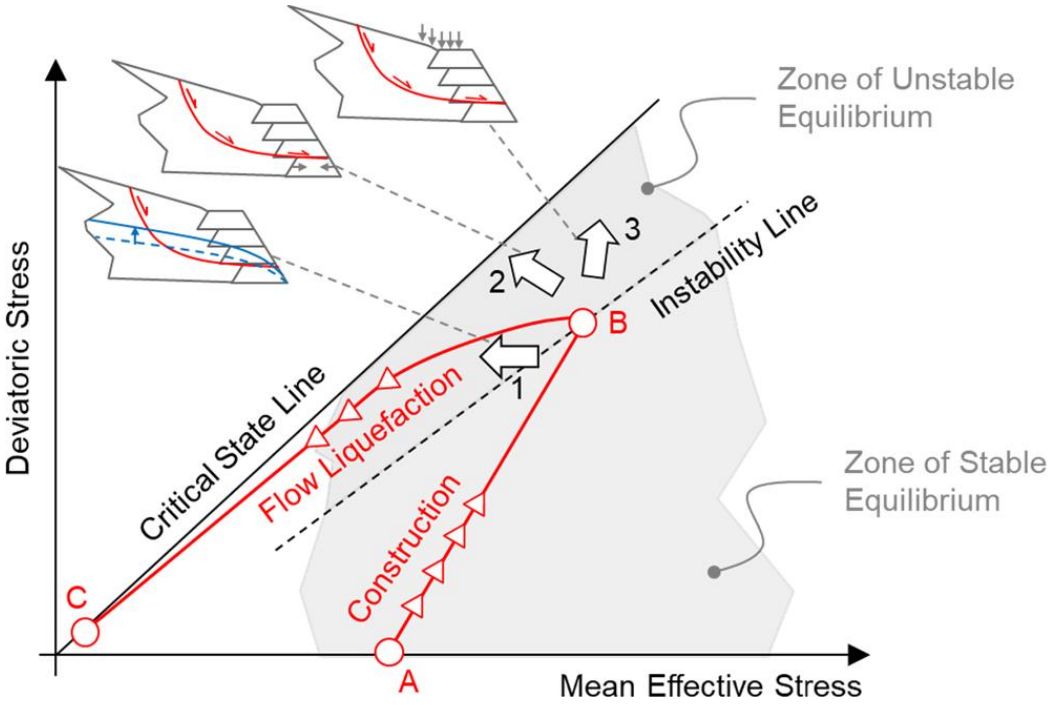

Figure 2.8 - Conceptual stress path to illustrate the transition from a stable to an unstable state, delineated by the instability line, caused by a liquefaction trigger (after Ledesma et al., 2022).

2.3 - CONSTITUTIVE MODEL

In general, the models of interest for this study are based on elastoplasticity theory. For standardization purposes, the equations will be written in terms of the Cambridge invariants: mean effective stress (p'), deviatoric stress (q), and Lode angle (θ) (Wood, 2017). The elastoplasticity theory presented in this chapter is based on the books by Wood (1990, 2017); for further details, the reader is referred to these references. These invariants are given by:

$$p' = \frac{\sigma'_1 + \sigma'_2 + \sigma'_3}{3} \qquad \text{Equation 2-3}$$

$$q = \frac{1}{\sqrt{2}}\sqrt{(\sigma'_1 - \sigma'_2)^2 + (\sigma'_1 - \sigma'_3)^2 + (\sigma'_2 - \sigma'_3)^2} \qquad \text{Equation 2-4}$$

$$\theta = \text{atan}\left[\frac{\sigma'_1 - 2\sigma'_2 + \sigma'_3}{\sqrt{3}(\sigma'_1 - \sigma'_3)}\right] \qquad \text{Equation 2-5}$$

where σ'_1, σ'_2, and σ'_3 are the major, intermediate, and minor principal stresses, respectively.

In elastoplastic models, the constitutive matrix ([D]) or its inverse, called the compressibility matrix ([C]), relates the strain increments ($\{d\varepsilon\}$) to the stress increments ($\{d\sigma\}$) through the following equations:

$$\{d\sigma\} = [D]\{d\varepsilon\} \qquad \text{Equation 2-6}$$

$$\{d\varepsilon\} = [C]\{d\sigma\} \qquad \text{Equation 2-7}$$

The compressibility matrix is subdivided into an elastic component ([C^e]) and a plastic component ([C^p]):

$$[C] = [C^e] + [C^p] \qquad \text{Equation 2-8}$$

The elastic component of the strain increments can be defined by Hooke's law:

$$\begin{Bmatrix} d\varepsilon_p^e \\ d\varepsilon_q^e \end{Bmatrix} = [C^e] \begin{Bmatrix} dp' \\ dq \end{Bmatrix} = \begin{bmatrix} 1/K & 0 \\ 0 & 1/3G \end{bmatrix} \begin{Bmatrix} dp' \\ dq \end{Bmatrix} \quad \text{Equation 2-9}$$

Where *K* is the bulk modulus, *G* is the shear modulus, and the subscripts "p" and "q" represent, respectively, the volumetric and deviatoric components of the strains, and the superscript "e" represents the elastic portion.

The bulk modulus and shear modulus are related to Young's modulus and Poisson's ratio, respectively, by:

$$K = \frac{E}{3\,(1-2v)} \quad \text{Equation 2-10}$$

$$G = \frac{E}{3\,(1+v)} \quad \text{Equation 2-11}$$

In elastoplastic models, elastic behavior occurs within stress states that lie inside a domain defined by a function known as the yield surface:

$$f\,(p', q, \theta, s) = 0 \quad \text{Equation 2-12}$$

where *f* is the yield surface and *s* is the stress variable that measures the size of the elastic domain.

When the stress state reaches the yield surface, a combination of elastic and plastic strains begins to occur, provided that loading is applied. As the material is loaded and plastic strains occur, changes in the elastic domain may take place to ensure the consistency condition (*f = 0*). This change is controlled by the parameter *s*, which evolves according the hardening law:

$$ds = H_p\, dh \quad \text{Equation 2-13}$$

where H_p is the plastic modulus and h is the plastic strain component which controls the hardening law.

Finally, to define the directions and magnitude of the plastic strains, a flow rule is required, where the direction of the plastic strains is given by the plastic potential function:

$$g\left(p', q, \theta, r_g\right) = 0 \qquad \text{Equation 2-14}$$

where r_g is a parameter that controls the size of the plastic potential. If g ≡ f, the flow rule is said to be associated; otherwise, it is a non-associated flow rule.

Given the ingredients mentioned earlier (yield surface, hardening law, and plastic potential), the increments of plastic strains are defined as:

$$\begin{Bmatrix} d\varepsilon_p^p \\ d\varepsilon_q^p \end{Bmatrix} = [C^p] \begin{Bmatrix} dp' \\ dq \end{Bmatrix} = \frac{-1}{\frac{\partial f}{\partial s}\left(\frac{\partial s}{\partial h}\frac{\partial g}{\partial p'} + \frac{\partial s}{\partial h}\frac{\partial g}{\partial q}\right)} \begin{bmatrix} \frac{\partial f}{\partial p'}\frac{\partial g}{\partial p'} & \frac{\partial f}{\partial q}\frac{\partial g}{\partial p'} \\ \frac{\partial f}{\partial p'}\frac{\partial g}{\partial q} & \frac{\partial f}{\partial q}\frac{\partial g}{\partial q} \end{bmatrix} \begin{Bmatrix} dp' \\ dq \end{Bmatrix} \qquad \text{Equation 2-15}$$

where the subscripts "p" and "q" represent, respectively, the volumetric and deviatoric components of the strains, and the superscript "p" represents the plastic portion.

Using the additivity theorem, the increments of total strains can be defined as:

$$\begin{Bmatrix} d\varepsilon_p \\ d\varepsilon_q \end{Bmatrix} = \begin{Bmatrix} d\varepsilon_p^e \\ d\varepsilon_q^e \end{Bmatrix} + \begin{Bmatrix} d\varepsilon_p^p \\ d\varepsilon_q^p \end{Bmatrix} \qquad \text{Equation 2-16}$$

Substituting Equation 2-9 and Equation 2-15 into Equation 2-16, the final relation is obtained as:

$$\begin{Bmatrix} d\varepsilon_p \\ d\varepsilon_q \end{Bmatrix} = \left\{ \begin{bmatrix} 1/K & 0 \\ 0 & 1/3G \end{bmatrix} - \frac{1}{\frac{\partial f}{\partial s}\left(\frac{\partial s}{\partial h}\frac{\partial g}{\partial p'} + \frac{\partial s}{\partial h}\frac{\partial g}{\partial q}\right)} \begin{bmatrix} \frac{\partial f}{\partial p'}\frac{\partial g}{\partial p'} & \frac{\partial f}{\partial q}\frac{\partial g}{\partial p'} \\ \frac{\partial f}{\partial p'}\frac{\partial g}{\partial q} & \frac{\partial f}{\partial q}\frac{\partial g}{\partial q} \end{bmatrix} \right\} \begin{Bmatrix} dp' \\ dq \end{Bmatrix} \qquad \text{Equation 2-17}$$

For an accurate simulation of liquefaction, the constitutive model plays a crucial role. The constitutive model must represent the concept of the instability line and capture the tendency of strength and stiffness reduction. Models based on critical state theory, such as the CASM and NorSand, fulfill these requirements and are commonly used for numerical modeling and liquefaction analysis (Mánica et al., 2021; Shuttle et al., 2022; Liu et al., 2024). A description of the formulations of the analyzed models is provided in the following subsections.

2.3.1- CLAY AND SAND MODEL - CASM

The CASM, initially introduced by Yu (1998), is based on the critical state theory, and adopts an approach similar to the Cam-Clay constitutive model (Wood, 1990). The parameters and equations of the model are presented in Table 2.1 and Table 2.2, respectively.

Table 2.1 – CASM parameters.

Component		Description
CSL	Γ	CSL void ratio at p' = 1 kPa, in *e-ln(p')* plane;
	λ	slope of CSL in *e-ln(p')* plane;
	M_{tc}	slope of CSL in *q-p'* plane for triaxial compression condition;
Elasticity	ν	Poisson's ratio
	κ	slope of elastic line in e-ln(p') plane
Plasticity	n	Parameter that controls the yield function shape;
	r	spacing ratio;
	m	Parameter that controls the plastic potential shape;
State	OCR	Over-consolidation ratio;

Table 2.2 – CASM equations.

Component	Equations	
CSL	$e = \Gamma - \lambda \, lnp'$	Equation 2-18
	$M_\theta = M_{TC} \left\{ \frac{2\,\alpha^4}{1 + \alpha^4 + (1 - \alpha^4)\, sen3\theta} \right\}^{1/4}$	Equation 2-19
Yield function	$f = (\frac{q}{M_\theta p'})^{n} + \frac{1}{\ln r} \ln (\frac{p'}{p'_0})$	Equation 2-20
Hardening rule	$\frac{\partial p'_0}{\partial \varepsilon_p^p} = \frac{(1+e)\, p'_0}{\lambda - \kappa}$	Equation 2-21
Plastic Potencial	$g = (\frac{q}{M_\theta p'})^{m} + \mathrm{m} - 1 - \frac{p_c\,(m-1)}{p'}$	Equation 2-22
Elasticity	$K = \frac{(1+e)\, p'}{k}$	Equation 2-23
	$G = \frac{K\,(1-2v)}{(1+v)}$	Equation 2-24

CASM postulates a linear relationship for the critical state line in the *e-ln (p')* plane (Equation 2-18), with consolidation lines assumed to run parallel to the CSL. In contrast to the Cam-Clay model, CASM replaces the normal consolidation line with the reference compression line (RCL), representing the loosest state the material might experience (Figure 2.9). According to Yu (2006), this change was made because the normal compression line of sands, unlike clays, is only reached under high stresses uncommon in engineering problems. The position of the reference consolidation line in CASM is determined by the spatial ratio (*r*, refer to Table 2.1), a parameter used to measure the distance between the critical state line and the reference line.

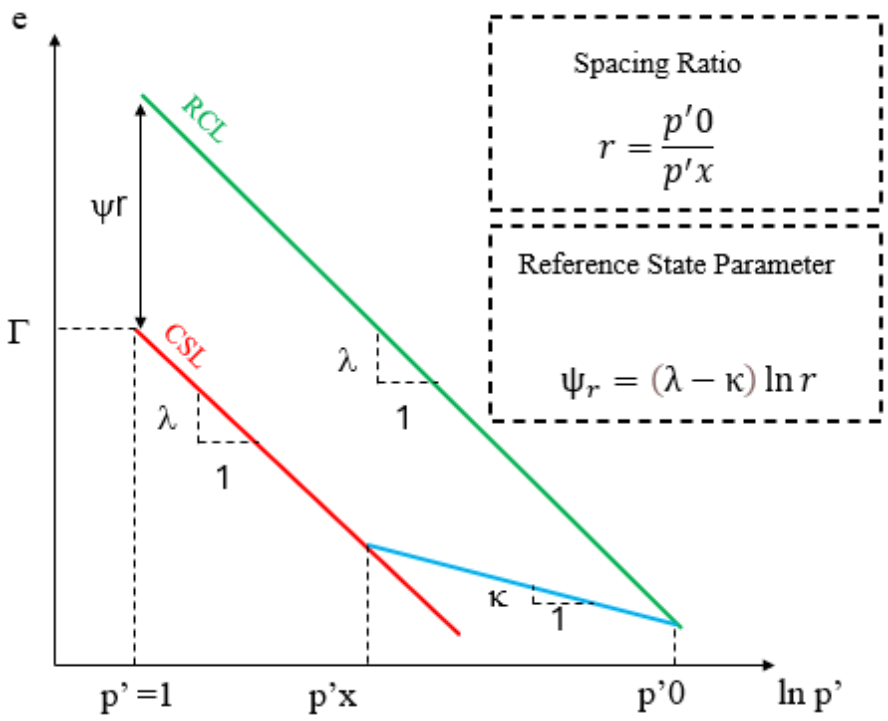

Figure 2.9 – Definition of the Reference Consolidation Line (RCL) in CASM.

A modified version of CASM proposed by Mánica et al. (2021) is employed in this research. Mánica et al. (2021) modified the original version proposed by Yu (1998), integrating the effect of intermediate principal stress, captured by the change in the Lode angle, on the CSL in the q-p' plane (Figure 2.10). They applied the relationship presented in Equation 2-19, proposed by Sheng et al. (2000), where α is a parameter controlling the difference of M_θ between triaxial compression and extension and is defined by:

$$\alpha = \frac{3}{3 + M_{TC}} \qquad \text{Equation 2-25}$$

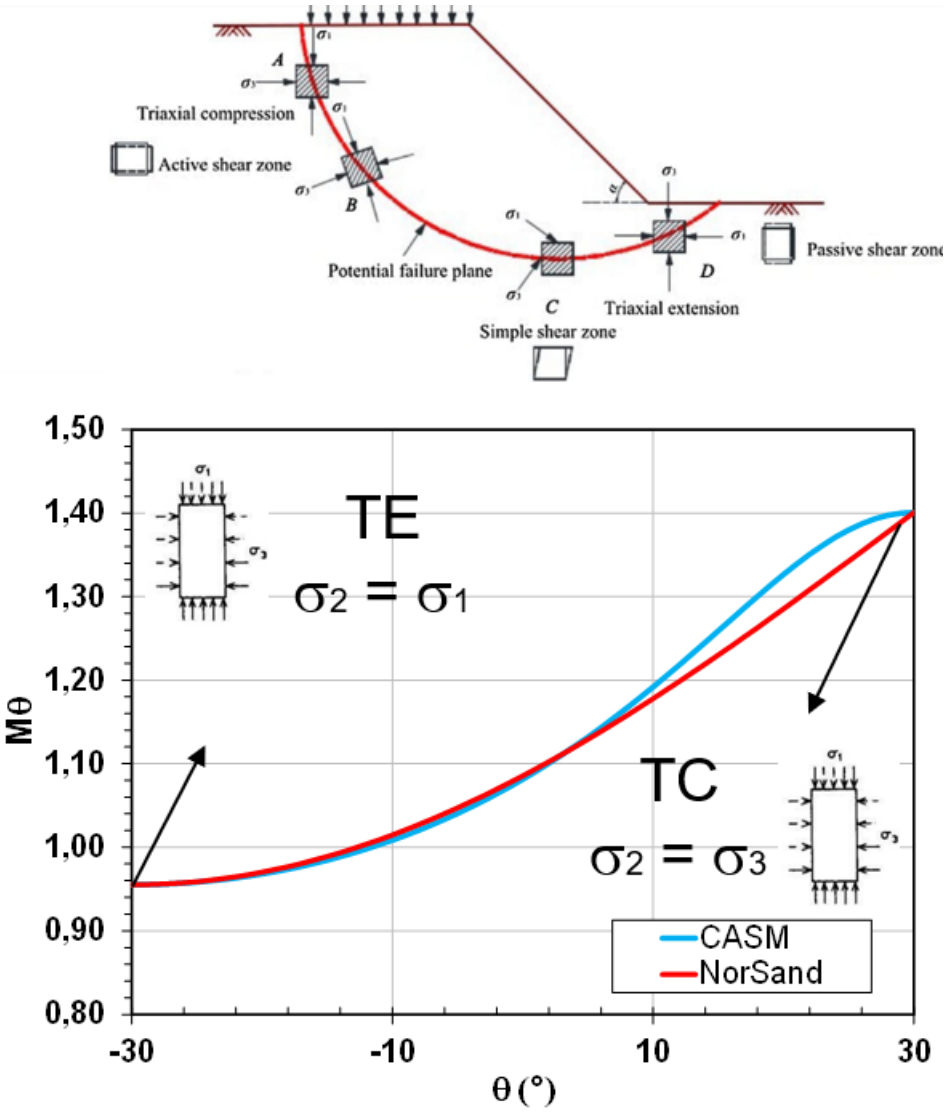

Figure 2.10 – Effect of Lode angle variation on the CSL in the *q*-*p'* plane.

The yield function adopted in the model is presented in Equation 2-20, where the elastic domain is controlled by the pre-consolidation stress (p'_0). It is noteworthy that the ratio p'_0/p' is referred to as the overconsolidation ratio (*OCR*). On the other hand, the hardening law (Equation 2-21) is based on plastic volumetric strain, similar to the Cam-Clay model.

The plastic potential function adopted by Mánica et al. (2021) was also modified from the original formulation by Yu (1998). The plastic potential employed is presented in Equation 2-22, where p_c is given by:

$$p_c = \frac{p}{m-1}\left[\left(\frac{q}{Mp'}\right)^m - 1\right] \qquad \text{Equation 2-26}$$

The p_c must be solved for the current stress state. Notably, the plastic potential function exhibits a distinct form from the yield surface. Consequently, CASM incorporates a non-associated flow rule. The parameter *m* offers flexibility in adjusting the model's response along oedometric paths, ensuring that the K_0 remains constant at a specified value, unaffected by plastic strains.

Finally, the elastic behavior in CASM is defined by the constant Poisson's ratio and the bulk modulus (Equation 2-23 and Equation 2-24). The bulk modulus is related to the slope of the unloading line (κ) and also varies with stress level and void ratio, as depicted in Equation 2-23.

2.3.2- NORSAND

The NorSand constitutive model (Jefferies, 1993; Jefferies and Shuttle, 2005) is based on critical state theory and incorporates the state parameter into its formulation. The parameters and equations of the model are presented in Table 2.3 and Table 2.4, respectively.

NorSand employs the concept of infinite virgin compression lines, which are linked to the initial void ratio and may not necessarily align with the CSL (Figure 2.11). Similar to CASM (Equation 2-28), the CSL is also defined as a straight line in NorSand. It is noteworthy that NorSand also accommodates the adoption of a curved CSL in the *e-ln(p')* plane:

$$e = C_a - C_b\left(\frac{p'}{p_{ref}}\right)^{C_c} \qquad \text{Equation 2-27}$$

where C_a, C_b and C_c are the power-law CSL parameters.

It is worth noting that NorSand also captures changes in the CSL in the *q-p'* plane due to variations in intermediate stress (Equation 2-29). This means it is capable of modeling tailings behavior in a generalized stress state. This capability is crucial for capturing the effect of different stress paths on strength along the potential slip surface (Figure 2.10).

Table 2.3 – Norsand parameters.

Component		Description
CSL	Γ	CSL void ratio at p' = 1 kPa, in *e-ln(p')* plane;
	λ	slope of CSL in *e-ln(p')* plane;
	M_{tc}	slope of CSL in *q-p'* plane for triaxial compression condition;
Elasticity	ν	Poisson's ratio;
	G_{ref}	shear modulus at the reference mean effective stress (p'_{ref});
	n_e	Parameter that controls the relationship between G and p';
Plasticity	N	Volumetric coupling coefficient;
	χ_{tc}	Dilatancy constant for triaxial compression condition;
	H	Plastic hardening modulus for loading, often a fuction of initial state parameter (ψ_0) $H = H_0 - H_\psi \psi_0$;
State	OCR	Over-consolidation ratio;
	ψ	state parameter;

Table 2.4 – NorSand equations.

Component	Equations	
CSL	$e = \Gamma - \lambda \, lnp'$	Equation 2-28
	$M_\theta = M_{TC} - \frac{{M_{TC}}^2}{3 + M_{TC}} cos\left(\frac{3\theta}{2} + \frac{\pi}{4}\right)$	Equation 2-29
Yield function	$f = \frac{q}{M_i p'} + ln\frac{p'}{p_i} - 1$	Equation 2-30
Hardening rule	$\frac{\partial p_i}{\partial \epsilon_q^p} = p_i \left[H \frac{M_i}{M_{i,TC}} \left(\frac{p'}{p_i}\right)^2 \left(\frac{p_{i,max}}{p'} - \frac{p_i}{p'}\right) + ST_s\right.$	Equation 2-31
Plastic Potencial	$g = f = \frac{q}{M_i p'} + ln\frac{p'}{p_i} - 1$	Equation 2-32
Elasticity	$K = \frac{G(1+v)}{(1-2v)}$	Equation 2-33
	$G = G_{ref} \left(\frac{p'}{p_{ref}}\right)^{n_e}$	Equation 2-34

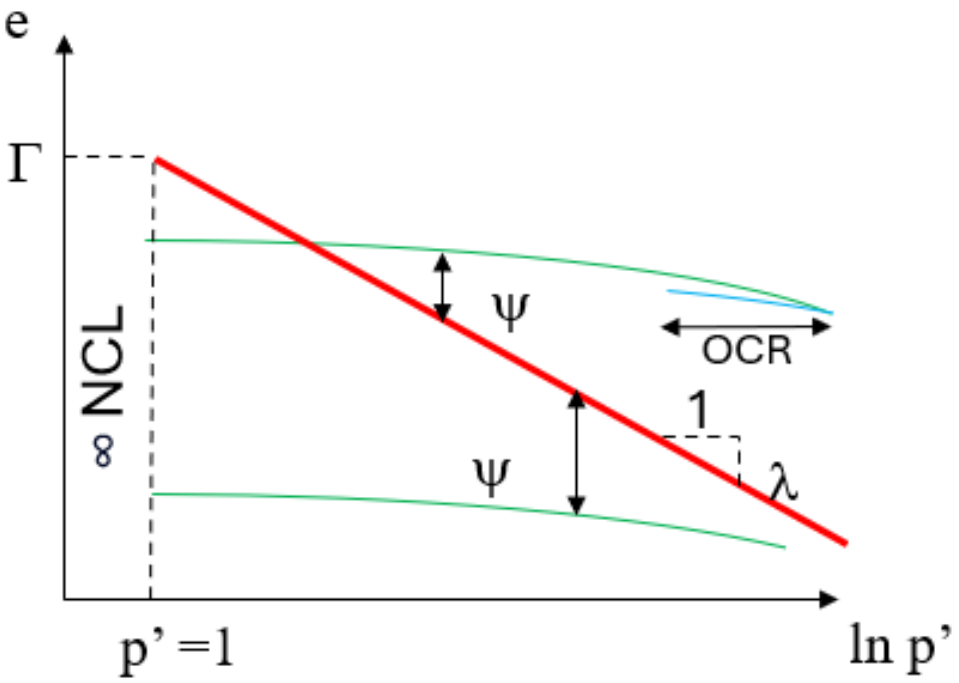

Figure 2.11 – Definition of the infinite Normal Consolidation Line (NCL) in NorSand.

The yield function adopted in NorSand is presented in Equation 2-30. This equation shares the same form as the Cam-Clay model, but it incorporates the concept of the image condition, which is a projection of the critical state. In this sense, the control of the elastic domain shifts from the pre-consolidation stress to the mean stress in the image condition (p_i). This change also leads to a decoupling of the yield surface from the CSL through the replacement of M_θ with M_i, given by:

$$M_i = M_\theta \left(1 - \frac{N\chi_i|\psi_i|}{M_{TC}}\right) \qquad \text{Equation 2-35}$$

where ψ_i and χ_i are, respectively, the state parameter and the dilatancy constant, both in the image condition:

$$\chi_i = \frac{M_{TC}\chi_{TC}}{M_{TC} - \lambda\chi_{TC}} \qquad \text{Equation 2-36}$$

In NorSand, a hardening law based on plastic shear strains was adopted, as presented in Equation 2-31. Here, $p_{i,max}$ is the variable responsible for controlling the maximum dilatancy:

$$p_{i,max} = p' \exp\left(-\frac{\chi_i \psi_i}{M_{i,TC}}\right) \quad \text{Equation 2-37}$$

while T_s represents an additional softening term (Equation 2-38):

$$T_s = \left(\frac{1}{1 + \frac{\chi_i \lambda}{M_{i,TC}}}\right)\left(\frac{K}{p'}\right)\left(\frac{q}{p' n_L}\right) \quad \text{Equation 2-38}$$

where η_L is the stress ratio limit defined by $p_{i,max}$.

Notably, T_s is governed by the parameter S (Equation 2-31), which functions as a Boolean operator, taking either 0 or 1 values. Additional softening should be deactivated under drained conditions; however, in undrained conditions, it may or may not be activated (Jefferies and Been, 2015; Itasca, 2019). The additional softening was activated in all undrained simulations presented in these studies.

NorSand assumes an associated flow rule. Thus, the plastic potential function has the same form as the yield surface (Equation 2-32). The specific form of the flow rule utilized in Norsand limits the model's ability to accurately capture the behavior of materials under oedometric paths (Castonguay and Konrad, 2016; Gomes, 2022; Reid et al., 2022). Given this poor control and based on the authors' experience, it is better to generate a reasonably accurate stress state using a simple model, such as the Mohr-Coulomb model, while maintaining control over oedometric paths, which will govern the stress state in zones prone to instability.

Lastly, the elastic behavior in NorSand is determined by Poisson's ratio, assumed to be constant, and the shear modulus, which varies with stress level and the reference shear modulus (Equation 2-33 and Equation 2-34).

2.4 - FINITE ELEMENT METHOD

The phenomenon of liquefaction has been analyzed using various numerical methods, including the Discrete Element Method (Zhu et al. 2021), the Finite Volume Method (Robertson et al. 2019), and the Finite Element Method (Arroyo and Gens, 2021). Among these, the Finite

Element Method stands out as one of the most renowned approaches within the technical community, being widely employed in liquefaction analyses. This study used this methodology, and for this reason, a brief theoretical review on the subject will be presented.

Figure 2.12 succinctly presents the flowchart of the basic steps involved in the implementation of the Finite Element Method (FEM). It is worth noting that the discussions presented in this section are based on the work of Beer and Watson (1994). For more details on the subject, readers are referred to that reference.

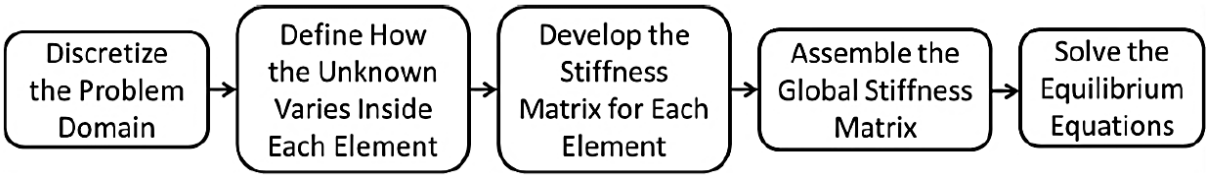

Figure 2.12 - Flowchart of the Finite Element Method.

The formulation of the method involves constructing the stiffness matrix for each finite element and subsequently assembling the global stiffness matrix, which relates forces and displacements in the equilibrium equation:

$$[K]\{du\} = \{dF_{ext}\} \qquad \text{Equation 2-39}$$

where $[K]$ is the global stiffness matrix, $\{du\}$ is the vector of nodal displacement increments, and $\{dF_{ext}\}$ is the vector of external nodal force increments.

The global stiffness matrix is assembled by combining the stiffness matrices of each element in the model. To construct the stiffness matrix, it is first necessary to define the relationship between the strain increment vector and the displacement increment vector, which is represented by the matrix $[B]$:

$$\{d\varepsilon\} = [B]\{du\} \qquad \text{Equation 2-40}$$

where $\{d\varepsilon\}$ is the vector of strain increments.

Finally, the internal stresses must be converted into internal nodal forces, which is accomplished using $[B]^T$:

$$\int_V [B]^T \{d\sigma\} dV = \{dF_{int}\} \qquad \text{Equation 2-41}$$

The integration in Equation 2-41 is initially performed over the element's volume (V); however, in a two-dimensional program, the integration is conducted over the element's area (A). Therefore, Equation 2-41 is modified to:

$$\int_A [B]^T \{d\sigma\} dA = \{dF_{int}\} \qquad \text{Equation 2-42}$$

where $\{dF_{int}\}$ is the vector of internal nodal force increments.

With the previously established relationships, the stiffness matrix is defined by:

$$\int_A [B]^T [D][B] dA = [K^e] \qquad \text{Equation 2-43}$$

where $[K^e]$ is the stiffness matrix of the finite element.

The matrices $[B]$ and $[B]^T$ depend on the type of element used, while the matrix $[D]$ depends on the constitutive model and the analysis conditions employed.

Once the stiffness matrix of each element in the mesh is defined, the global stiffness matrix is assembled, and then Equation 2-39 can be solved, which is done using known forces and displacements (boundary conditions). The system of equations formed is solved using numerical methods such as Gaussian elimination.

For nonlinear problems, the solution of Equation 2-39 becomes iterative, and external loads must be applied incrementally over a finite number of steps (n). In such situations, the initial stiffness method can be used to solve the equilibrium equation. The initial stiffness method is illustrated in Figure 2.13. In this method, an initial global stiffness matrix $[K_0]$ is assembled, and this matrix is kept constant throughout all iterations. After assembling the

stiffness matrix, the displacement increments are calculated, and the solution is updated according to the following equations:

$$[K_0]\{\Delta u^i\} = \{F_n\}_{ext} - \{F_n^{i-1}\}_{int} \quad \text{Equation 2-44}$$

$$\{du^i\} = [K_0]^{-1}(\{F_n\}_{ext} - \{F_n^{i-1}\}_{int}) \quad \text{Equation 2-45}$$

$$\{u_n\} = \{u_{n-1}\} + \sum_{1}^{i}\{du^i\} \quad \text{Equation 2-46}$$

where *i* is the number of iterations.

From the current displacements, the corresponding internal forces for each iteration ($\{F_n{}^i\}_{int}$) are calculated, as shown in Figure 2.10. These forces are then compared with the external forces, and the error between them is determined using:

$$\{R_n^i\} = \{F_n\}_{ext} - \{F_n^i\}_{int} \quad \text{Equation 2-47}$$

where $R_n{}^i$ is the error vector between the internal and external forces at each *i*-th iteration.

The procedure is repeated until the error between internal and external forces reaches a negligible value, specified by the program operator. It is then considered that equilibrium has been reached.

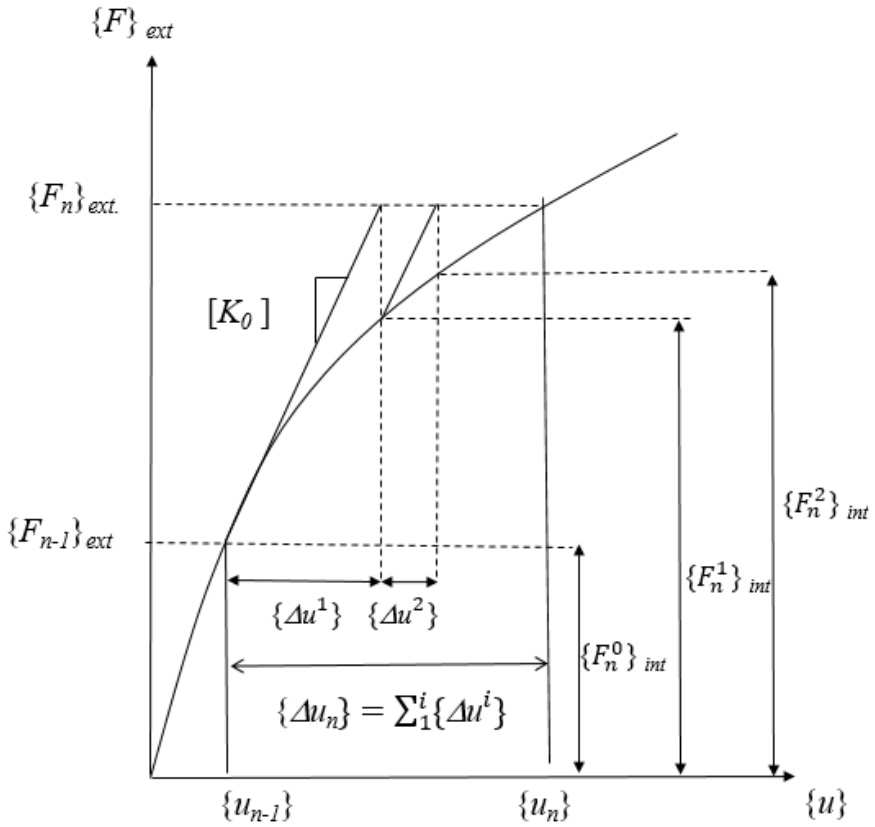

Figure 2.13 - Steps involved in the initial stiffness method for solving nonlinear problems.

3 - MODELING APPROACH

A well-documented case of tailings dam failure in Brazil was selected as the test case to quantify the constitutive models' influence on observed simulation results, as well as to test different decharacterization strategies.

The CASM and NorSand were selected for comparison because they were used by different investigation panels (Robertson et al., 2019, Arroyo and Gens, 2021) to represent the behavior of dam tailings. These studies served as references for model setup and the selection of materials' parameters.

It is worth mentioning that, although Arroyo and Gens (2021) successfully applied the CASM for the failure analyses, Robertson et al. (2019) reported that NorSand exhibited numerical instability and substituted it with a Mohr-Coulomb strain-weakening model for the failure simulation. Therefore, a direct comparison of the influence of the constitutive models on the results was not carried out, raising the question of whether the ability to capture different failure mechanisms was due to the choice of constitutive model. It is argued that a stronger case for the idea that the choice of constitutive model should not influence the triggering mechanisms of liquefaction can be made by demonstrating that similar results can be obtained using different constitutive models, provided that each model is calibrated according to accepted procedures and practices to represent the material behavior. Additionally, it should be noted that both the CASM and NorSand models have capabilities in simulating strain-softening responses due to pore pressure generation, which is a significant advantage compared to commonly used models, such as Mohr-Coulomb and Drucker-Prager (Yu, 2006; Jefferies and Been, 2015; Wood, 2017).

One should consider that despite the issues reported by Robertson et al. (2019) regarding the application of NorSand, this model has been widely applied in the geotechnical community and used in other forensic investigations, such as Fundão (Morgenstern et al., 2015) and Cadia (Jefferies et al., 2019). To the author’s knowledge, this was the first time that NorSand has been successfully applied in the trigger failure analysis of this case.

The analyses of this research were conducted using the finite element software Plaxis2D (Brinkgreve et al., 2020). The stress state was defined for the pre-failure condition through a simulation of the construction process using CASM, following a consolidation type calculation and methodology similar to that presented by Arroyo and Gens (2021). It is worth noting that

while NorSand is available in the Plaxis library, CASM was implemented as a user-defined soil model (Rógenes et al., 2024a).

Reid et al. (2022, 2023) highlighted that initial stress states can significantly influence static liquefaction analysis outcomes. To mitigate the impact of the initial state on results, trigger analyses were conducted using the same initial stress state obtained from the pre-failure model. This procedure is currently available in Plaxis and requires that the final results of one analysis (pre-failure condition) be used as the starting point for the new one (trigger analysis), a similar approach was employed by Reid et al. (2022). It is worth noting that the initial stress is used to initialize the hardening parameters and, consequently, the yield surface at each Gauss point, thus ensuring the consistency condition. NorSand was not used to simulate the construction of the dam because the stress path under oedometric conditions could not be adequately controlled. This behavior has been reported by other researchers (Castonguay and Konrad, 2016; Gomes, 2022; Reid et al., 2022) and will also be discussed in Section 5.1.1.

From the pre-failure condition different triggers were applied numerically in incremental steps, utilizing the arch-length based load control available in Plaxis (Brinkgreve et al., 2020). This numerical procedure enables the development of the failure mechanism, even in the presence of softening behavior, as the analysis progresses beyond the onset of loss of numerical convergence by reducing the active loading in pursuit of numerical convergence.

All analyses were performed using a small-strain approach, as the study focused on evaluating the level of perturbation necessary to trigger static liquefaction and induce failure in the structure, which can be simulated without a large-strain approach. It is emphasized that tracking the run-out of the sliding mass, or the complete post-failure evolution of the flow liquefaction, was beyond the scope of this analysis.

Finally, it is emphasized that the objective of this study was to compare the application of different constitutive models in representing the phenomenon of static liquefaction. Thus, the study does not aim to determine the cause of the rupture in the case study used as a basis, nor does it question the analyses previously conducted by Arroyo and Gens (2021) and Robertson et al. (2019). It is also highlighted that the authors do not make any judgment as to whether the presented models are representative of the actual conditions of the dam before and during the failure.

3.1 - BACK ANALYSIS AND HYPOTHETICAL TRIGGERS

Initially, a back analysis of the failure was carried out, simulating the static liquefaction triggered by an investigation borehole, an action identified by Arroyo and Gens (2021) as a possible triggering mechanism for the failure. This trigger was assessed by applying CASM with parameters proposed by Arroyo and Gens (2021), which were used in the construction simulation, and NorSand, applying parameters proposed by Robertson et al. (2019) to represent the same historical case.

In addition to the back analysis of the failure, two other simulations were conducted using hypothetical triggers: crest loading and gravity increase. This approach of using hypothetical triggers, applied by various researchers (Sottile et al., 2021; Ledesma et al., 2022; Gomes, 2022; Liu et al., 2024), aims to assess the structure's vulnerability before the failure, considering the challenge of predicting a specific trigger.

Based on these analyses, the influence of the adopted constitutive model is discussed by comparing the failure mechanisms observed, stress paths, and the levels of perturbation required to trigger liquefaction.

The trigger analyses were conducted under the assumption of undrained behavior of the saturated tailings material. This implies no volumetric strains with subsequent generation of excess pore pressures during shearing and compression.

3.2 - DECHARACTERIZATION

In recent years, Brazilian regulations have adopted stricter criteria for dam safety, mandating the decharacterization of dams built using the upstream method (ANM, 2022; Schaper et al., 2021). The decharacterization of an upstream-raised tailings dam involves structural interventions designed to eliminate its upstream-raised characteristics. This procedure was mandated by Brazilian regulations due to the uncertainties related to characterizing such structures, resulting in an approach that assumes that if it can liquefy, it will liquefy.

Conceptually, there are three main decharacterization approaches: reinforcement, reservoir excavation, or a combined solution. These strategies are schematically illustrated in

Figure 3.1, and real-world project examples are presented in Figure 3.2. In Figure 3.1 “stabilizing fill” refers to materials with a structural function and constructed with compaction control, whereas “backfill” refers to materials used for confinement that do not require compaction control. It is important to note that the alternatives presented do not exhaust the possible arrangements that can be employed, as the most suitable approach depends on the specific context of each structure. For real-world examples of decharacterization projects, readers are referred to the works of Pereira et al. (2024), Neves and Felitti (2024), and Vale (2024a, 2024b, 2024c, 2025).

To assess the impacts of these different decharacterization strategies, the pre-failure condition of the dam was used as a starting point, aiming to evaluate whether it would be possible to intervene in a critical structure without triggering the liquefaction.

The numerical model calibrated for back-analysis of failure will be applied to simulate the decharacterization strategies presented in Figure 3.1. The impacts and mechanisms promoted by these interventions will be analyzed, to define the strategy that causes the least disruption, thereby creating a more favorable condition for the safety of the structure.

The analyses are conducted under the assumption of undrained behavior of the saturated tailings material. Additionally, models based on the fully coupled flow-deformation approach (Brinkgreve et al., 2020) were also conducted to evaluate the effect of time on static liquefaction analyses. The coupled hydromechanical analysis is based on Biot's theory (Biot, 1941), which allows for the simultaneous consideration of time-dependent changes in stress, strain, and pore pressure.

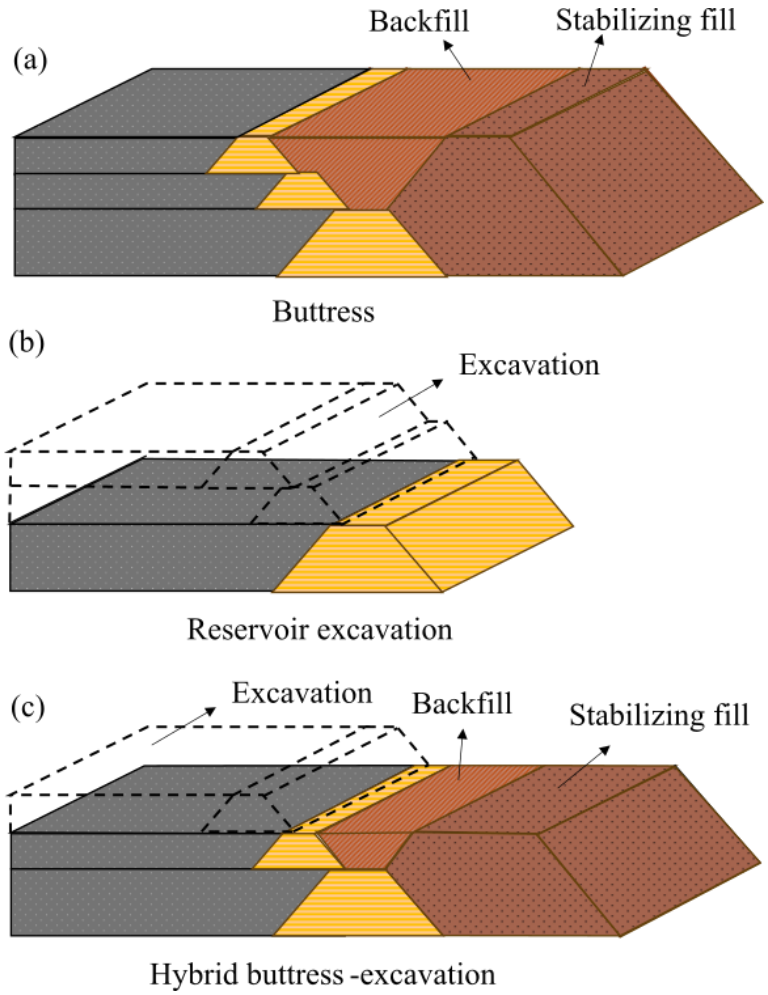

Figure 3.1 - Decharacterization strategies: (a) buttress, (b) excavation, and (c) hybrid buttress-excavation solution.

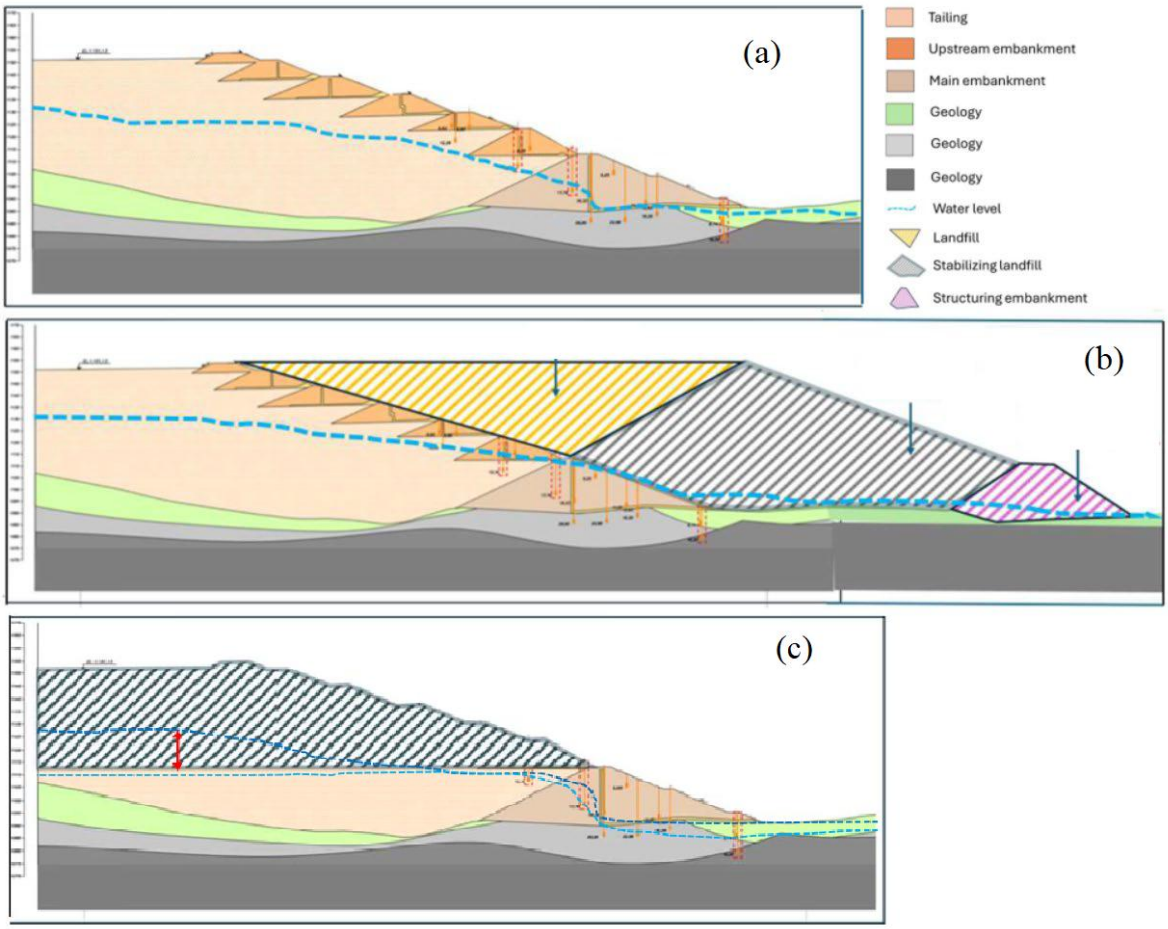

Figure 3.2 - Real-world examples of decharacterization projects: (a) Cross-section of an upstream-raised tailings dam; (b) Engineering strategy for stabilization using decharacterization fill and embankment buttresses; (c) Partial removal of tailings (modified from Neves and Felitti, 2024).

4 - PLAXIS AND CASM: IMPLEMENTATION, VERIFICATION AND CALIBRATION

In this chapter it is presented the CASM implementation using an explicit integration scheme as a user-defined model in Plaxis (Brinkgreve et al. 2020). It includes a procedure to validate the implementation, along with additional parametric analyses based on a series of numerical laboratory tests. Validation results demonstrate the consistency and robustness of the formulation proposed, and the procedure described will serve as a methodology to validate future implementations. Of note, this chapter is a partial reproduction of the papers published by Rógenes et al. (2024a), Gomes et al. (2024) and Nazareth et al. (2025), of which the author of this thesis is the main author or a co-author.

4.1 - IMPLEMENTATION

CASM was implemented in the finite element software Plaxis, which allows for the incorporation of new constitutive models through its User Defined Soil Model (UDSM) functionality. To integrate a user-defined constitutive model into the software, the code, written in Fortran, must be compiled into a Dynamic-link library (DLL) file and added to the program's directories.

The constitutive model will be invoked at each Gauss point, and Plaxis will provide preliminary information such as stress state, pore pressures, and state variables, along with strain increments as input data to the user-defined script. The constitutive model will then compute stress increments according to the defined formulation, and, subsequently, Plaxis will solve the equilibrium equations using the finite element method and will pass new strains back to the constitutive model. This cycle repeats until convergence is achieved.

To make the DLL functional within the main Plaxis program, it is necessary to develop a code that communicates with specific subroutines:

1. Initialization of state variables: At this stage, initial values of user-supplied properties and state variables are defined;
2. Integration of constitutive relations: During these steps, calculations are performed to determine new stresses based on strain increments;

3. Creation of the elastoplastic stiffness matrix: This involves creating the matrix that describes the relationship between stresses and strains for elastoplastic material behavior;
4. Creation of the elastic stiffness matrix: Here, the matrix describing the relationship between stresses and strains for purely elastic material behavior is created.

The main code of the constitutive model implementation involves integrating the constitutive relations. During the integration process, an elastic prediction is first made. If it is determined that the new stress state lies outside the yield surface, a plastic correction is performed, which is necessary to ensure consistency. The generalized elastoplastic constitutive relation was presented in Equation 2-17.

In the CASM, the hardening parameter controlling the variation of the elastic domain is the pre-consolidation stress p_0, thus $s = p_0$. Since hardening is governed by volumetric plastic strain, $h = \varepsilon_p^p$. Considering that the yield function and the plastic potential function adopted in CASM are given by Equation 2-20 and Equation 2-22, respectively, and that the hardening law is defined by Equation 2-21, the following derivatives can be defined:

$$\frac{\partial f}{\partial p'} = \left(\frac{q}{M_\theta}\right)^n \left(\frac{-n}{p'^{n+1}}\right) + \frac{1}{p' \ln r} \qquad \text{Equation 4-1}$$

$$\frac{\partial f}{\partial q} = \left(\frac{1}{M_\theta p'}\right)^n (nq^{n-1}) \qquad \text{Equation 4-2}$$

$$\frac{\partial g}{\partial p'} = \left(\frac{q}{M_\theta}\right)^m \left(\frac{-m}{p'^{m+1}}\right) + \frac{p'c(m-1)}{p'^2} \qquad \text{Equation 4-3}$$

$$\frac{\partial g}{\partial q} = \left(\frac{1}{M_\theta p'}\right)^m (mq^{m-1}) \qquad \text{Equation 4-4}$$

$$\frac{\partial f}{\partial s} = \frac{\partial f}{\partial p'_o} = \frac{-1}{ln\, r}\left(\frac{1}{p0'}\right. \qquad \text{Equation 4-5}$$

$$\frac{\partial s}{\partial h} = \frac{\partial p'_o}{\partial \varepsilon_v^p} = \frac{(1+e0)p'_o}{\lambda - \kappa}$$ Equation 4-6

During the plastic correction process, the initial approach is to apply the entire strain increment to integrate stresses and hardening parameters. To ensure numerical stability, an explicit automatic sub-incrementation algorithm, proposed by Sloan et al. (2001), has been adopted. If the integration fails to meet the specified error tolerance, the strain increment is reduced. This iterative process continues until all strain is applied while maintaining the specified error threshold. Flowchart for automatic sub-incrementation integration algorithm is presented in Figure 4.1.

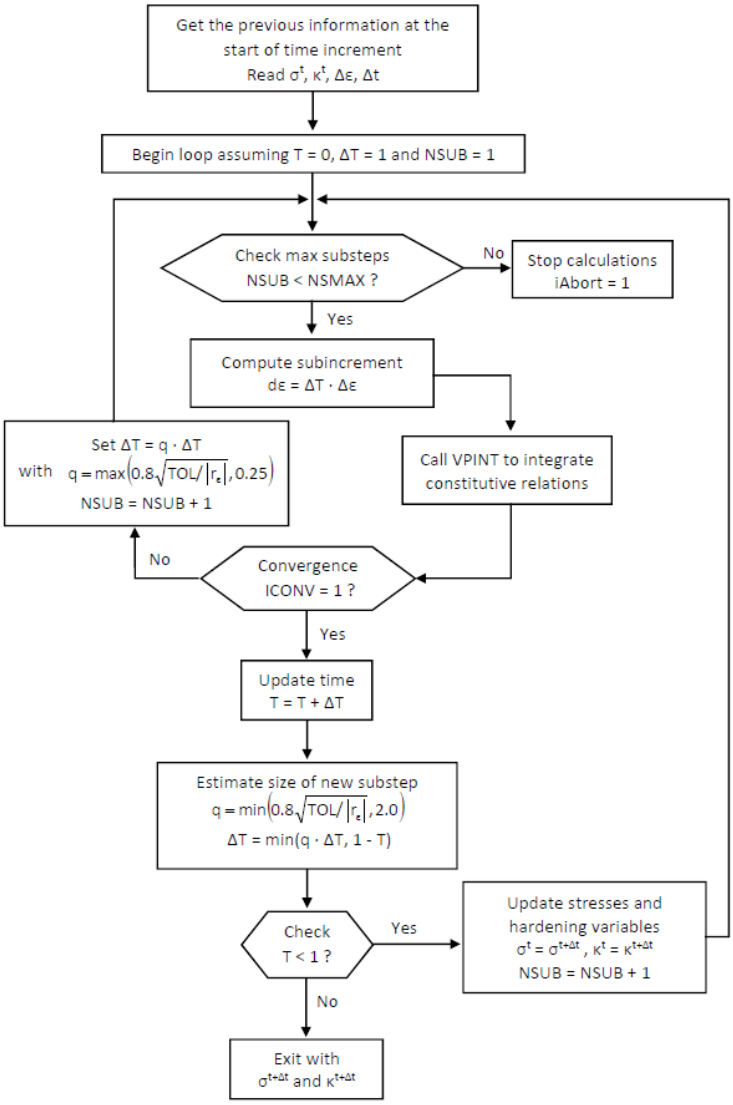

Figure 4.1 - Flowchart for automatic substepping integration. (after Cirone, 2020)

4.2 - VERIFICATION

To validate the numerical implementation of CASM, a series of numerical tests were conducted. The model developed for this stage consists of a sample under axisymmetric conditions with regular geometry, as shown in Figure 4.2. The parameters used in these simulations are presented in Table 4.1, which were defined by Arroyo and Gens (2021) to represent iron ore tailings.

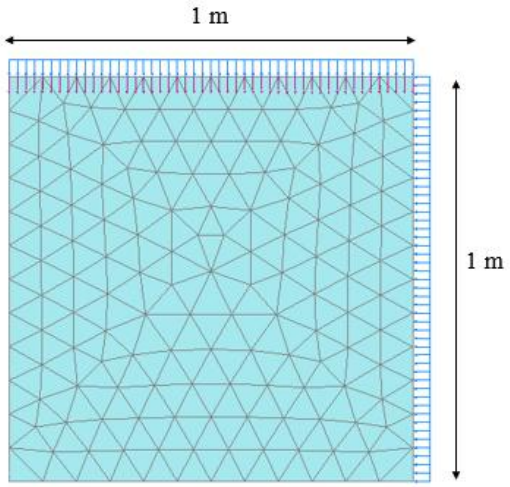

Figure 4.2 - Boundary condition and problem setup used for CASM implementation validation.

Table 4.1 – CASM parameters applied in the validation simulations.

Component	Parameters
Γ	1.20
λ	0.053
M_{tc}	1.40
n	5
r	35
m	2.3
κ	0.007
ν	0.3
OCR	1

For a comprehensive validation, numerical drained and undrained triaxial tests were simulated under compression and extension conditions. The results are presented in Figure 4.3, demonstrating the CASM ability to represent varying strength values depending on the simulated path, the hardening process under drained conditions, and the generation of pore pressures and brittle behavior under undrained conditions.

Isotropic compression and oedometer tests were also conducted. The results are presented in Figure 4.4, showing an increase in stiffness with increasing confinement in both tests. It is noteworthy that in the oedometer test, the sample was initially in an isotropic condition and as it was compressed, it approached a constant K0 value, demonstrating the model's capability to control the coefficient of lateral earth pressure, which is crucial for applications involving staged construction simulations.

An unloading followed by an undrained loading test was conducted, and the result is presented in Figure 4.5 alongside a result of a numerical test on a normally consolidated sample. It is observed that the model successfully captures the increase in OCR induced by unloading, leading to elastic behavior at the beginning of reloading. Such scenarios are crucial for dam decharacterization involving excavation processes and subsequent unloading.

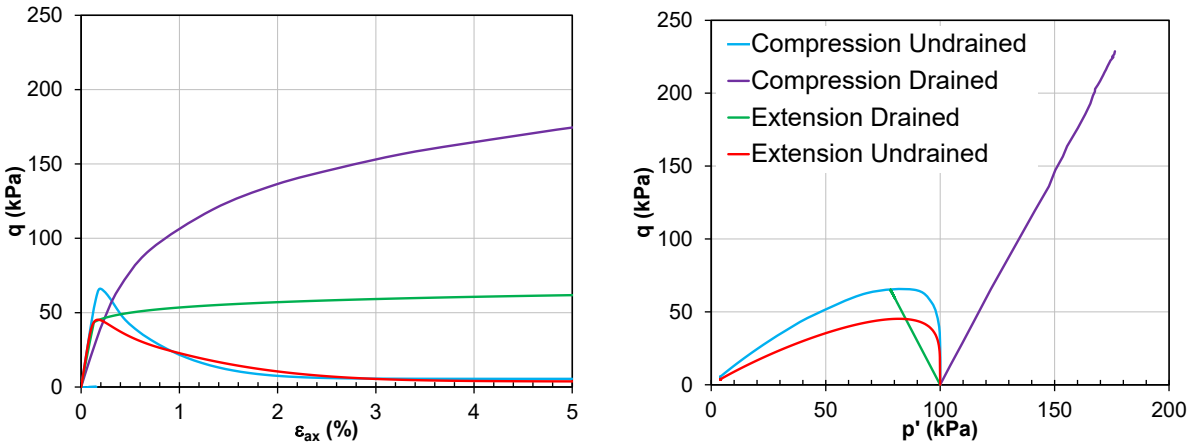

Figure 4.3 - Verification of CASM implementation in conventional triaxial tests.

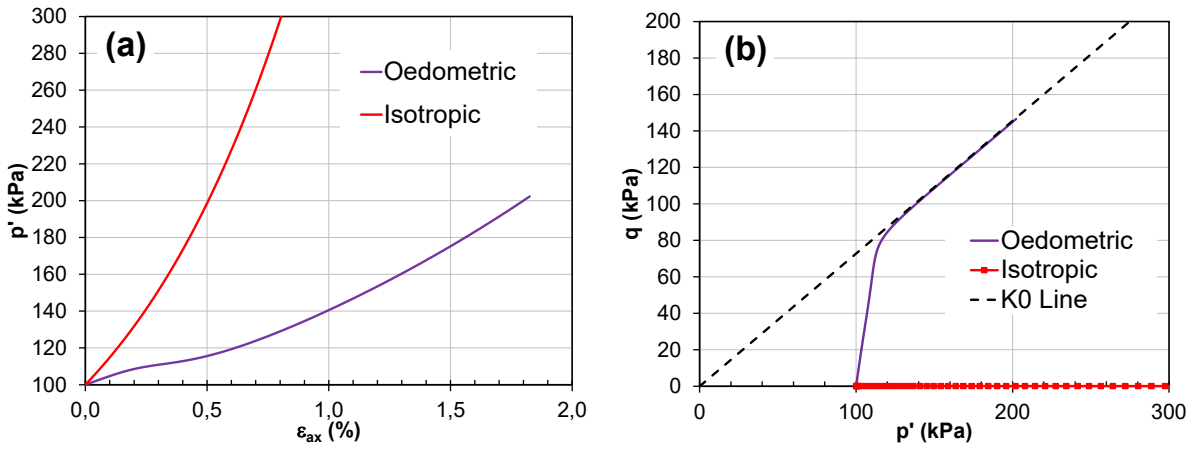

Figure 4.4 - Verification of CASM implementation in isotropic compression and oedometer paths: (a) mean effective stress – axial strain, and (b) deviatoric stress - mean effective stress.

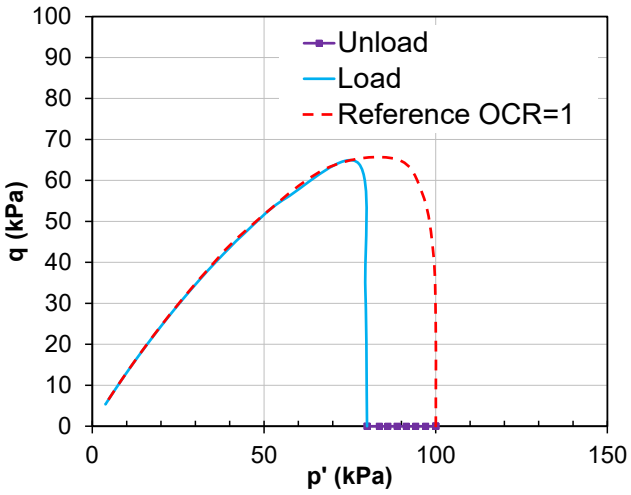

Figure 4.5 - Verification of CASM implementation in unloading paths followed by undrained recompression.

The numerical verification also included partially drained/undrained behavior through hydro-mechanical coupling approaches, where excess pore pressure generation is a function of strain rate, soil stiffness, and permeability. In this simulation, horizontal and vertical hydraulic conductivities of 1.00E-08 m/s and 2.00E-09 m/s, respectively, were applied, as presented by Arroyo and Gens (2021). The results obtained are shown in Figure 4.6, indicating that CASM can simulate partially drained behavior in triaxial compression tests by adjusting the strain rate, ranging from fully drained to undrained conditions. t should be noted that the intermediate case was simulated by applying a compression rate sufficient to induce a partially drained behavior for demonstration purposes.

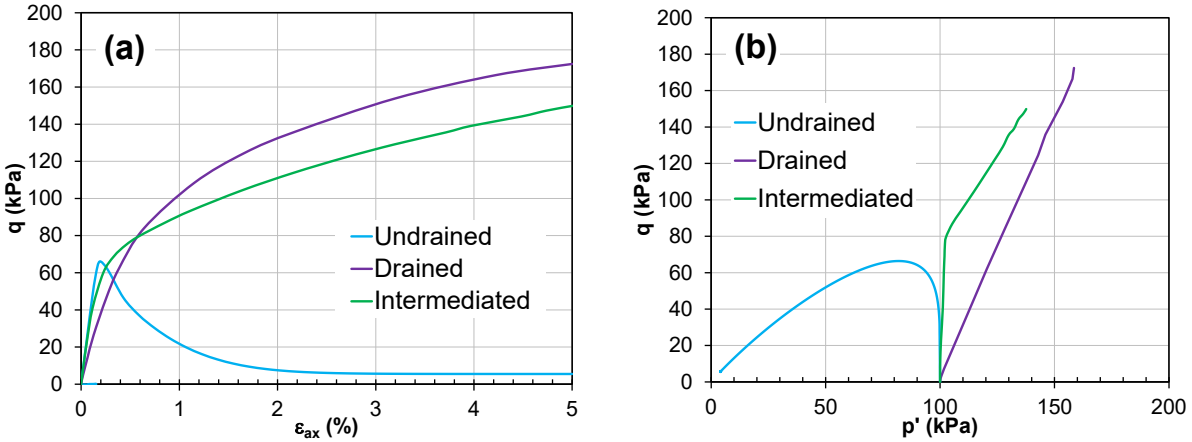

Figure 4.6 - Verification of hydro-mechanically coupled triaxial tests using CASM: (a) deviatoric stress – axial strain, and (b) deviatoric stress – mean effective stress.

4.3 - PARAMETRIC ANALYSIS

The main difference between CASM and Cam-Clay models lies in the addition of parameters n, r, and m. For instance, if $r = 2$, $n = 2$, and $m = 2$, CASM simulates behavior similar to that obtained with the Cam-Clay model, as shown in Figure 4.7 (Cam-Clay model parameters were extracted from Table 4.1). Therefore, sensitivity analyses focused on the effects of these parameters on the behavior represented in the CASM. These analyses were conducted starting from the parameters listed in Table 3.

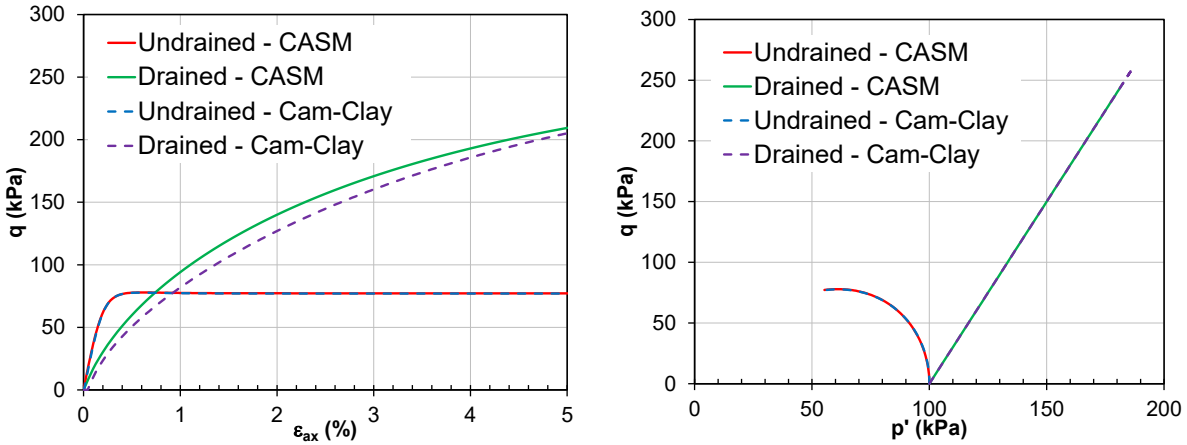

Figure 4.7 - Comparison of triaxial compression test results using the Cam-Clay and CASM models with $r = 2$, $n = 2$, and $m = 2$.

The parameter *n* modifies the shape of the yield surface, as shown in Figure 4.8a. It is evident that a higher *n* expands the elastic domain, thereby increasing the peak undrained strength, as demonstrated by parametric analyses depicted in Figure 4.9

The parameter *r* also influences the shape of the yield surface, as shown in Figure 4.8b, but its primary role is to separate the reference compression line from the critical state line. Thus, an increase in the parameter *r* indirectly promotes an increase in the state parameter, consequently reducing the residual undrained strength, as observed in Figure 4.10.

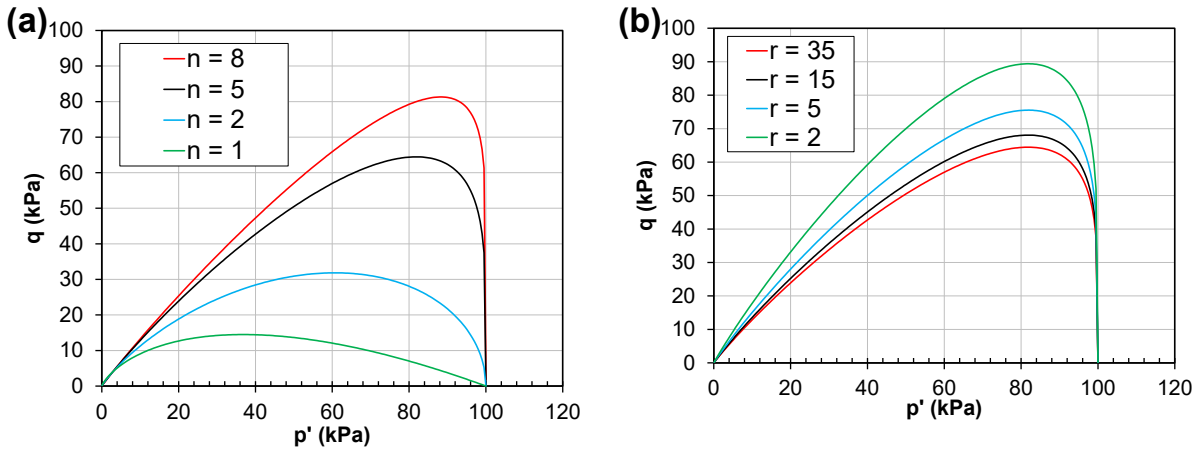

Figure 4.8 - Changes in the yield surface shape due to variations of parameters: (a) *n*, and (b) *r*.

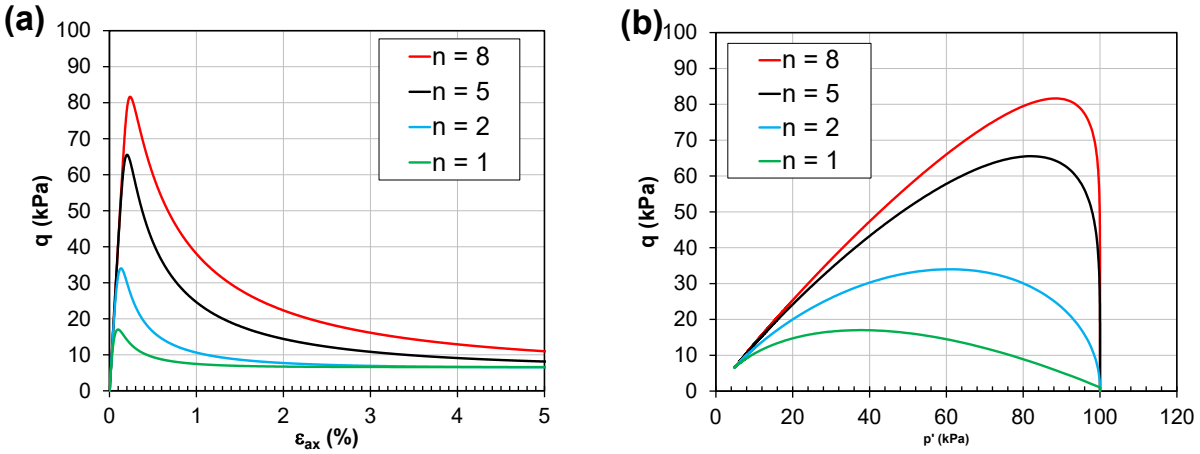

Figure 4.9 - Sensitivity of CASM in undrained triaxial compression tests to variations of *n*: (a) deviatoric stress – axial strain, and (b) deviatoric stress – mean effective stress..

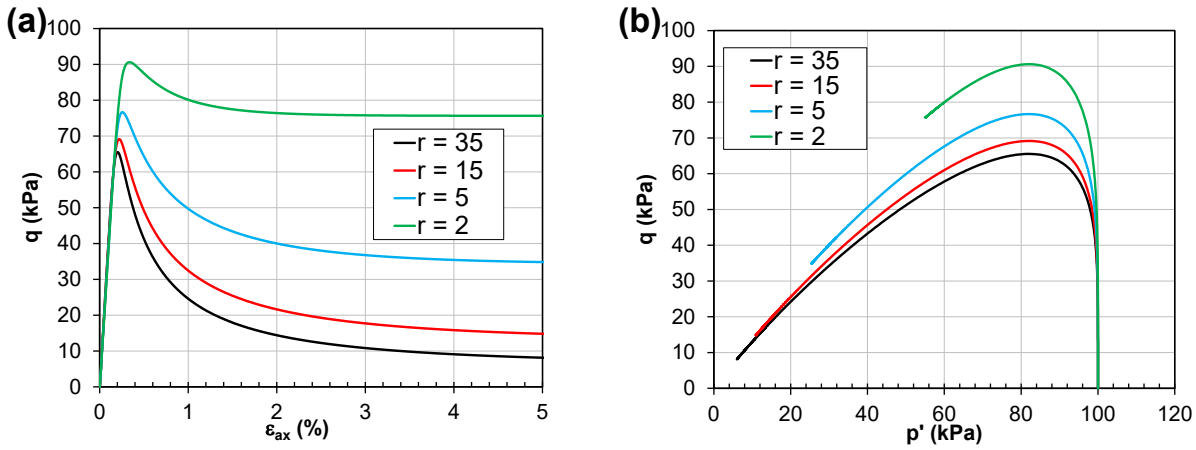

Figure 4.10 - Sensitivity of CASM in undrained triaxial compression tests to variations of r : (a) deviatoric stress – axial strain, and (b) deviatoric stress – mean effective stress..

Given the non-associated flow rule adopted in CASM, the parameter m solely influences the plastic potential function. Thus, in shear loading conditions, such as in triaxial tests, this parameter affects only the deformations, while stress paths remain unchanged (Figure 4.11). On the other hand, in oedometer compression conditions, m directly controls the value of the coefficient of earth pressure at-rest, i.e., the slope of the K_0 line simulated in the model, as seen in Figure 4.12.

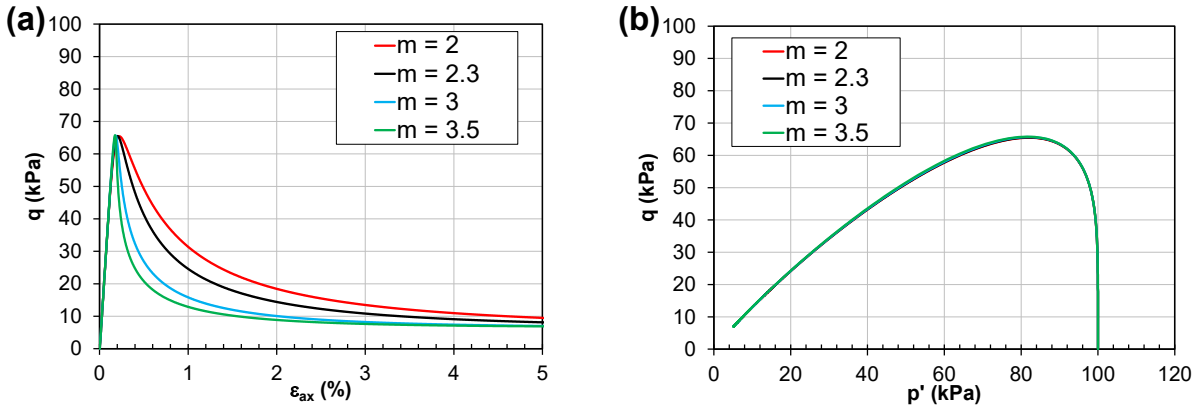

Figure 4.11 - Sensitivity of CASM to variations of the parameter m in undrained triaxial compression tests.

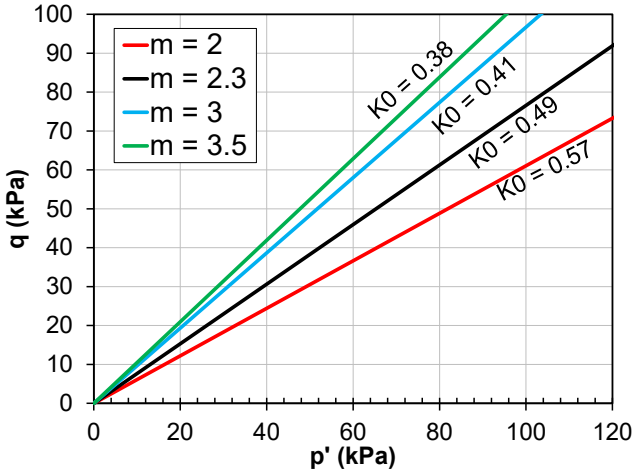

Figure 4.12 - Sensitivity of CASM to variations of the parameter *m* in oedometer compression tests.

4.4 - CALIBRATION METHODOLOGY

Given that CASM does not have a well-defined calibration methodology, this work proposes a calibration methodology for the model parameters, with applications to tailings materials. The proposed methodology was defined based on the parametric analysis conducted in Section 4.3 and on the works of Mánica et al. (2021), Arroyo and Gens (2021), and Nazareth et al. (2025), and was presented by Gomes et al. (2024).

For the calibration of CASM, eight input parameters are required, as presented in Table 2.1. The methodology for determining the required input data for the constitutive model will be divided into 5 steps. It is worth noting that the analytical equations presented were derived under normal consolidation conditions.

4.4.1- Step 1 - Determination of parameters *M*, *Γ* and *λ*

To determine parameters M, Γ, and λ, triaxial tests (conducted under drained or undrained conditions, with the void ratio defined at the end of deviatoric compression) are conducted to establish the CSL on the p'-q plane (Figure 4.13a), and the ln(p')-e plane (Figure 4.13b). In the p'-q plot, parameter M is obtained from the slope of the CSL, while in the ln(p')-e plot, Γ corresponds to the CSL void ratio at p' = 1 kPa, and λ represents the slope of the CSL.

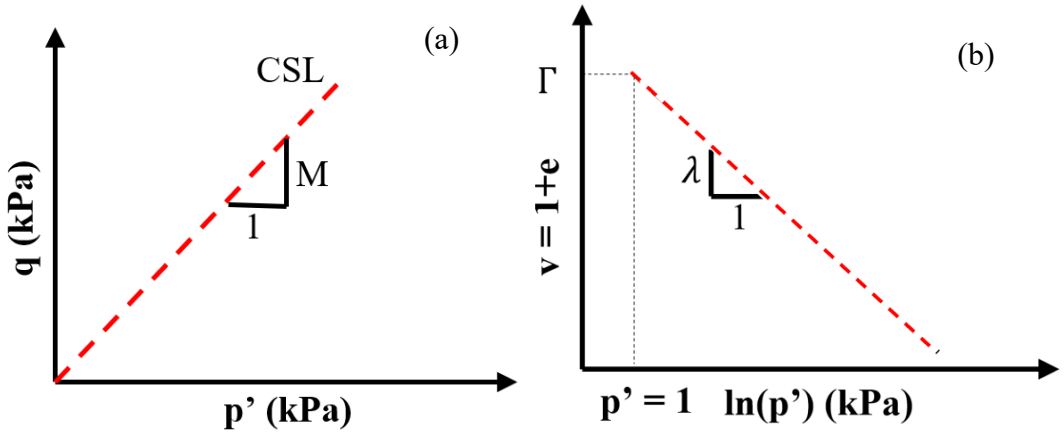

Figure 4.13 – (a) Plot to obtain parameter *M*, and (b) plot to obtain parameters *Γ* and *λ*.

4.4.2- Step 2 - Determination of the elastic parameters *ν* and *k*

The Poisson's ratio (ν) can be obtained through data from drained triaxial tests (with measurements of volumetric or lateral strain) by plotting the axial strain versus radial strain and determining ν from the slope of the line. Alternatively, this parameter can also be obtained from literature references, as Arroyo and Gens (2021), as it does not vary significantly.

To obtain *κ*, consolidation oedometer tests are conducted, and the ln(p') - v graph is plotted (Figure 4.14). The value of *κ* corresponds to the slope of the recompression line, as illustrated in Figure 3.

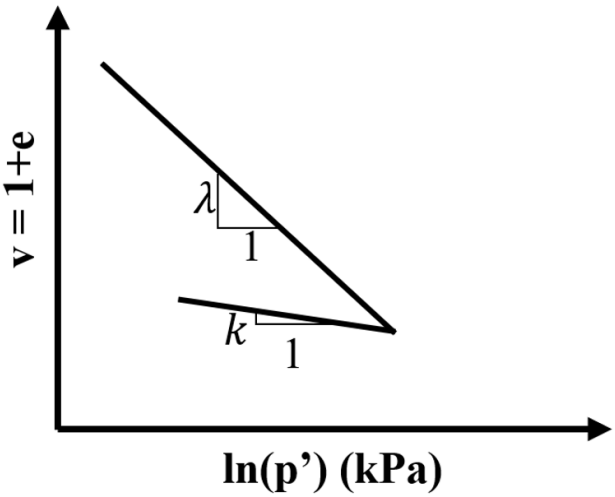

Figure 4.14 – Graph to obtain the parameter *κ*.

According to Mánica et al. (2021), since the parameters ν and κ do not vary much, they can be estimated. In the absence of oedometer tests, κ can be adjusted for a better fit between the calibration results and the triaxial laboratory data (drained and undrained) in the q-ε_{ax} plane. It is also worth noting that Poisson's ratio will control the K_0 condition under an overconsolidated state, as will be discussed in step 3.

4.4.3- Step 3 - Determination of the plastic parameter – *m*

The parameter m controls the shape of the plastic potential and can be used to adjust the model's response in oedometer tests, ensuring that the coefficient of earth pressure at rest (K_0) remains at a specified value without changes due to plastic deformations. The relationship between K_0 and m is given by Equation 4-7 (Mánica et al., 2021).

$$\frac{3\,(\lambda-\kappa)}{2\,\lambda}=\left[\frac{M_{TC}}{m}-M_{TC}\right]\left[\left(\frac{1}{M_{TC}}\frac{3(1-K_0)}{1+2K_0}\right)-\left(\frac{1}{M_{TC}}\frac{3(1-K_0)}{1+2K_0}\right)^{1-m}\right] \qquad \text{Equation 4-7}$$

The equation requires data related to the CSL (M and λ), determined in Step 1, the elastic parameter (κ), determined in Step 2, and K_0, which can be obtained through pressuremeter tests, correlated with available data for similar materials, or estimated using Jaky's equation for normally consolidated condition (Equation 4-8).

$$K_0 = 1 - sen\,\phi' \qquad \text{Equation 4-8}$$

where ϕ' is the effective friction angle.

For overconsolidated material (OCR > 1), elastic behavior will occur, and in this case, K_0 will be controlled through Poisson's ratio. It is essential to note that K_0 is one of the most critical parameters in liquefaction simulations, as it significantly influences the field stress, i.e., the distance from the current stress state to the instability line. Unfortunately, K_0 is one of the most challenging parameters to determine with precision, so we can consider it as one of the "black holes" of geotechnical engineering.

4.4.4- Step 4 - Determination of the spacing ratio - *r*.

The parameter *r* allows control of the distance between the CSL and the virgin compression line on the horizontal axis and is related to residual undrained strength (S_{ur}), determined by Equation 4-9 (Mánica et al., 2021).

$$r = \left[\frac{M_{tc}}{6}\,(1 + 2K_0)\left(\frac{\sigma'_{v0}}{S_{ur}}\right)\right]^{\frac{\lambda}{\lambda-\kappa}} \qquad \text{Equation 4-9}$$

where σ'_{v0} is the initial vertical effective stress.

The equation requires data related to the CSL (M and λ) (Step 1), the elastic parameter (κ) (Step 2), K_0 (Step 3), and the residual undrained strength of the material ($\frac{S_{ur}}{\sigma'_{v0}}$), which can be obtained through triaxial or CPTu tests. It is worth noting that if the $\frac{S_{ur}}{\sigma'_{v0}}$ is defined through isotropically consolidated triaxial tests, K_0 should be taken as 1 in the Equation 4-9.

4.4.5- Step 5 - Determination of the plastic parameter – *n*.

The parameter *n* controls the shape of the yield surface and is related to peak undrained strength (S_{up}), determined by Equation 4-10 (Nazareth et al. 2025).

$$\frac{S_{up}}{\sigma'_{v0}} = \frac{1 + 2K_0}{6} M_{tc}\,(n\,\frac{\psi_r}{\lambda}e)^{\frac{-1}{n}} \qquad \text{Equation 4-10}$$

where ψ_r is the reference state parameter, given by Equation 4-11.

$$\psi_r = (\lambda - \kappa)\ln r \qquad \text{Equation 4-11}$$

To determine parameter *n*, Equation 4-10 is used. The equation requires data related to CSL (M and λ) (Step 1), the elastic parameter (κ) (Step 2), the plastic parameter (r) (Step 3), and the peak undrained strength of the material ($\frac{S_{up}}{\sigma'_{v0}}$), which can be obtained through triaxial or CPTu tests. It is worth noting that if the $\frac{S_{up}}{\sigma'_{v0}}$ is defined through isotropic triaxial tests, K_0 should be taken as 1 in the Equation 4-10.

4.4.6- Calibration for tailing materials

An application of the methodology to calibrate CASM parameters for tailings materials is presented in this section. After obtaining the input data, p'-q and q-ε_{ax} graphs will be illustrated, comparing the calibration results with tests performed on remolded iron tailings samples from the Iron Quadrangle in Brazil.

To determine parameters M_{tc}, Γ, and λ, undrained triaxial tests under isotopically consolidated conditions were conducted to establish the critical state line on the p'-q plane (Figure 4.15), and the ln(p')-v plane (Figure 4.16). In the p'-q graph, parameter M_{tc} = 1.32, from the slope of the CSL. In the ln(p')-e graph, the values obtained were Γ = 1.79 and λ = 0.035. The critical state parameters obtained are close to those presented by Ledesma et al. (2021) for Fundão dam tailings. It should be noted that Figure 4.16 presents the critical state line in the ln(p')-v plane using only the three undrained tests. However, the author acknowledges and advises that critical state lines are more accurately represented with a minimum of five tests (Shuttle and Jefferies, 2010), incorporating both drained and undrained loading conditions.

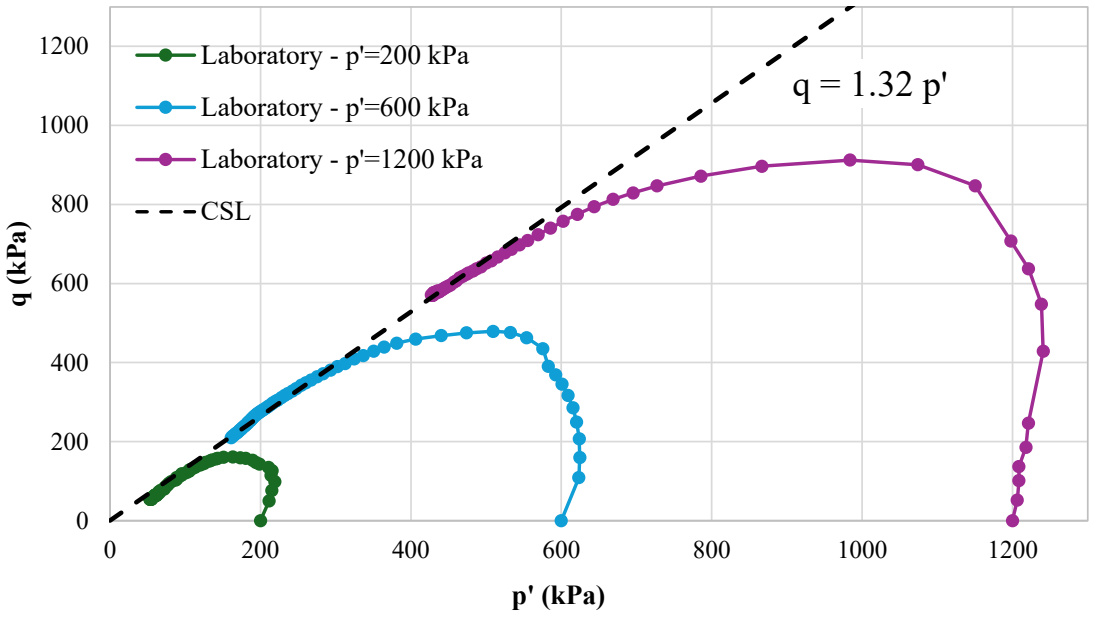

Figure 4.15 – Critical State Line - p'-q plot.

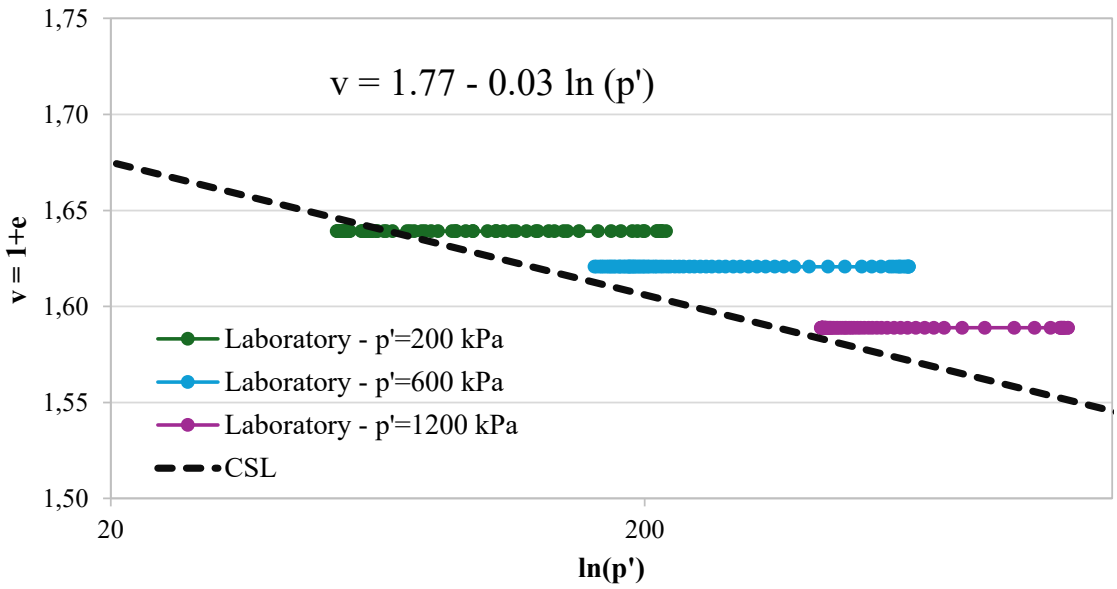

Figure 4.16 – Critical State Line - ln(p')-v plot.

The parameter $\nu = 0.3$ was adopted based on the value reported by Arroyo and Gens (2021) for iron ore tailings. Due to the lack of oedometer consolidation tests, $\kappa = 0.02$ was assumed to improve the fit between the calibration results and the laboratory data in the q-ε_{ax} plane.

A value of $K_0 = 0.5$ was assumed based on Arroyo and Gens (2021), which also aligns with the value given by Jaky's equation. Applying this value together with the previously defined parameters ($M_{tc} = 1.32$, $\lambda = 0.03$, $k = 0.02$) into Equation 4-7 yielded m = 1.70.

To determine the spacing ratio, the residual undrained strength of the material was defined based on triaxial test results (Figure 4.17), which yielded $\frac{S_{ur}}{\sigma'_{v0}} = 0.22$. Using these results in Equation 4-9, the spacing ratio r was calculated as 27.

Finally, the peak undrained strength, $\frac{S_{up}}{\sigma'_{v0}} = 0.38$, derived from the same triaxial tests (Figure 4.18), was used in Equation 4-10, resulting in n = 5.0.

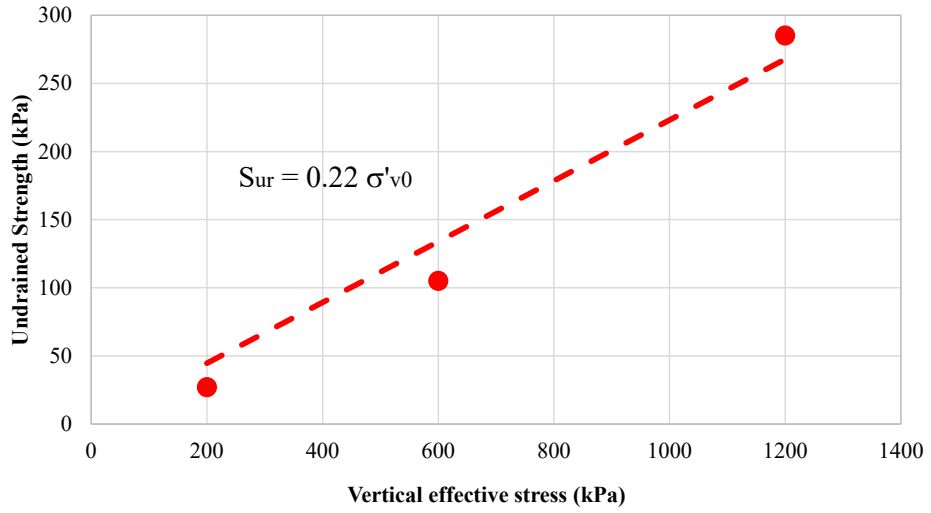

Figure 4.17 – Residual undrained strength

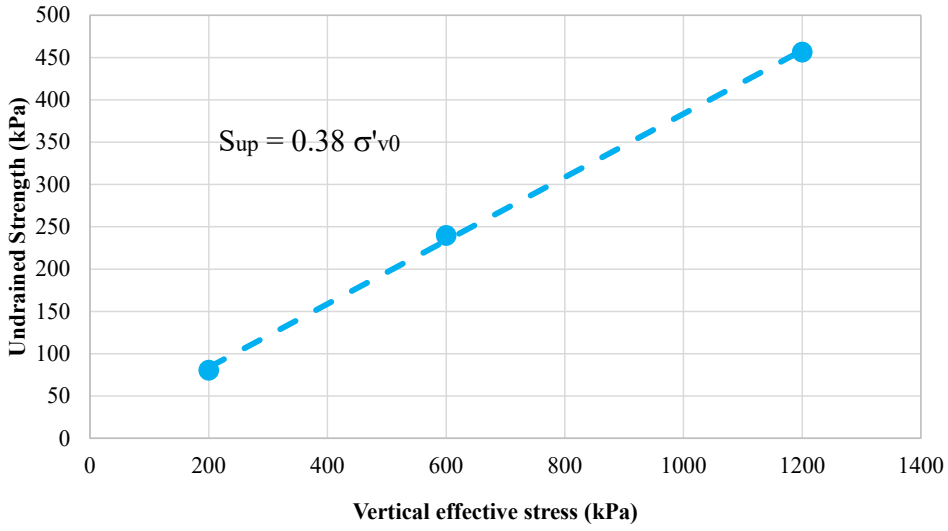

Figure 4.18 – Peak undrained strength

A summary of the CASM parameters obtained from the calibration for the tailing material is presented in Table 4.2. Once the input data from the calibration were defined, the model response was compared with the laboratory test results (Figure 4.19 and Figure 4.20).

Table 4.2 – Calibrated CASM model parameters.

Component	Parameters
Γ	1.77
λ	0.03
M_{tc}	1.32
n	5
r	27
m	1.7
κ	0.02
ν	0.3
OCR	1

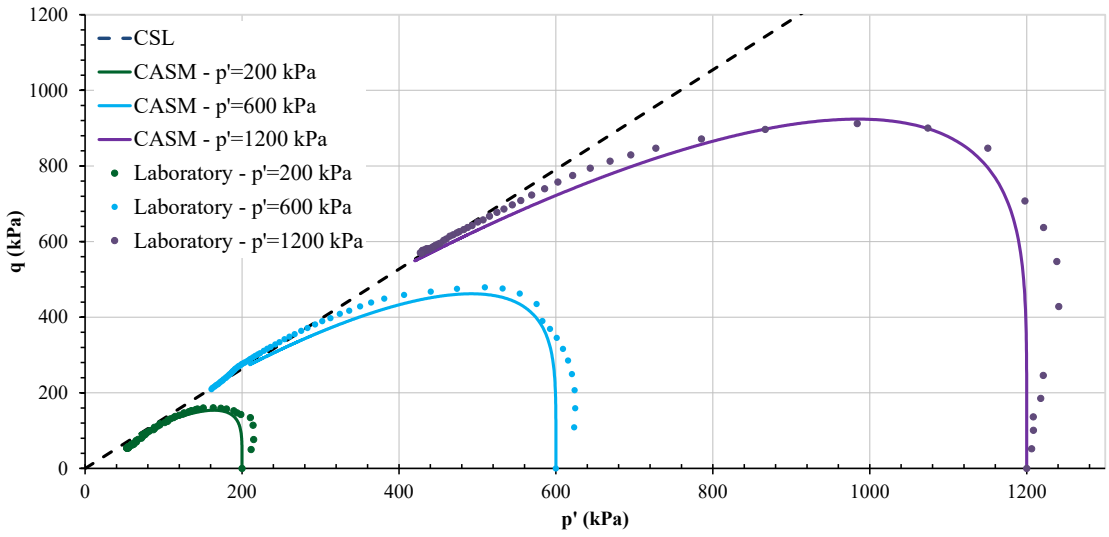

Figure 4.19 – Calibrated versus laboratory p'-q curves.

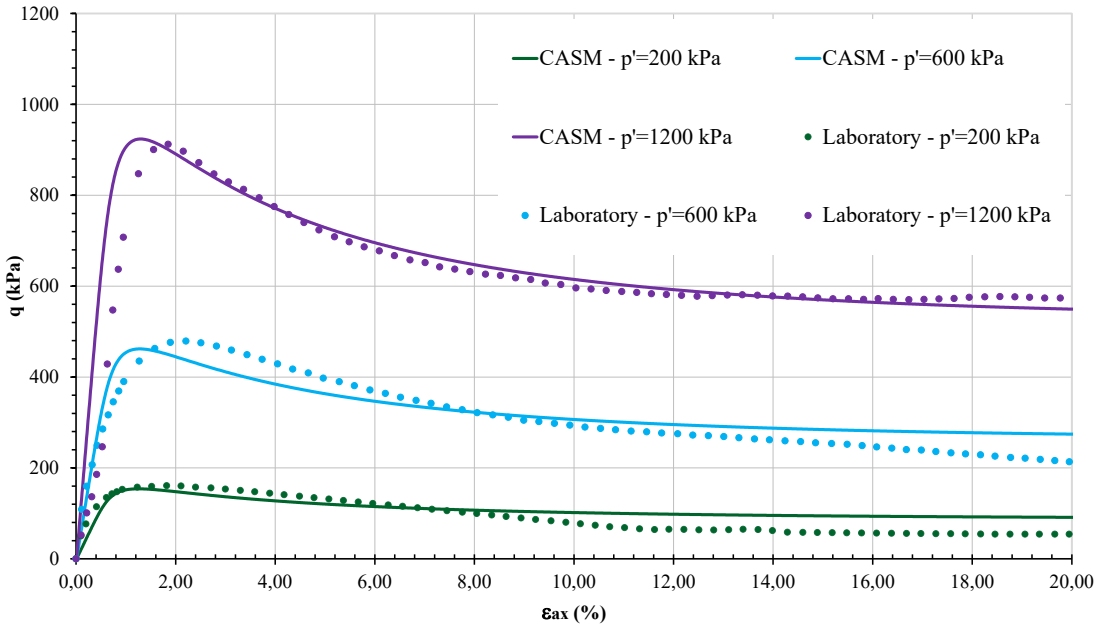

Figure 4.20 – Calibrated versus laboratory ε_{ax}-q curves.

Since the calibration should approximate the behavior of the materials simulated in the laboratory tests, it is shown that in the present example case, a consistent calibration is observed when applying the calibration methodology presented in this work.

5 - CASE STUDY: TAILINGS DAM FAILURE

The selected case study to assess the influence of CASM and NorSand on static liquefaction analyses should be treated as a hypothetical scenario based on a tailings dam failure that occurred in Brazil. This choice was made due to its extensive data availability in the literature (Robertson et al., 2019; Arroyo and Gens, 2021; Viana da Fonseca et al., 2022). Of note, this chapter is a partial reproduction of the paper published by Rógenes et al. (2024b).

The dam was an upstream tailings disposal structure. Construction began in 1976 and extended until 2013 (Robertson et al., 2019). The disposal process continued until July 2016, when the dam reached a height of approximately 85.0 m (Arroyo and Gens, 2021).

In January 2019, the dam suffered a sudden failure. Figure 5.1a and Figure 5.1b depict the dam before and after the rupture. Video cameras captured the exact moment of the rupture (Figure 5.1c), revealing that the process occurred within a few seconds, clearly indicating a liquefaction mechanism.

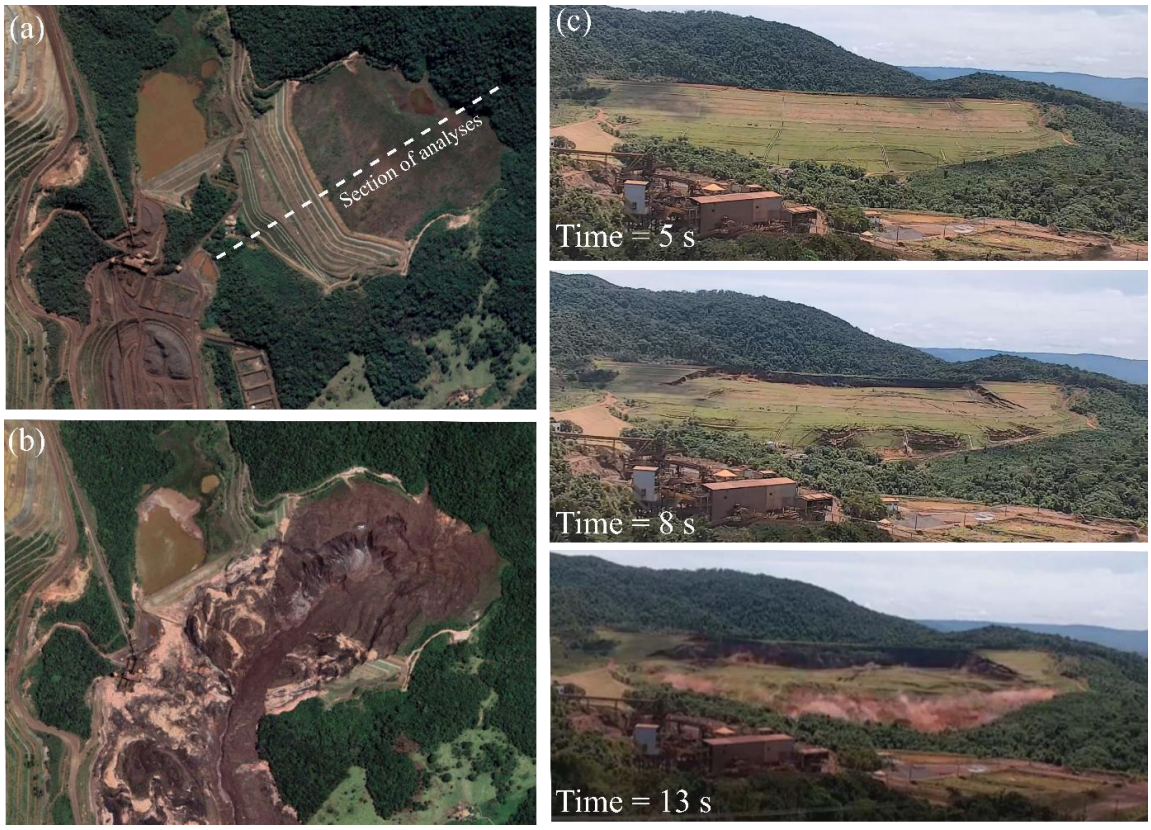

Figure 5.1 – Tailings dam failure: (a) before the failure, (b) after the failure (satellite images from Google Earth), and (c) frontal video images capturing the dam failure and flow (https://www.youtube.com/watch?v=sKZUZQytads).

It is emphasized that the objective of this study was to compare the application of different constitutive models in representing the phenomenon of static liquefaction. Thus, the study does not aim to determine the cause of the rupture in the case study used as a basis, nor does it question the analyses previously conducted by Arroyo and Gens (2021) and Robertson et al. (2019). It is also highlighted that the authors do not make any judgment as to whether the presented models are representative of the actual conditions of the dam before and during the failure.

5.1 - MODEL SETUP

A cross-section of the tailings dam was simulated using a two-dimensional plane strain finite element analysis with Plaxis2D. The geometry and material distribution are well documented and publicly available (Arroyo and Gens, 2021). Figure 5.2 depicts a cross-section near the dam's center, where the failure was initiated based on the camera images captured during the event (Figure 5.1c). This aligns with the critical section used in previous studies on the same case (Robertson et al., 2019; Arroyo and Gens, 2021).

The dam was formed by compacted tailings, compacted fill, ultra-fine iron ore, and drainage material, while the foundation was treated as a homogeneous material. It is worth noting that aforementioned materials did not play a significant role in the dam's failure. Thus, the primary focus of the analysis lies on the tailings, categorized into fine, mixed, and coarse tailings (Robertson et al., 2019; Arroyo and Gens, 2021).

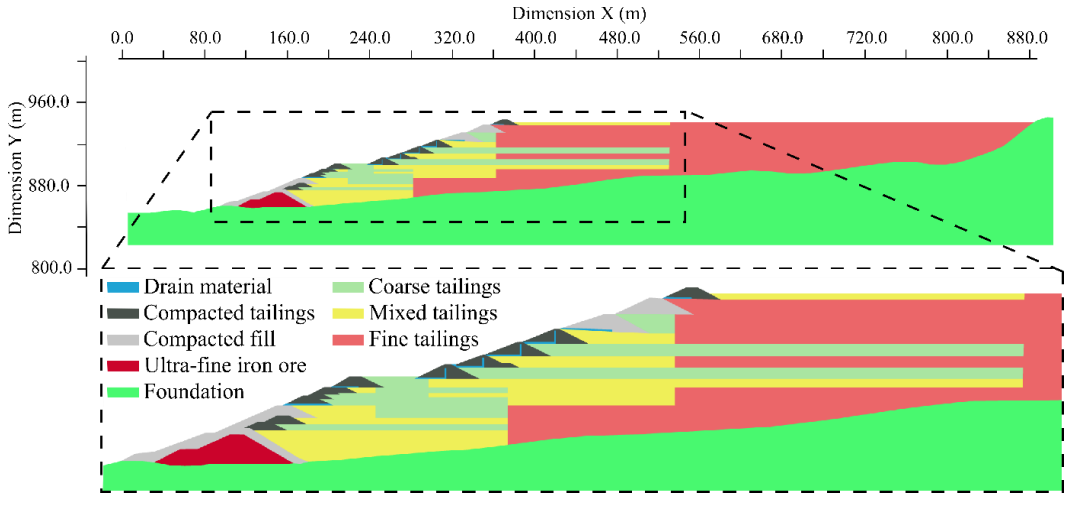

Figure 5.2 - Dam geometry and material distribution of the case study.

5.1.1- TAILINGS – MECHANICAL BEHAVIOR

Arroyo and Gens (2021) and Robertson et al. (2019) categorized the tailings into three groups. Although the classification criteria differed slightly between the two studies, their classifications will be treated as equivalent for numerical analysis comparison. The parameters used by Arroyo and Gens (2021) and Robertson et al. (2019) for the CASM and NorSand models are outlined in Table 5.1 and Table 5.2, respectively. The natural and saturated unit weights considered in the analysis were 22 and 27 kN/m³, respectively, for all tailings. It is important to note that Robertson et al. (2019) did not explicitly provide the state parameter for mixed tailings. This study assumed an average value between the parameters assigned to fine and coarse tailings.

Table 5.1 – CASM model parameters applied to the tailings, taken from Arroyo and Gens (2021).

Symbol	Fine tailings	Mixed tailings	Coarse tailings
Γ	1.20	1.23	1.27
λ	0.053	0.053	0.04
M_{tc}	1.4	1.4	1.4
n	5	6.5	7.5
r	35	15	5
m	2.3	2.3	2.3
κ	0.007	0.007	0.007
ν	0.3	0.3	0.3
OCR	1	1	1

Table 5.2 – NorSand model parameters applied to the tailings, taken from Robertson et al. (2019).

Symbol	Fine tailings	Mixed tailings	Coarse tailings
Γ	1.12	1.04	1.02
λ	0.039	0.039	0.039
M_{tc}	1.38	1.38	1.38
N	0.27	0.27	0.27
χ_{tc}	6	6	6
H_0	160	160	160
H_ψ	1037	1037	1037
G_{ref} (MPa)	100	100	100
n	0.5	0.5	0.5
ν	0.2	0.2	0.2
OCR	1	1	1
ψ	0.06	0.02	-0.02

The parameters outlined in Table 5.1 and Table 5.2 were employed in simulations of undrained triaxial compression tests under initial K_0-consolidation (K_0 = 0.5). Figure 5.3 to Figure 5.5 depict the simulation outcomes alongside select results from triaxial tests conducted on remolded samples, as presented by Viana da Fonseca et al. (2022) and Arroyo and Gens (2021). In these results, η denotes the ratio of the deviatoric stress to the mean effective stress, while η_{K0} and η_{IL} represent this ratio at the initial condition and the instability line in triaxial compression, respectively. It is worth noting that numerical results regarding the fine tailings could not be compared with laboratory data, as Arroyo and Gens (2021) stated that representative samples of the fine tailings were not collected. For reference, laboratory results of the mixed tailings were incorporated into Figure 5.3. Peak and residual strengths for the fine tailings were determined from CPTu tests conducted prior to failure. Moreover, the η_{IL}/M_{tc} value of 0.57 falls within the range reported by Vergaray et al. (2023) for mining tailings.

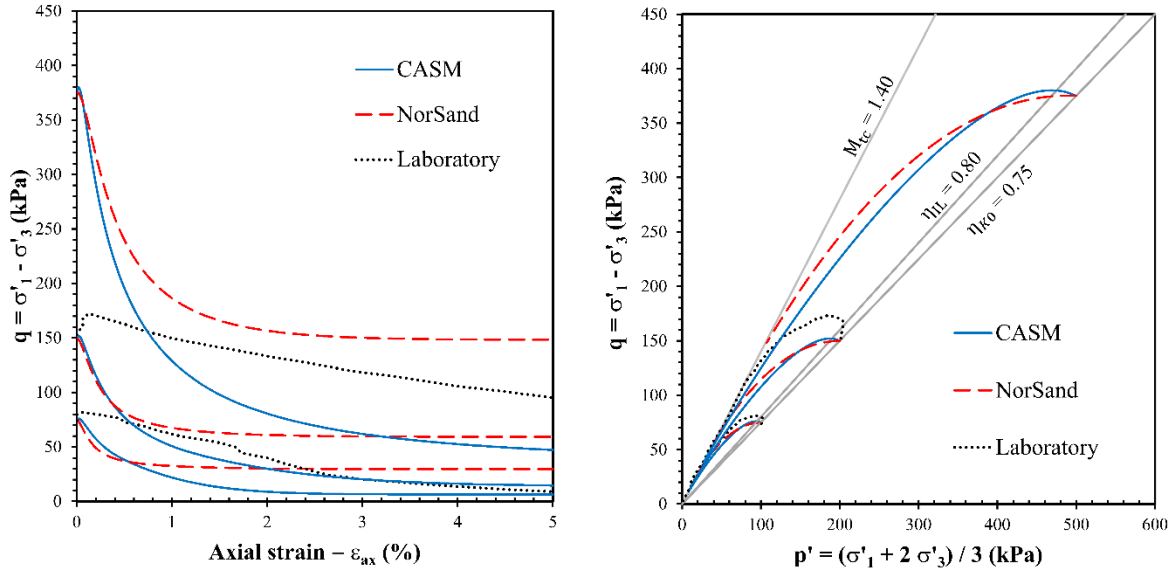

Figure 5.3 - Numerical results for undrained anisotropic triaxial compression tests on fine tailings.

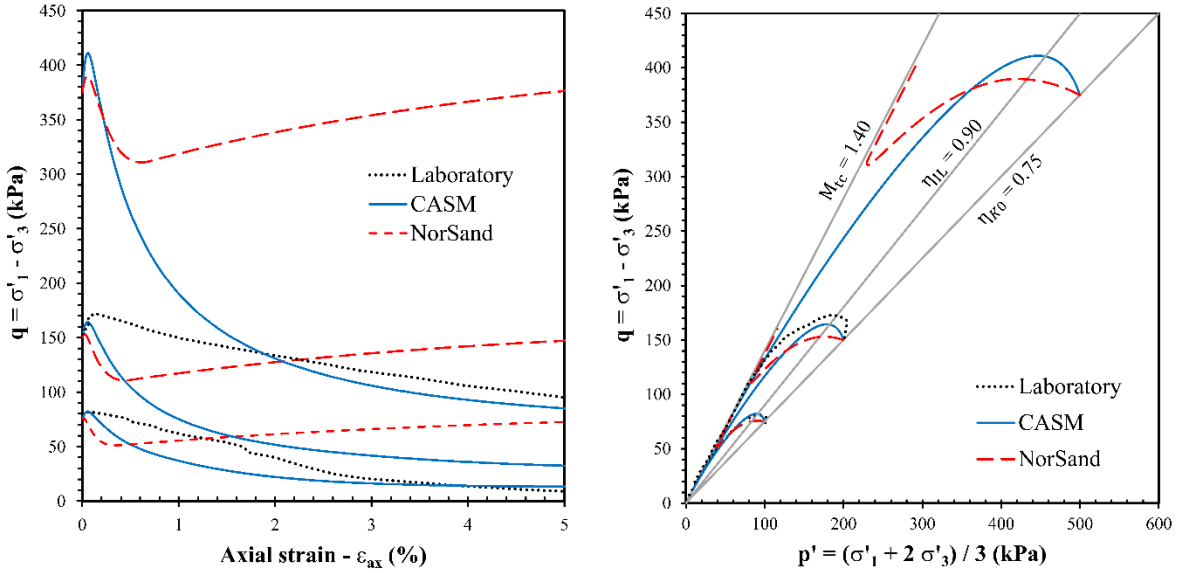

Figure 5.4 - Numerical and laboratory results for undrained anisotropic triaxial compression tests on mixed tailings.

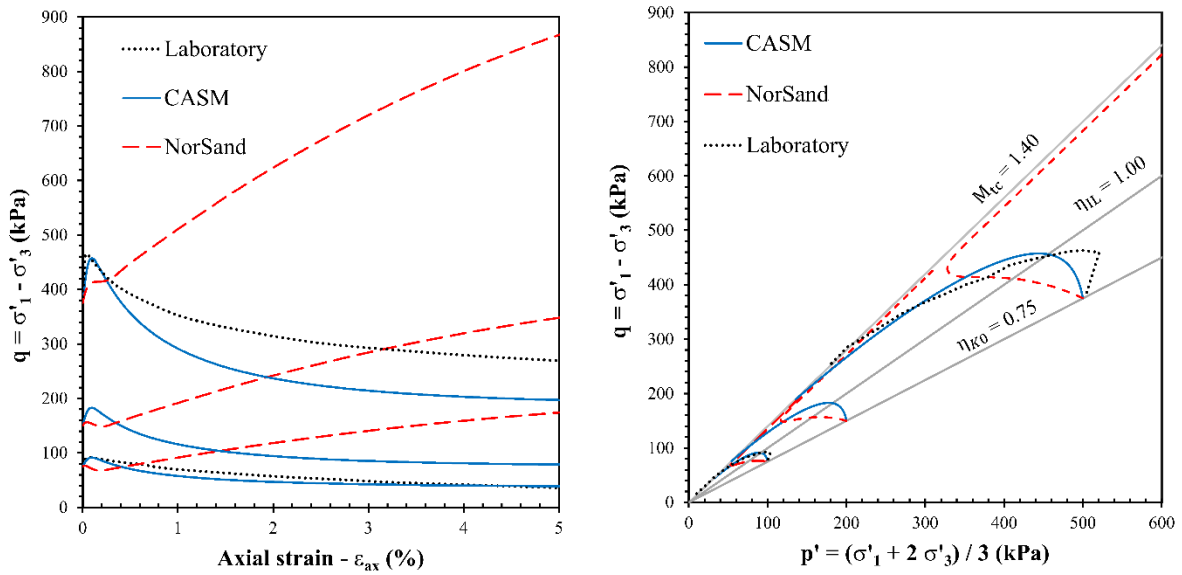

Figure 5.5 - Numerical and laboratory results for undrained anisotropic triaxial compression tests on coarse tailings.

The calibrations for CASM and NorSand are partially consistent with laboratory results. The limited data on material behavior prior to failure and the heterogeneity of the tailings are key aspects that affect the calibration. This discrepancy arises because the calibrations aim to capture field conditions before failure, which are subject to interpretations from field tests and are challenging to replicate in a laboratory test. Furthermore, the calibration also depends on the methodology applied to the chosen constitutive model (Jefferies and Shuttle, 2005; Mánica et al., 2021) and may vary based on engineering judgment, even when using the same database, as recently reported by Reid and Fourie (2024).

While Robertson et al. (2019) calibrated NorSand for triaxial tests and determined the state parameter from CPTu data, Arroyo and Gens (2021) combined field and laboratory tests to calibrate CASM, using triaxial tests to define the critical state line and peak undrained strength, oedometer tests to determine stiffness, and CPTu data to assess residual undrained strength. The calibration procedures are not detailed here for brevity; moreover, cross-checking the calibration was not part of the analysis objectives. Interested readers are referred to the works of Arroyo and Gens (2021) and Robertson et al. (2019) for a comprehensive description of the calibration.

Upon examining the results depicted in Figure 5.3 it is noted that the calibrations for the fine tailings are similar. Both calibrations exhibited contractive behavior throughout the test

and an instability line of approximately 0.8. The primary disparity lies in the residual strength, higher for the NorSand calibration.

Figure 5.4 and Figure 5.5 depict the calibrations for mixed and coarse tailings. Notably, the CASM calibration displays contractive behavior throughout the test, with an instability line of around 0.9 for mixed tailings and 1.0 for coarse ones. However, the NorSand calibration exhibits quasi-steady state behavior (Ishihara, 1993; Yoshimine et al., 1999), transitioning from initial contraction to dilation at high strains, resulting from a state parameter near zero applied to both.

Oedometric compression tests were also simulated to verify the model's ability to control geostatic stress. The stress paths are presented in Figure 5.6, where the initial condition was set at $p' = 100$ kPa and $K_0 = 0.5$. These results show the control of K_0 path by CASM, while NorSand tends to increase the K_0 value, leading to a stress state farther from the instability line. This behavior has also been reported by other researchers (Castonguay and Konrad, 2016; Gomes, 2022; Reid et al., 2022), which justifies avoiding the use of NorSand to generate the stress state before failure, as controlling geostatic stress is an important feature of static liquefaction simulations (Reid et al., 2022, 2023). Given this result and based on the authors' experience, it is better to generate a reasonably accurate stress state using a simple model like Mohr-Coulomb, while maintaining control of the K0 condition, which will govern the stress state in zones prone to instability.

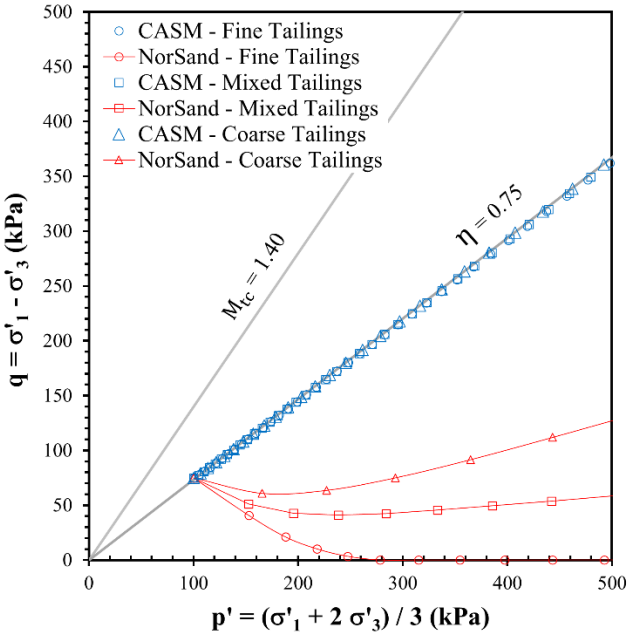

Figure 5.6 - Numerical results for oedometric compression tests.

5.1.2- OTHER MATERIALS – MECHANICAL BEHAVIOR

The compacted tailings, compacted fill, and ultra-fine iron ore were simulated using the Hardening Soil Model (Schanz et al., 1999). Meanwhile, the drain material was represented by the elastoplastic Mohr-Coulomb model. Elastic behavior was assumed for the foundation. The parameters proposed by Arroyo and Gens (2021) were utilized in our analyses and are presented in Table 5.3

Table 5.3 – Mechanical parameters employed to characterize the materials of the embankment and foundation, taken from Arroyo and Gens (2021).

Symbol	Description	Compacted tailings	Compacted fill	Ultra-fine iron ore	Drain	Foundation
E_{50ref} (MPa)	Reference modulus that relates plastic straining due to primary deviatoric loading	17.9	13	13.4	-	-
E_{oedref} (MPa)	Reference modulus that relates plastic straining due to primary compression	17.9	13	13.4	-	-
c' (kPa)	Cohesion	0	10	10	10	-
ϕ' (°)	Friction angle	40	35	35	35	-
ψ_{dil} (°)	Dilation angle	0	0	0	0	-
p_{ref} (kPa)	Reference pressure	100	100	100	-	-
m_s	Parameter that controls the variation of stiffness with confining stress	1	1	1	-	-
E(MPa)	Young modulus	179	130	134	13	470
ν	Poisson's ratio	0.3	0.3	0.3	0.3	0.3
γ (kN/m³)	Unit weight	28	19	19	19	19

5.1.3- HYDRAULIC BEHAVIOR

The hydraulic behavior of the materials was described by Darcy's law, with a constant hydraulic conductivity applied. The soil-water characteristic curve and unsaturated hydraulic conductivity function, following the Van Genuchten model, were also incorporated to capture unsaturated flow behavior. The values presented by Arroyo and Gens (2021), which were derived from laboratory tests and correlations with physical characterization, were adopted in this work. The parameters are summarized in Table 5.4.

Table 5.4 – Hydraulic parameters, taken from Arroyo and Gens (2021).

Symbol	Description	Fine tailings	Mixed tailings	Coarse tailings	Compacted tailings	Compacted fill	Ultra-fine iron ore	Drain	Foundation
S_{res}	Residual degree of saturation	0.15	0.30	0.25	0.06	0.06		0.06	0.06
g_n	Van Genuchten parameter	1.5	2.0	4.0	1.38	1.38		1.38	1.38
g_a (m^{-1})	Van Genuchten parameter	0.18	0.40	0.40	3.83	3.83		3.83	3.83
g_l	Van Genuchten parameter	0.001	0.001	0.001	1.25	1.25		1.25	1.25
k_x (m/s)	Horizontal hydraulic conductivity	1.00E-07	1.70E-06	5.00E-06	5.00E-07	1.20E-09	1.20E-06	1.00E-04	9.31E-07
k_y (m/s)	Vertical hydraulic conductivity	2.00E-08	3.40E-07	1.00E-06	1.00E-07	1.20E-09	1.20E-06	1.00E-04	9.31E-07

5.1.4- FINITE ELEMENT MESH AND BOUNDARY CONDITIONS

A mesh comprising approximately 24,000 15-node triangular elements was employed. The discretization is depicted in Figure 5.7. It is crucial to recognize that both CASM and NorSand are mesh-sensitive to the formation of shear bands, given the brittle nature of the

liquefaction, and they are not formulated with regularization techniques (Mánica et al., 2018; Chen et al., 2023). Therefore, the mesh density was defined based on similar analyses of dam failures due to static liquefaction (Arroyo and Gens, 2021; Mánica et al., 2021; Ledesma et al., 2022; Liu et al., 2024).

Mechanical boundary conditions included constrained horizontal displacement applied to the sides of the model, and constrained horizontal and vertical displacements applied to the bottom boundary as well.

Hydraulic boundary conditions were defined by imposing a constant total head of 848.0 m at the downstream boundary and 941.0 m at the upstream boundary. Additionally, total water head boundary conditions were applied in the reservoir to replicate a lake along the dam construction. It should be noted that rainfall boundary conditions were not considered in the analysis.

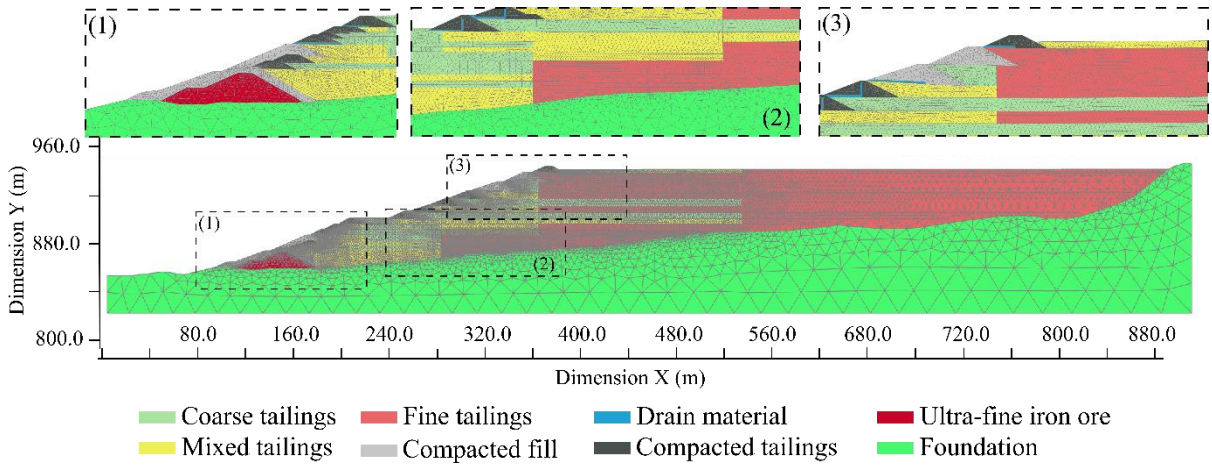

Figure 5.7 - Finite element mesh.

5.1.5- MODELING SEQUENCE

The pre-failure state was achieved through the construction simulation of the dam. The main objective of this simulation was to assess the stress distribution in the tailings prior to failure. The construction simulation was subdivided into 32 stages, with the first stage dedicated to establishing the initial condition of the foundation, intermediate stages representing raises and reservoir filling, and the final stage representing the period during which the dam was out

of operation until immediately before the rupture. This construction simulation employed CASM and the parameters outlined in Table 5.1.

In these simulations, the generation and dissipation of excess pore pressure were accounted for by a consolidation-type calculation available in Plaxis. This method considers the development and dissipation of excess pore pressure over time in saturated materials, while in the unsaturated phase, suction is considered only in the effective stress calculation. For more detailed information, readers are referred to the Plaxis manual (Brinkgreve et al. 2020). The time applied in each stage was defined based on the construction history of the dam up to the moment prior to the rupture, as presented by Arroyo and Gens (2021), which took a total time of 43 years. Figure 5.8 illustrates some of the simulation stages.

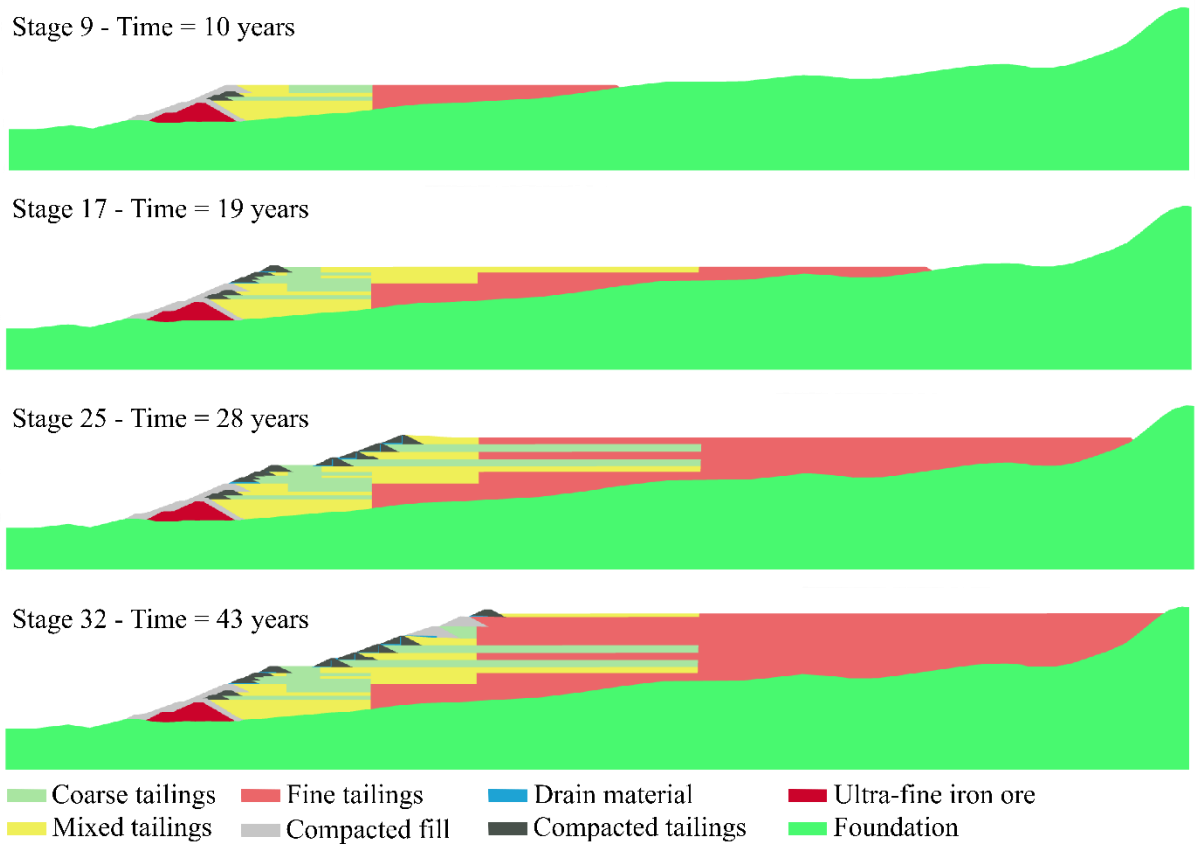

Figure 5.8 - Model geometry of dam construction simulation in different stages.

5.2 - PRE-FAILURE STATE

In Figure 5.9, the distribution of pore water pressures reached prior to rupture is depicted. The numerical results are compared with the values observed in the dissipation conducted during CPTu driving and readings from piezometers installed in the dam, as detailed by Whittle et al. (2022). A good agreement is observed between the numerical results and the field data, highlighting the model's capability to capture the non-hydrostatic condition of pore water pressure.

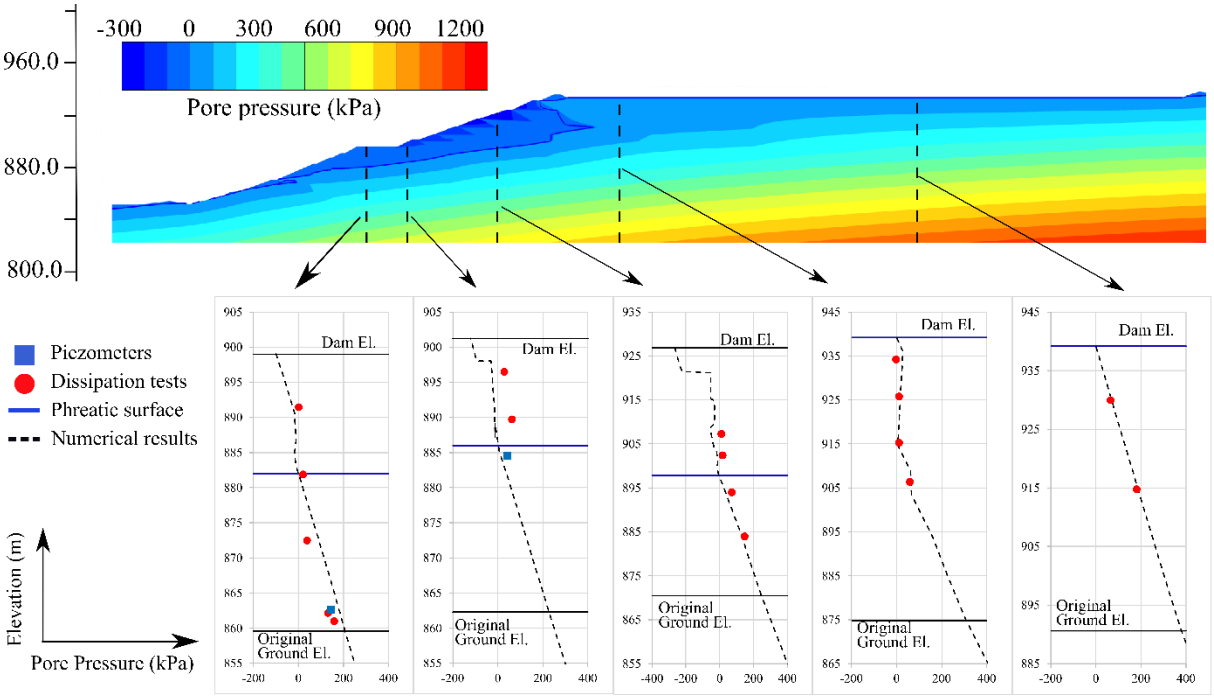

Figure 5.9 - Pore pressure in pre-failure stage.

The stress state in the pre-failure condition is presented through the stress ratio and the mobilized stress ratio in Figure 5.10. The parameters applied to the tailings (Table 5.1) result in a K_0 value of 0.5, leading to a predominant η value of 0.75, as observed in Figure 5.10a. Additionally, there is a zone of lower mobilization (η <0.65) attributed to the setback of the embankments, while a zone of higher mobilization (η >0.75) forms a potential failure surface.

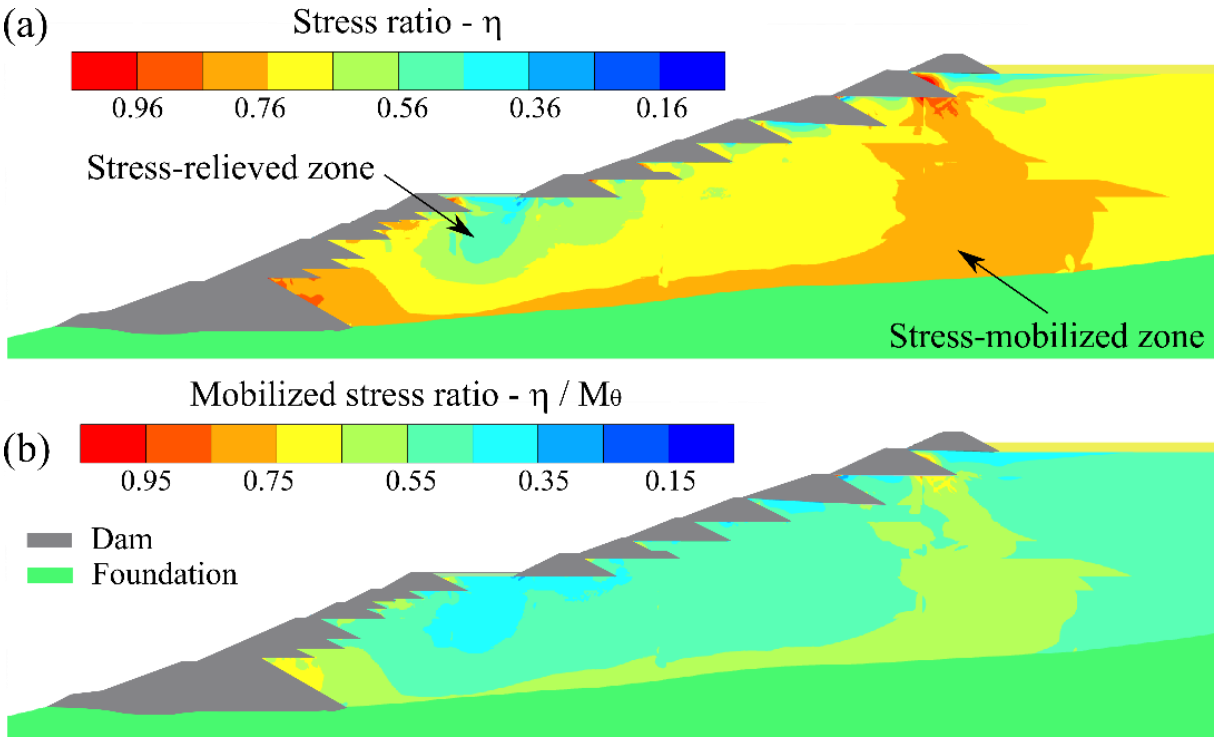

Figure 5.10 - Stress distribution in the pre-failure stage: (a) stress ratio ($\eta = q/p'$) and (b) mobilized stress ratio (η/M_θ).

5.3 - LIQUEFACTION BACK ANALYSIS

At the moment of failure, a drilling operation for an inspection borehole was underway near the dam's crest. Arroyo and Gens (2021) identified this activity as a possible triggering mechanism for the static liquefaction-induced failure. Following the same hypothesis, this section will present a back analysis of the failure, considering a liquefied zone induced by the drilling as the trigger.

It is estimated that the borehole depth was approximately at the foundation level when failure initiated. Arroyo and Gens (2021) demonstrated through numerical analyses that the water column's pressure could induce liquefaction of the material around the borehole. Following the dimensions proposed by Arroyo and Gens (2021), localized liquefaction was considered in a region measuring 3 m in height and 1 m in width (Figure 5.11). Arroyo and Gens (2021) did not provide the procedure for determining these dimensions. This approach aims to verify if liquefaction in a limited zone could propagate throughout the domain and cause a complete failure. A similar procedure was adopted by Ledesma et al. (2022) to back-analyze the failure of the Fundão dam due to the extrusion of fine tailings.

Arroyo and Gens (2021) prescribed local liquefaction by changing some parameters of the material in the liquefied zone induced by drilling (Figure 5.11). In this work, the local disturbance was simulated by prescribing a uniform horizontal contraction (compressive horizontal strain) across the entire 3m x 1m region. Plaxis internally converts the horizontal contraction strain into nodal displacements for each node within the region. This procedure was adopted to facilitate a direct comparison between CASM and NorSand results by eliminating the need to change material parameters. An analogous approach to induce local liquefaction was used by Ledesma et al. (2022).

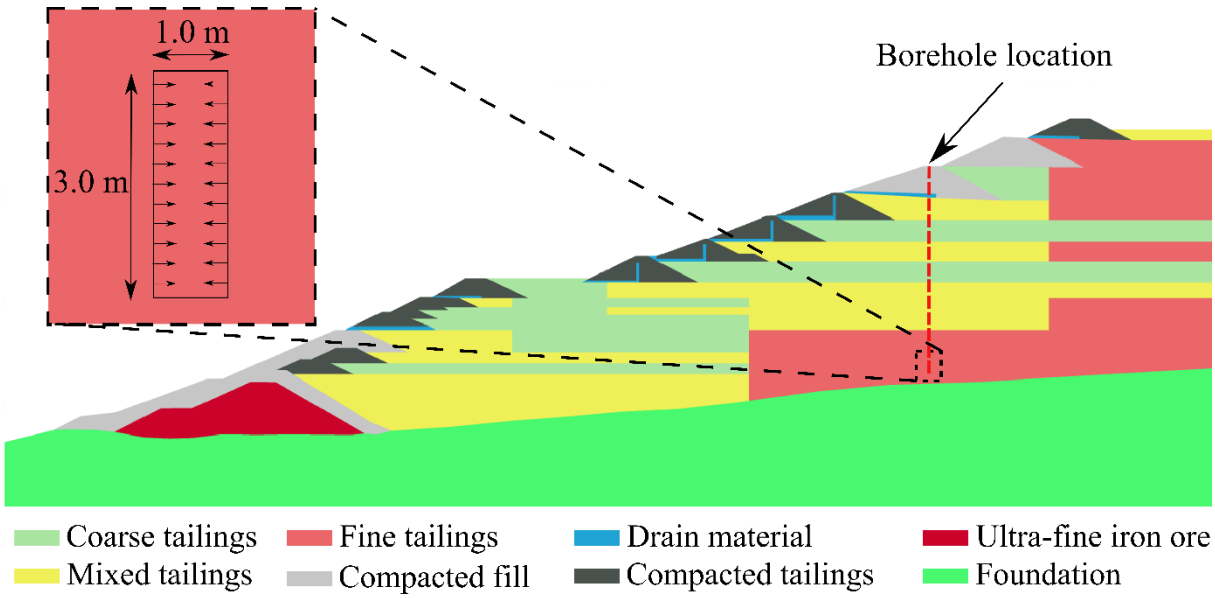

Figure 5.11 - Details of the liquefied zone induced by drilling.

It is important to mention that the two-dimensional analyses provide only an approximation of the impacts induced by drilling, given the three-dimensional nature of the liquefied zone around the borehole. The analyses presented here primarily aim to compare the CASM and NorSand models rather than provide an assessment of the causes of failure. Furthermore, Arroyo and Gens (2021) conducted three-dimensional analyses simulating the trigger using a zone with similar geometry but only 1 m in width, which resulted in the same failure mechanism. This emphasizes the capability of the 2D analysis to provide a reliable approximation.

It is emphasized that the objective of this study was to compare the application of different constitutive models in representing the phenomenon of static liquefaction. Thus, the study does not aim to determine the cause of the rupture in the case study used as a basis, nor

does it question the analyses previously conducted by Arroyo and Gens (2021) and Robertson et al. (2019). It is also highlighted that the authors do not make any judgment as to whether the presented models are representative of the actual conditions of the dam before and during the rupture

5.3.1- CASM SIMULATION

In the CASM simulation, when a horizontal strain of 0.3% is applied to the liquefied zone induced by drilling, equivalent to a horizontal displacement of 3 mm, the model becomes unstable, and the dam fails. The simulation results are shown in Figure 5.12 and are presented in terms of a normalized stress ratio (η/M_θ). It is important to note that the parameter η/M_θ is analogous to the inverse of a local safety factor (FS_{Local}) (Equation 5-1). Therefore, the local failure condition is reached with $\eta/M_\theta = 1$.

$$FS_{Local} = \frac{\tau_f}{\tau_{mob}} = \frac{\sigma'_n \tan\phi'}{\tau_{mob}} \approx \frac{p' M_\theta}{q} = \frac{M_\theta}{\eta} \qquad \text{Equation 5-1}$$

where τ_f is the shear strength at failure, τ_{mob} is the mobilized shear strength, and σ'_n is the normal stress at the failure plane.

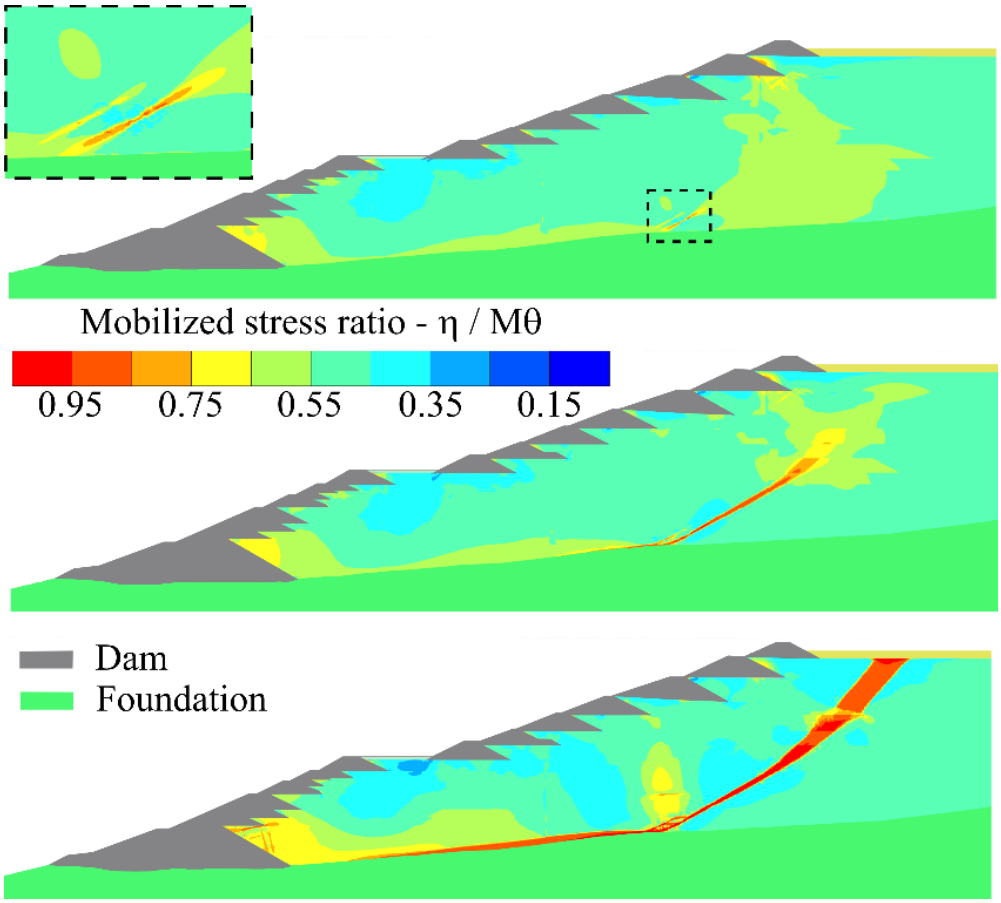

Figure 5.12 - Mobilized stress ratio resulting from liquefaction failure triggered by the borehole using CASM.

Figure 5.12 shows that the imposed horizontal strain disturbs the stress state in the vicinity of the borehole. The mechanism initiates from the area surrounding the borehole and quickly propagates internally through the zone with the highest stress mobilization, ultimately leading to the structure's liquefaction. The state parameters before and after failure are presented in Figure 5.13 highlighting the material's tendency to undergo a reduction in state parameter, reaching the critical state at the slip surface. Of note, the initial state parameter is related to the spacing ratio used in the calibration (Figure 2.9).

Figure 5.14 presents the results of incremental displacements and the deformed model. The numerical results show a slope failure within the dam, starting from the crest and extending to an area just above the starter dam. The dam crest dropped while the area above the toe region bulged outwards. Additionally, the notable rigid body movement experienced by the embankments in the dam's center is noteworthy. All these aspects are consistent with the recorded images of the failure (Figure 5.1c).

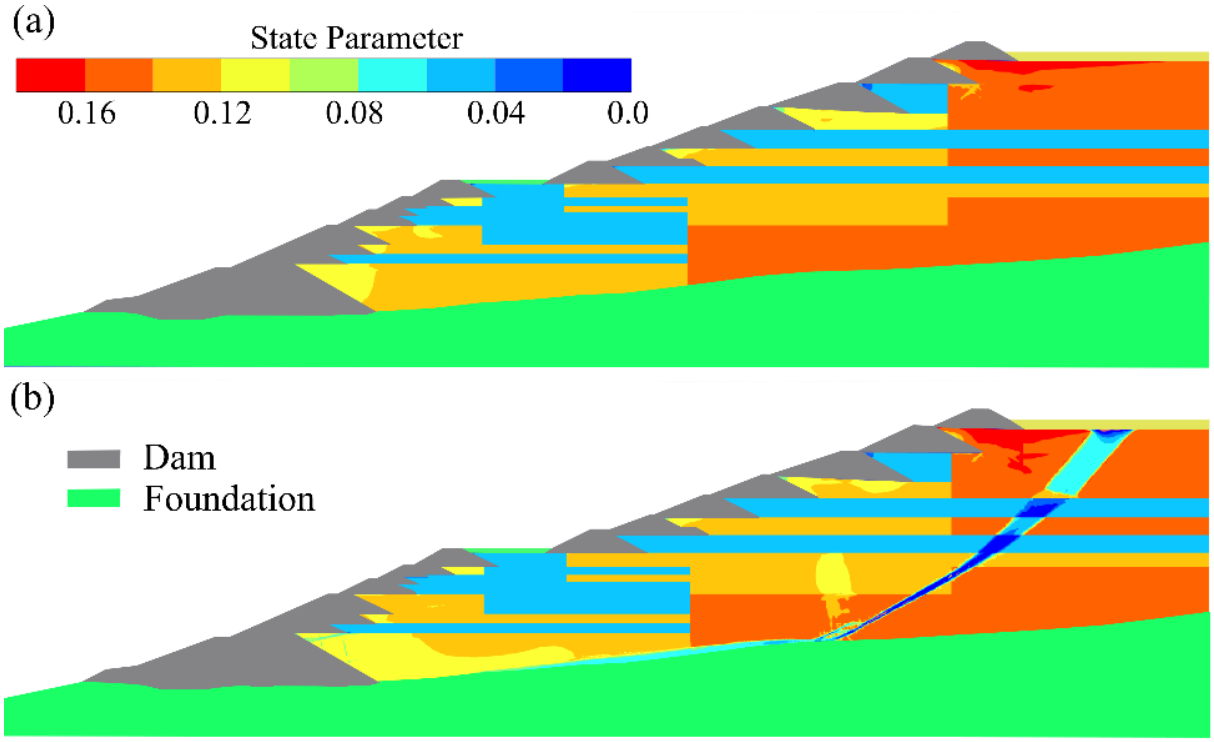

Figure 5.13 - Evolution of state parameter due to liquefaction failure triggered by the borehole using CASM: (a) initial condition and (b) failure condition.

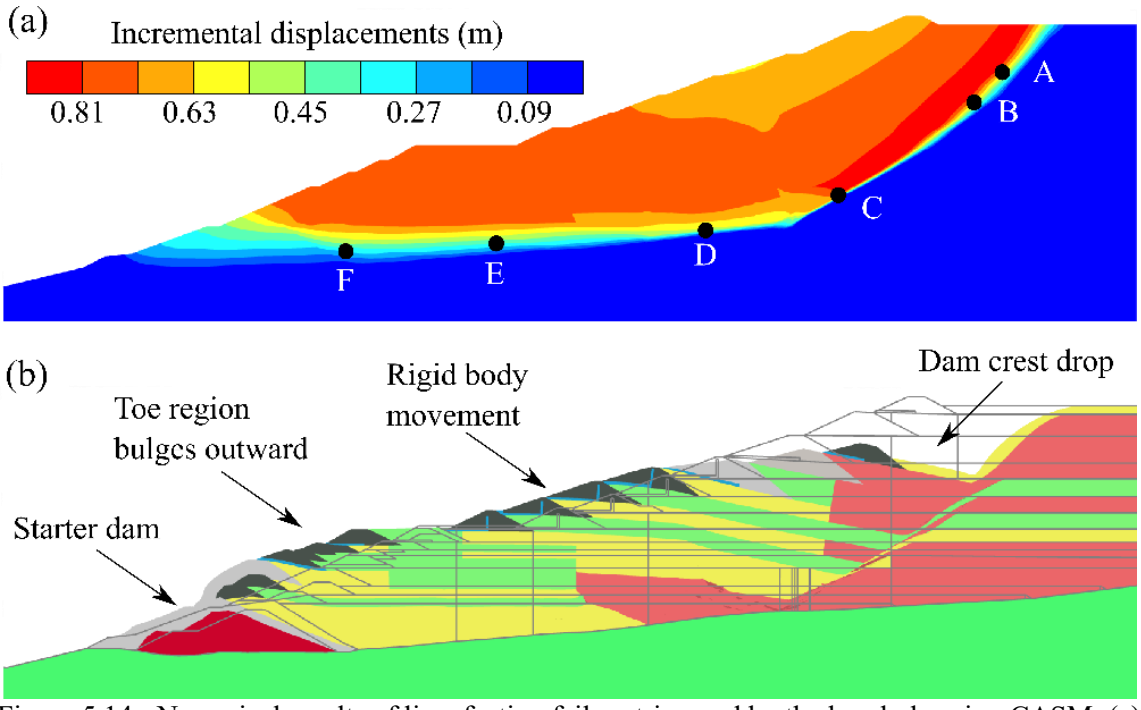

Figure 5.14 - Numerical results of liquefaction failure triggered by the borehole using CASM: (a) incremental displacements and (b) deformed mesh scaled by a factor of 10.

In Figure 5.15 stress paths at control points are depicted, with the locations of these points shown in Figure 5.14a. All points exhibit a substantial loss of strength, indicating a flow

liquefaction-type failure. The critical state line and instability lines presented were derived from anisotropic triaxial compression tests (Section 5.1.1) and should be regarded as reference values only, as these parameters are subject to variation with the Lode angle (Lu et al., 2017; Reid et al., 2023).

Points A, C, and D (Figure 5.15a) are located in the fine tailings. It is observed that the initial stress ratios are slightly different among them. Point A, located below the K_0 line ($\eta < 0.75$), shows an increase in strength until reaching the instability line ($\eta \approx 0.8$), followed by a decrease in strength. Point C exhibits a similar behavior; however, as it is initially closer to the instability line, it shows less strength increase compared to Point A. Lastly, Point D is initially situated on the instability line, so it exhibits a loss of strength from the outset. All these results indicate that the fine tailings were in a potentially unstable stress state, which significantly contributed to the mechanism's development in response to minor perturbations.

In Figure 5.15b, point B is within the coarse tailings, whereas points E and F are in the mixed tailings. Both materials initially demonstrate an increase in strength until reaching the instability line, followed by a subsequent decrease in strength. These results indicate that, despite having higher undrained strength than fine tailings, the mixed and coarse tailings also contribute to the mechanism's development, as they exhibit a pronounced loss of strength.

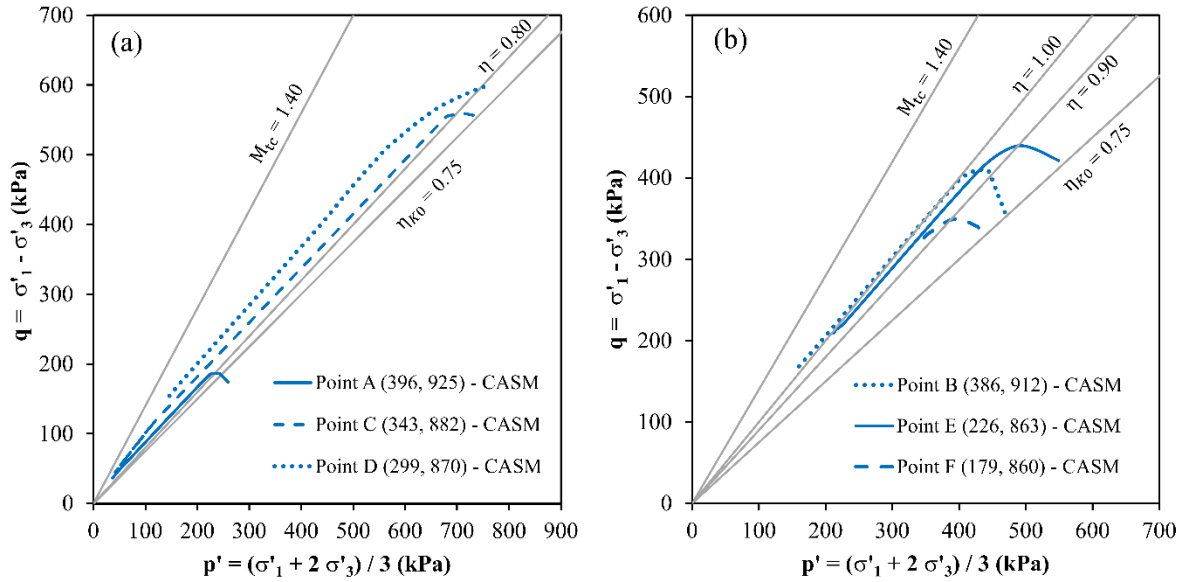

Figure 5.15 - Local soil response to liquefaction failure triggered by the borehole using CASM: (a) fine tailings (points A, C, and D), (b) coarse tailings (point B), and mixed tailings (points E and F). Representative points are located on the failure surface (see Figure 5.14a). The coordinates of the points, in meters, are indicated in the plot legends.

5.3.2- NORSAND SIMULATION

The simulation using NorSand initiates the liquefaction failure mechanism by imposing a horizontal strain of 3.3% in the vicinity of the borehole. This value is eleven times higher than the disturbance required to trigger liquefaction with CASM. Nonetheless, it still constitutes a minor perturbation, equivalent to a horizontal displacement of 33 mm in the borehole's influence zone.

The failure mechanism is presented in Figure 5.16. It is observed that the mechanism initiates from the vicinity of the borehole and propagates globally, producing a similar outcome to that obtained in CASM. The contours of displacement increments are particularly useful for observing the localization of deformations within the soil during failure. Although the values obtained using NorSand (Figure 5.16c) are lower than those from CASM (Figure 5.14a), it should be noted that these values represent displacements calculated for a single calculation step, reflecting differences in the numerical procedures.

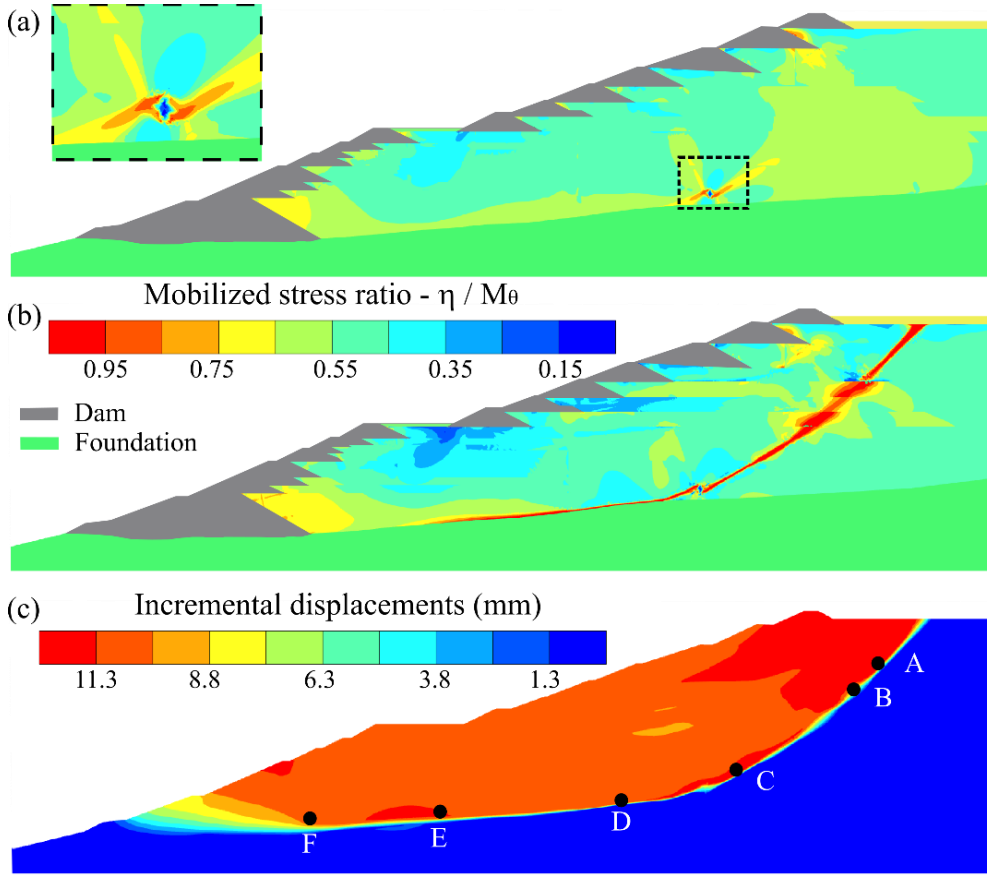

Figure 5.16 - Numerical results of liquefaction failure triggered by the borehole using NorSand: (a) and (b) Mobilized stress ratio, and (c) incremental displacements.

Figure 5.17 presents the state parameters before and after failure. The state parameter evolves during the deformation and reaches a value near zero (i.e., on the CSL) at the failure surface. It should be recognized that the differences in the initial state parameters observed between Figure 5.14 and Figure 5.17 result from the different calibrations adopted by Arroyo and Gens (2021) and Robertson et al. (2019). These differences arise from the interpretation of field tests as well as variations in the constitutive model formulations, such as considerations regarding whether the virgin compression line is parallel to the critical state line or the existence of infinite virgin compression lines, as discussed in Sections 2.3.1 and 2.3.2, for example.

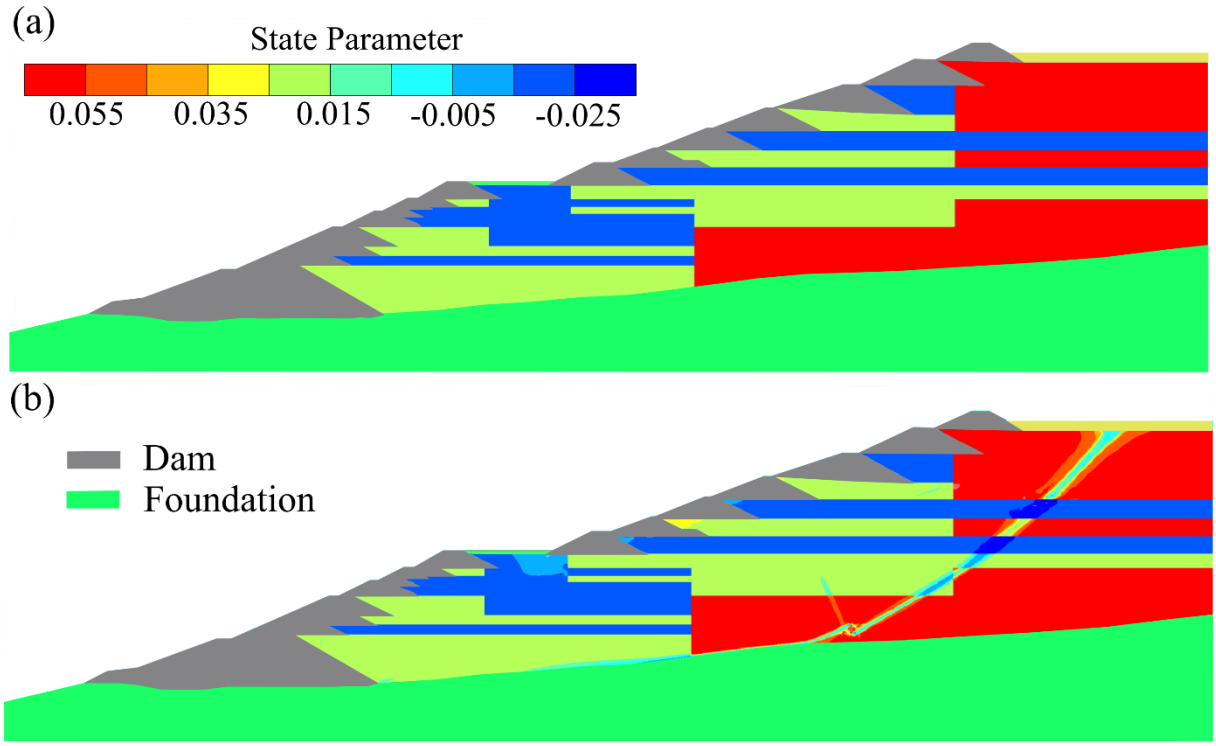

Figure 5.17 - Evolution of state parameter due to liquefaction failure triggered by the borehole using NorSand: (a) initial condition and (b) failure condition.

Stress paths obtained at control points (Figure 5.16c) with NorSand are presented in Figure 5.18. The control points shown in Figure 5.14 were retained, enabling a direct comparison with the results observed in CASM.

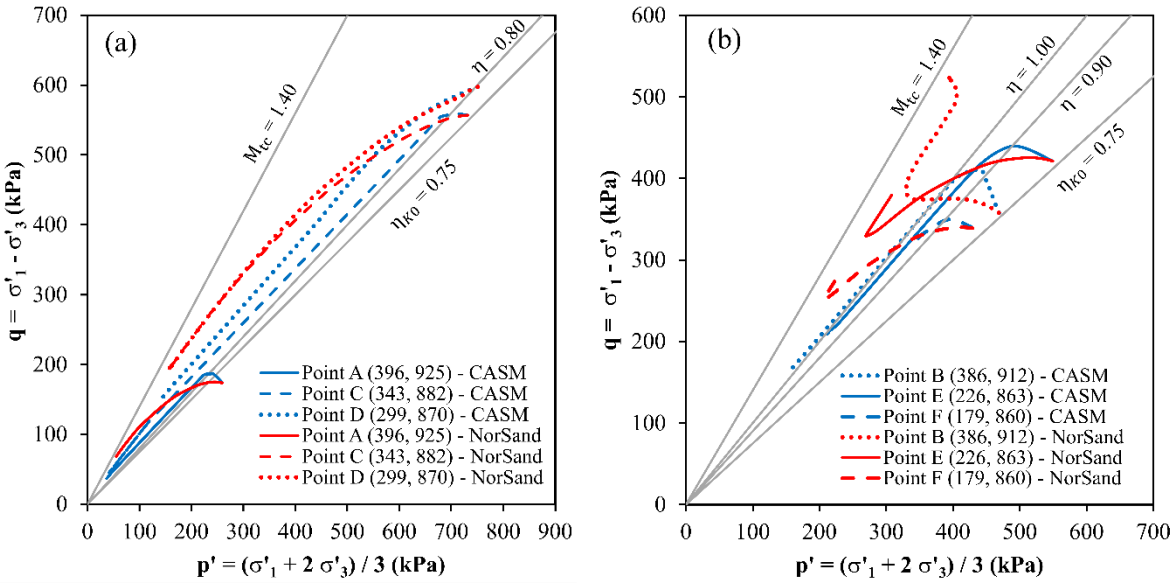

Figure 5.18 - Local soil response to liquefaction failure triggered by the borehole using NorSand in comparison with CASM results: (a) fine tailings (points A, C, and D), (b) coarse tailings (point B), and mixed tailings (points E and F). Representative points are located on the failure surface (see Figure 5.16a and Figure 5.14c). The coordinates of the points, in meters, are indicated in the plot legends.

In Figure 5.18a, it is noticeable that the fine tailings exhibit similar behavior in both models. Points A, C, and D show a significant loss of strength, indicating that the fine tailings underwent a complete liquefaction failure.

The mixed and coarse tailings exhibit more divergent behavior, as presented in Figure 5.18b. Results from NorSand initially show a more pronounced loss of strength than CASM. However, NorSand demonstrates a strength gain in the residual condition, whereas CASM exhibits only a decrease in strength.

The state parameter derived from the calibrations of Arroyo and Gens (2021) and Robertson et al. (2019) results in higher values for CASM compared to NorSand (Figure 5.14 and Figure 5.17), which might be primarily responsible for the difference in residual strength observed in stress paths. Given the adopted set of model parameters, CASM appears more brittle than NorSand under undrained conditions, requiring a smaller perturbation to initiate failure.

Despite the differences in peak and residual strength observed between the two models, the failure mechanism was captured similarly. This finding suggests that when assessing a dam's susceptibility to liquefaction, the choice of constitutive model is less important than the model's ability to represent the brittle behavior and sudden strength loss due to pore pressure generation after crossing the instability line. These results are in agreement with the findings of Liu et al. (2024).

6 - HYPOTHETICAL TRIGGERS

The numerical model under pre-failure conditions, presented in Section 5.2, was employed to assess two hypothetical actions that could induce liquefaction in the structure: dam loading and gravity increase. These analyses evaluate the structure's vulnerability before failure, considering the difficulty in predicting a specific trigger, and have been applied by different researchers (Sottile et al., 2021; Ledesma et al., 2022; Gomes, 2022; Liu et al., 2024). Of note, this chapter is a partial reproduction of the paper published by Rógenes et al. (2024b).

The trigger simulating a load on the dam involves applying a vertical load on the ground surface, throughout the tailings reservoir's extent. This simulation aims to represent the effect of a potential dam raise. On the other hand, the increase in gravity entails a rise in gravity acceleration. Although not physically possible, the gravity increase amplifies forces across all model regions, triggering static liquefaction in the most vulnerable areas.

The triggers analyzed are not intended to represent a probable or realistic scenario; instead, they should be understood as a numerical experiment to assess the structure's vulnerability. The level of disturbance associated with each trigger can be interpreted as engineering estimates of the dam's susceptibility to static liquefaction (Ledesma et al., 2022).

A general definition of the safety factor (*FS*) is given by Baecher (1987) as the ratio of capacity to demand (Equation 6-1). This can be expressed in many ways, including forces, moments, stresses, and displacements. In this context, the disturbances that triggered the failure will be used to estimate safety factors based on load and gravity, given by the ratio between critical and actual values. These safety factors are intended to facilitate a direct comparison of results between the two models used. It should be noted that these safety factors should not be interpreted as equivalent to other traditional methodologies, such as limit equilibrium and strength reduction factor (*SRF*).

$$FS = \frac{Capacity}{Demand} \qquad \text{Equation 6-1}$$

6.1 - DAM LOADING

The results derived from CASM are depicted in Figure 6.1 and Figure 6.2, which shows the progression of the failure mechanism in different calculation steps. Upon application of the load, multiple shear bands emerge (Figure 6.1a and Figure 6.2a). Failure is observed upon the application of a 109 kPa load. This mechanism propagates to the unconfined region downstream of the dam, culminating in the formation of a deep failure surface that encompasses the entire structure (Figure 6.2b and Figure 6.2d).

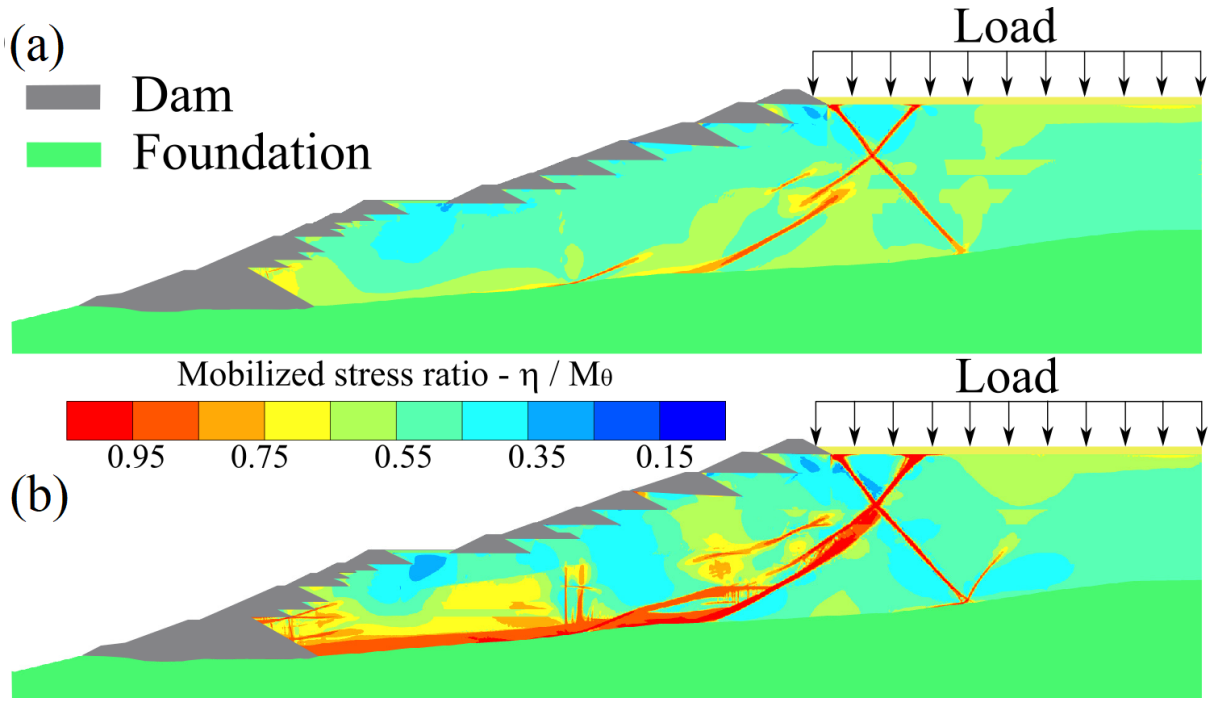

Figure 6.1 - Evolution of liquefaction failure triggered by dam loading across different calculation steps, mobilized stress ratio using CASM: (a) onset of failure, and (b) end of simulation.

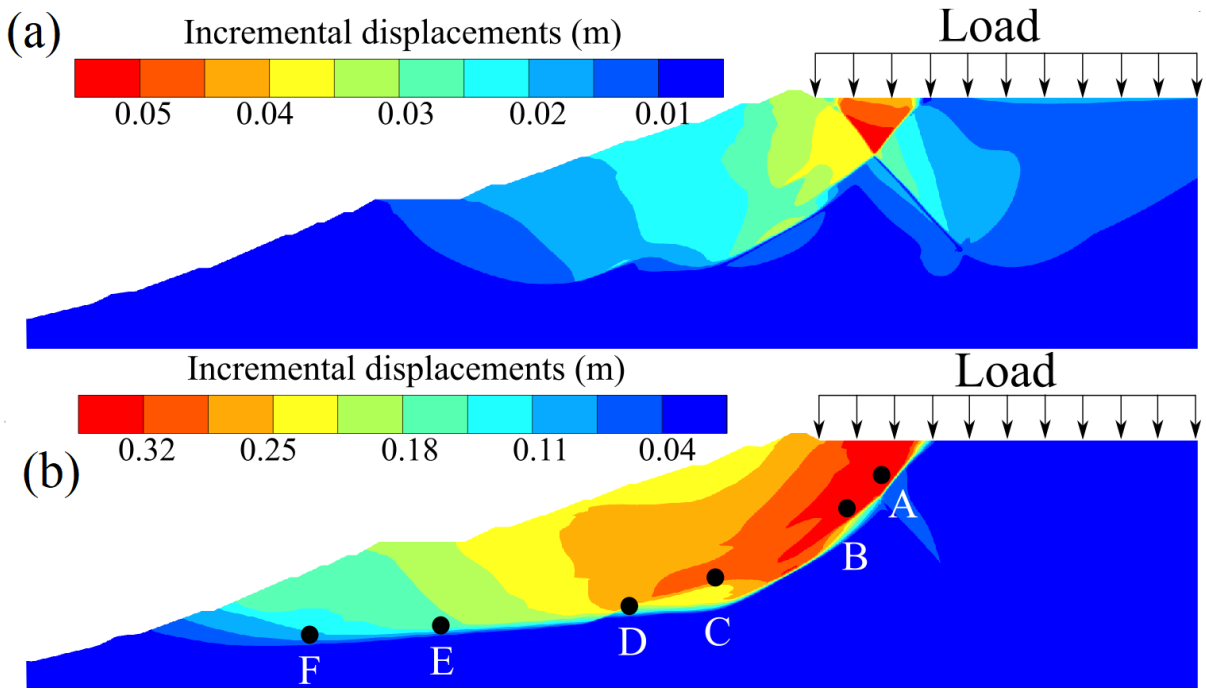

Figure 6.2 - Evolution of liquefaction failure triggered by dam loading across different calculation steps, incremental displacements using CASM: (a) onset of failure, and (b) end of simulation.

NorSand also exhibits a mechanism similar to that observed in the previous analysis, as presented in Figure 6.3 and Figure 6.4. In contrast to CASM, even in the initial perturbation, a shallower failure wedge is observed in the downstream direction of the dam (Figure 6.3a and Figure 6.4a). This mechanism evolves and begins to encompass a deeper surface (Figure 6.3b and Figure 6.4b). The critical load reached is 219 kPa, twice the value obtained in CASM.

Notably, both models generated failure mechanisms with a geometry similar to what was observed in the simulations of a trigger induced by the borehole, thus passing through the region of highest mobilized stresses during the pre-failure stage (Figure 5.10). This finding emphasizes the significance of the initial stress state as a reliable indicator of the regions most prone to liquefaction development.

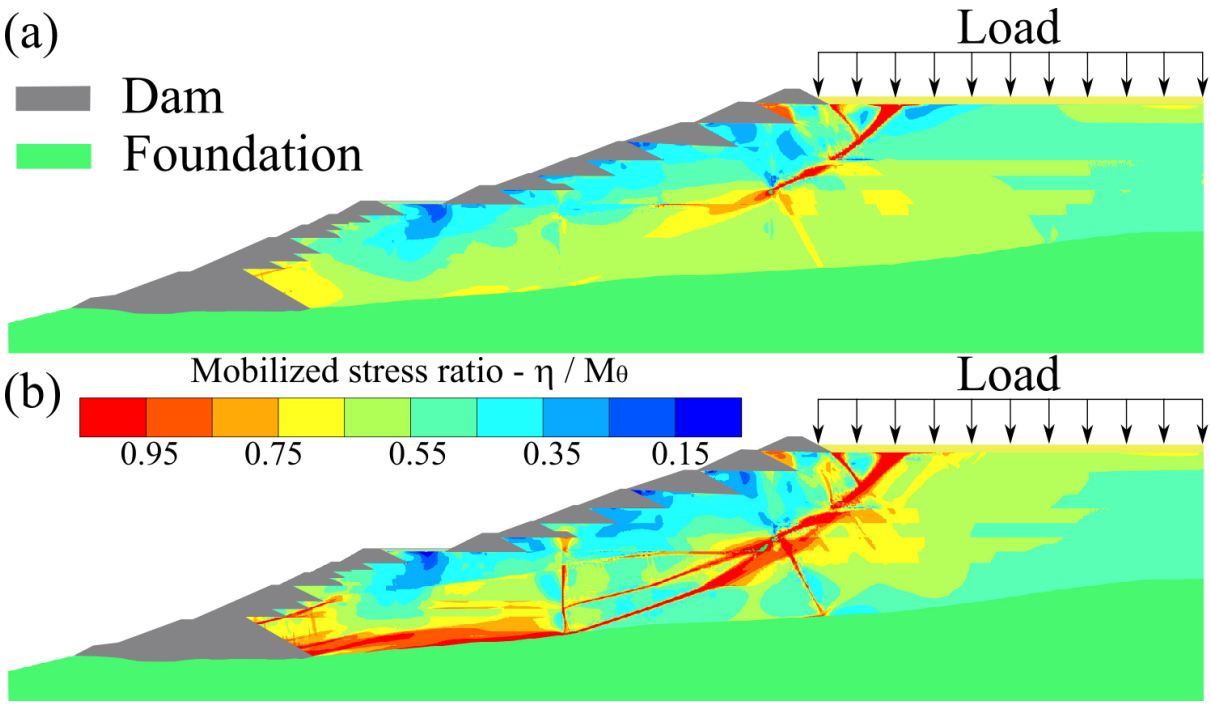

Figure 6.3 - Evolution of liquefaction failure triggered by dam loading across different calculation steps, mobilized stress ratio using NorSand: (a) onset of failure, and (b) end of simulation.

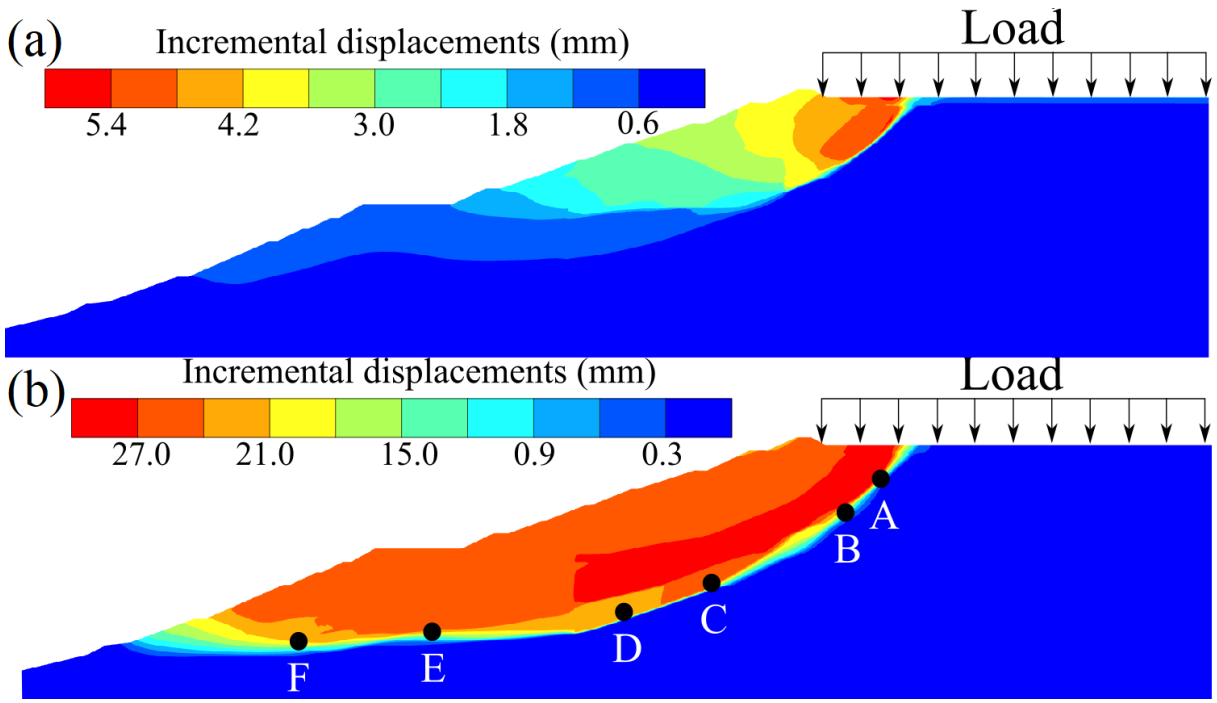

Figure 6.4 - Evolution of liquefaction failure triggered by dam loading across different calculation steps, incremental displacements using NorSand: (a) onset of failure, and (b) end of simulation.

The stress paths obtained at monitoring points (Figure 6.2b and Figure 6.4b) are depicted in Figure 6.5. Overall, a similar pattern of behavior to that seen in the trigger induced by the borehole is observed. In CASM, all tailings undergo static liquefaction failure, whereas in NorSand, while the fine tailings experience total liquefaction, the mixed and coarse tailings show a transition from initial contraction to dilation. Notably, despite differences in stress paths, particularly for the mixed and coarse tailings, the mechanisms develop similarly in both models.

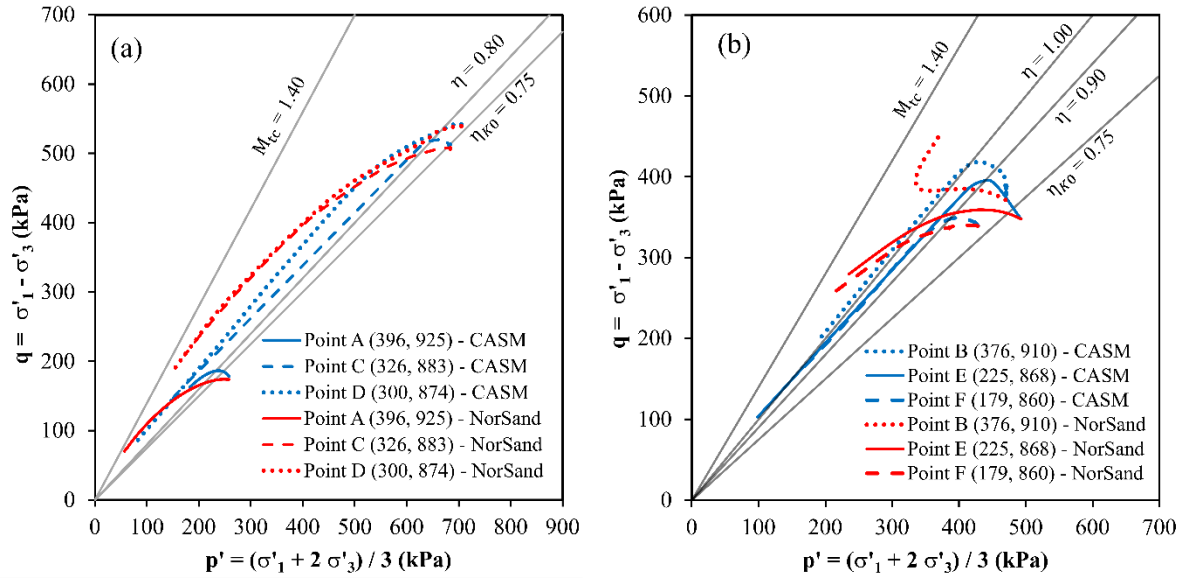

Figure 6.5 - Local soil response to liquefaction failure triggered by dam loading: (a) fine tailings (points A, C, and D), (b) coarse tailings (point B), and mixed tailings (points E and F). Representative points are located on the failure surface (see Figure 6.2b and Figure 6.4d). The coordinates of the points, in meters, are indicated in the plot legends.

The critical loads that trigger the liquefaction mechanism can be converted into an equivalent height of the tailings layer over the dam. This allows for estimating a safety factor based on the critical dam height (Itasca, 2019), as outlined in Equation 6-2.

$$FS_{Load} = \frac{Critical\ Height}{Dam\ Height} = \frac{\frac{Critical\ Load}{Unit\ Weight} + Dam\ Height}{Dam\ Height} \qquad \text{Equation 6-2}$$

Applying the dam height of 85 m (Section 5), unit weight of 27 kN/m³ (Section 5.1.1), and critical loads of 109 kPa and 219 kPa to Equation 6-2, safety factors of 1.05 and 1.10 are

obtained for the CASM and NorSand models, respectively. These results are consistent with those reported by Whittle et al. (2022), who used limit analysis, and indicate the critical condition of the dam, as they are below the minimum safety factor of 1.3 required by Brazilian regulations (ANM, 2022). It should be noted that the current factor of safety criterion was defined after this failure.

6.2 - GRAVITY INCREASE

The development of the failure mechanism in different calculation steps of the gravity increase simulation is depicted in Figure 6.6 and Figure 6.7. Upon increasing gravity in CASM, two mechanisms initially occur in the upper and lower regions of the dam (Figure 6.6a and Figure 6.7a). As the calculation progresses, a deeper mechanism emerges (Figure 6.6b and Figure 6.7b). Failure begins in the layers of fine tailings until a global failure surface is triggered (Figure 6.6c and Figure 6.6f).

The maximum additional increase in gravity was 7%. The final failure mechanism is similar to those observed in previously tested triggers. The initiation of the mechanism by the fine tailings emphasizes the importance of these layers for the initiation and propagation of liquefaction, as highlighted by other researchers (Morgenstern et al., 2016; Ledesma et al., 2022; Liu et al., 2024).

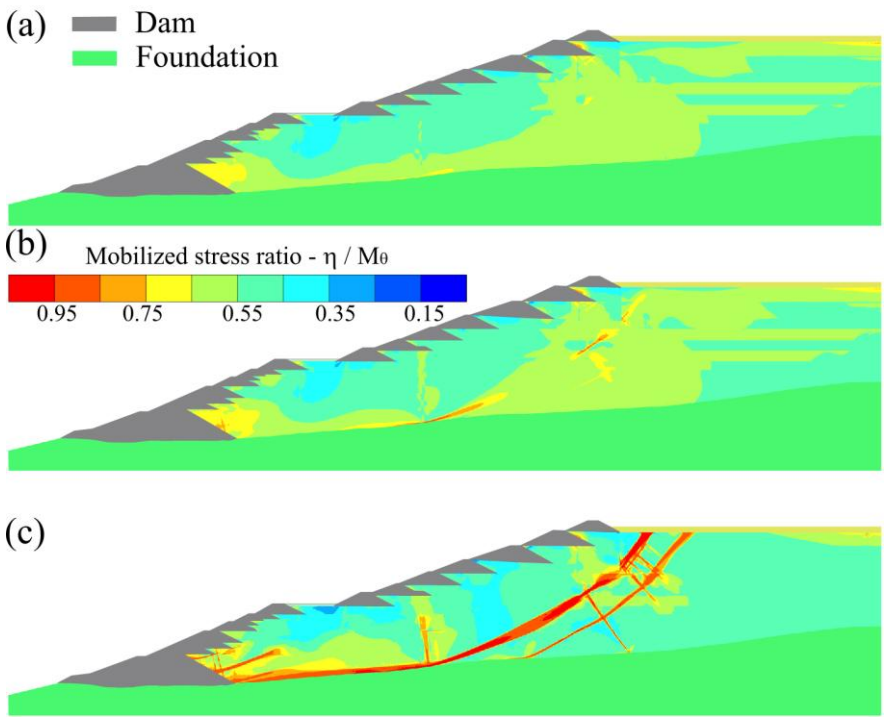

Figure 6.6 - Evolution of liquefaction failure triggered by gravity increase across different calculation steps, results using CASM: mobilized stress ratio. (a) onset of failure, (b) intermediate stage, and (c) end of simulation.

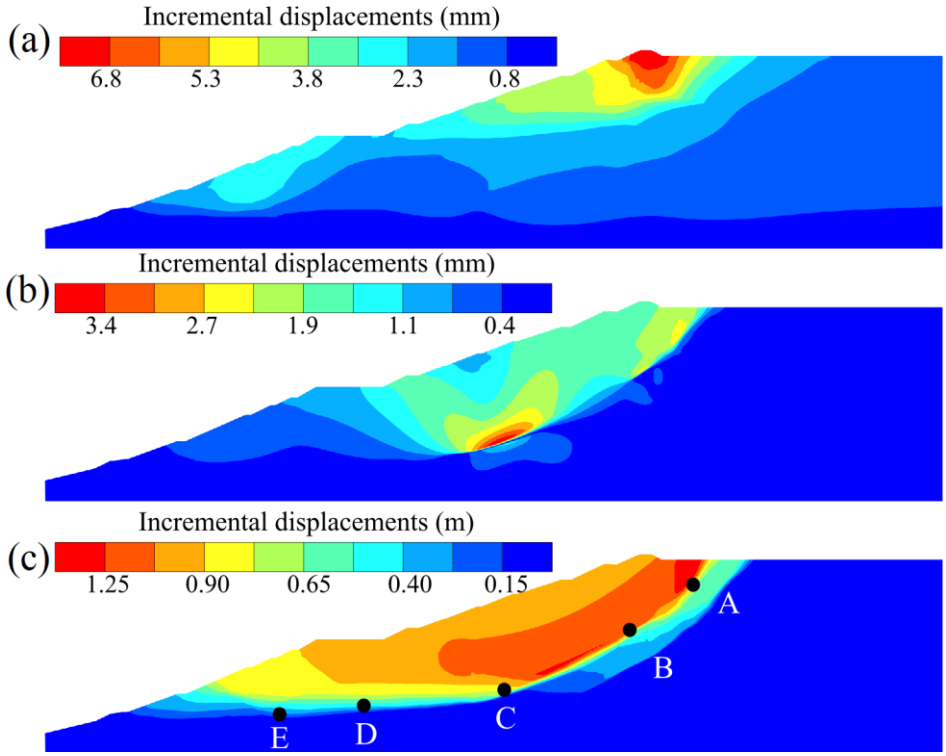

Figure 6.7 - Evolution of liquefaction failure triggered by gravity increase across different calculation steps, results using CASM: incremental displacements. (a) onset of failure, (b) intermediate stage, and (c) end of simulation.

The results obtained from NorSand (Figure 6.8 and Figure 6.9) resemble those from CASM. Similarly, two mechanisms initiate, both at the lower and upper regions of the dam (Figure 6.8a and Figure 6.9a). A complete surface develops at the first dam risings, while the upper mechanism penetrates more profoundly through the fine tailings (Figure 6.8b and Figure 6.9b). This result underscores the critical role of fine materials in global failure initiation. Notably, the developed failure surfaces (Figure 6.8c and Figure 6.9c) align with observations made by Whittle et al. (2022) through the limit analysis, indicating that increased gravity can effectively indicate the dam's most critical regions. The additional gravity increase supported by the model was 10%, 1.4 times higher than that obtained with CASM. Furthermore, the final mechanism mirrors those observed in previously tested triggers.

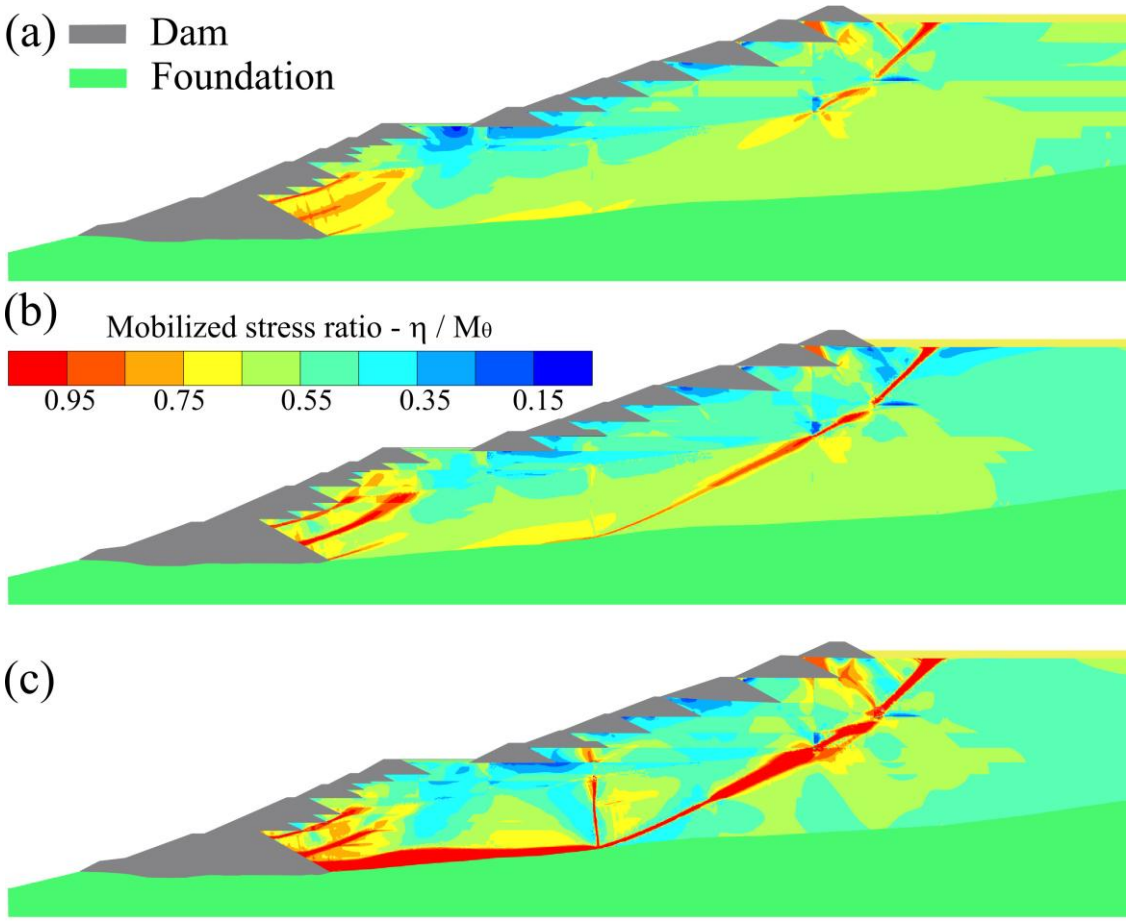

Figure 6.8 - Evolution of liquefaction failure triggered by gravity increase across different calculation steps, results using NorSand: mobilized stress ratio. (a) onset of failure, (b) intermediate stage, and (c) end of simulation.

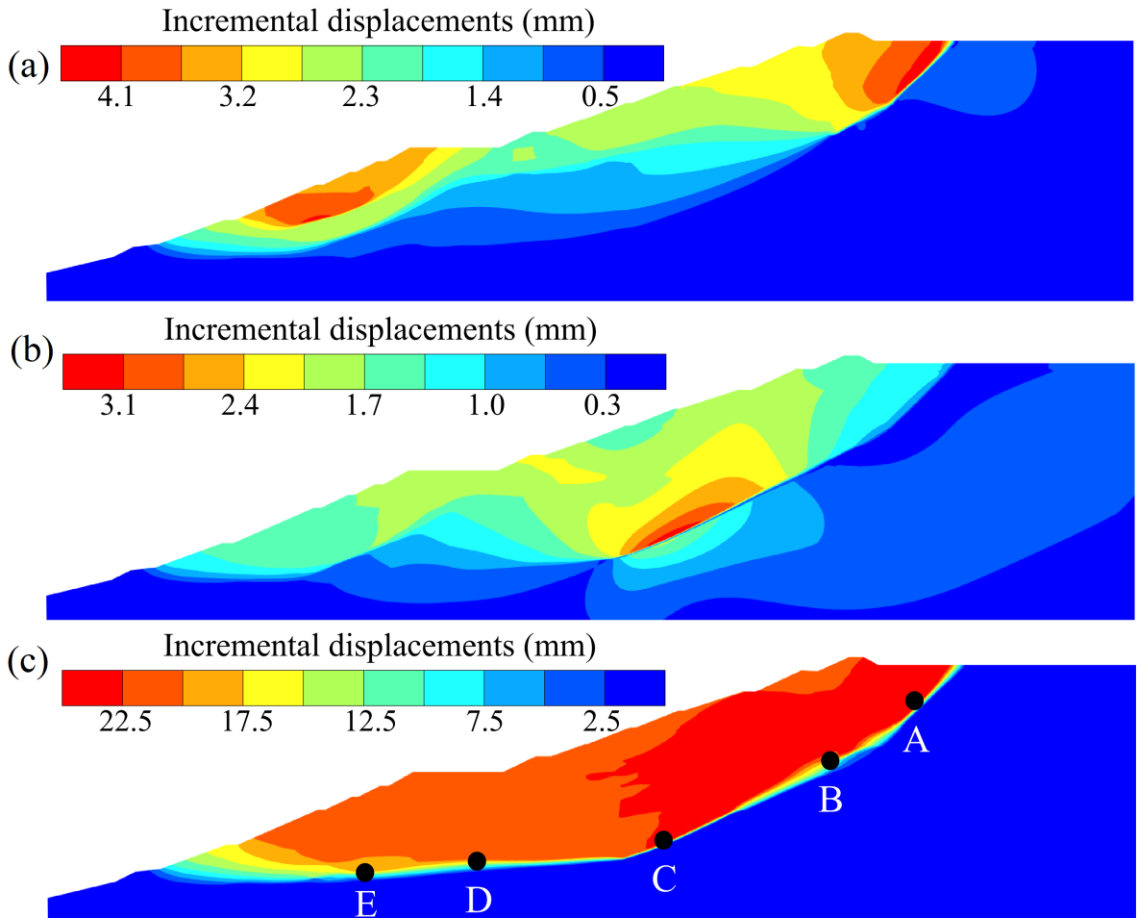

Figure 6.9 - Evolution of liquefaction failure triggered by gravity increase across different calculation steps, results using NorSand: incremental displacements. (a) onset of failure, (b) intermediate stage, and (c) end of simulation.

Stress paths at control points (Figure 6.7c and Figure 6.9c) are depicted in Figure 6.10. The behavior pattern closely resembles previous simulations. Fine tailings exhibit similar liquefaction behavior in both models. However, mixed and coarse tailings show only contraction in CASM and transition from initial contraction to dilation in NorSand. Once again, despite the differences in stress paths, the mechanisms develop similarly in both the CASM and NorSand models.

The critical increases in gravity that trigger liquefaction can be utilized to estimate a safety factor based on gravity, Equation 6-3 (Li et al., 2009; Hu et al., 2019). Gravity increases of 7% and 10% directly yield safety factors of 1.07 and 1.10, respectively, for the CASM and NorSand models. These findings are consistent with those obtained from dam loading (Section 6.1) and values obtained through the limit analysis presented by Whittle et al. (2022).

$$FS_{Gravity} = \frac{Critical\ Gravity}{Earth\ Gravity}$$ Equation 6-3

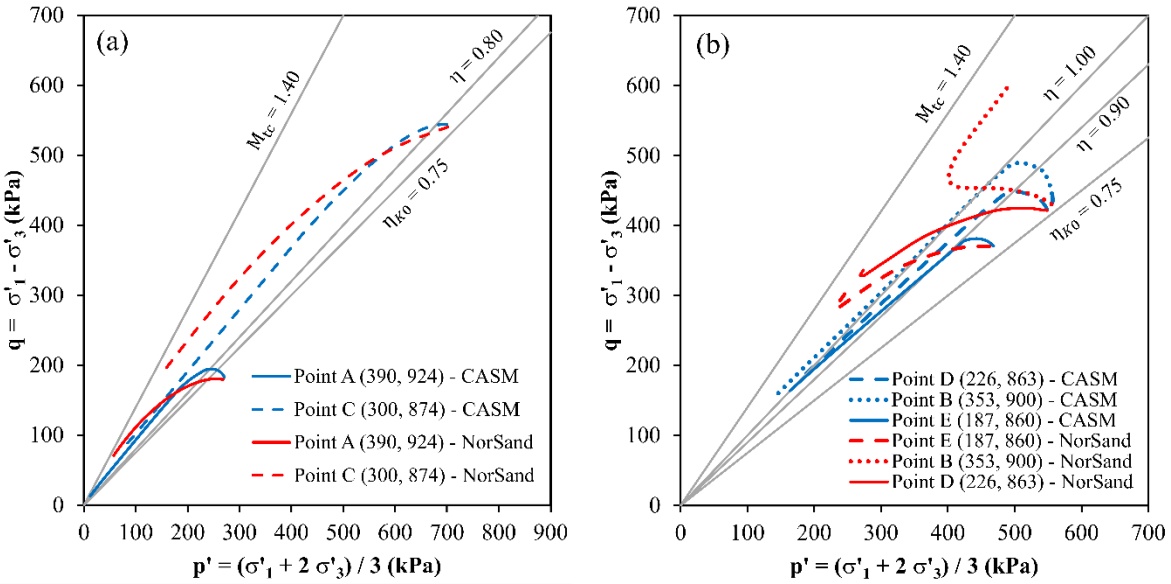

Figure 6.10 - Local soil response to liquefaction failure triggered by gravity increase: (a) fine tailings (points A, C, and D), (b) coarse tailings (point B), and mixed tailings (points E and F). Representative points are located on the failure surface (see Figure 6.7c and Figure 6.9c). The coordinates of the points, in meters, are indicated in the plot legends.

7 - DECHARACTERIZATION NUMERICAL SIMULATION

The tailings dam failure outlined in previous sections (Sections 5 and 6) has confirmed the model's ability to reproduce various aspects consistent with the recorded failure images accurately. According to Oreskes et al. (1994), once numerical models are verified, they become powerful tools for parametric analyses. Such analyses help address conditional scenarios and identify the most critical factors influencing the investigated phenomenon.

In this context, the model was used to explore the following key question: "would it be possible to implement a decharacterization strategy without triggering the static liquefaction failure?"

Different decharacterization methods were tested to address this issue, including buttress, excavation, and a hybrid buttress-excavation solution. To evaluate the influence of the construction sequence, the buttress strategy was subdivided into two arrangements: one considering the initial execution of stabilizing fill followed by backfill, and the other considering the simultaneous construction of both elements.

7.1 - MODEL SETUP

The numerical model developed for the back analysis of the failure was used as the starting point for the decharacterization simulations. The model was extended in the downstream area to allow for the simulation of buttress solutions. These changes are illustrated in Figure 7.1.

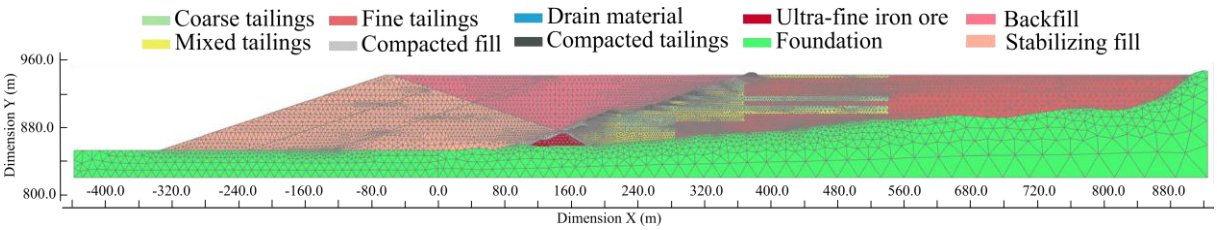

Figure 7.1 - Numerical model applied for decharacterization simulations.

The simulated buttress involves constructing an approximately 88 m high stabilizing fill, starting downstream of the starter dam, followed by a backfill between the new embankment and the upstream-raised dam. The simulation was carried out using the elastoplastic Mohr-Coulomb model, with the mechanical parameters presented in Table 7.1

defined based on the values indicated in Section 5.1 for the fine tailings and compacted fill. The hydraulic parameters applied to the stabilizing fill and backfill were the same as those used for the compacted fill and fine tailings, as outlined in Table 5.4. Slopes with an inclination of 33% were employed, resulting in a safety factor of approximately 2.15, as estimated by Equation 7-1.

Table 7.1 – Parameters adopted for the buttress.

Parameters	Stabilizing fill	Backfill
c' (kPa)	0.0	0.0
ϕ' (°)	35.0	35.0
E (MPa)	30.0	15
ν	0.33	0.33
Unit weight (kN/m³)	19.0	22.0

$$FS = \frac{\tan \varphi'}{\tan \alpha} = \frac{\tan 35}{\tan 18} = 2.15 \qquad \text{Equation 7-1}$$

where α is the slope angle.

The finite element mesh consists of approximately 29,000 15-node triangular elements (Figure 7.1). The mechanical and hydraulic boundary conditions were maintained as described in Section 5.1.4: horizontal displacement constraints on the sides of the model; both horizontal and vertical displacement constraints on the bottom boundary; a constant total water load at an elevation of 941.0 m on the right boundary; and a constant total water load at an elevation of 848.0 m on the left boundary. A drainage system at the base of the buttress was assumed to prevent the groundwater table from rising within the embankment.

Initially, the analyses were conducted considering the undrained condition for the saturated tailings. In these analyses, volumetric deformation is restricted, and excess pore pressure dissipation is not considered. This condition represents an immediate intervention, reflecting an extreme scenario in terms of the development of the static liquefaction mechanism.

Additionally, transient analyses with hydromechanical coupling were also conducted. These analyses allow for considering time and pore pressure dissipation, making it a more representative condition.

Further details about the geometry and sequencing of the simulations will be presented individually for each intervention in the following sections. It is important to note that the modifications to the geometry and mesh used for simulating the decharacterization stages did not affect the results discussed in Section 5. Thus, it was possible to reproduce the same pre-failure conditions and the failure caused by the borehole in the model adjusted for the decharacterization analyses.

For the decharacterization simulation, we did not conduct a vulnerability analysis; however, this methodology is recommended for design purposes, both for the final configuration and for the intermediate stages. During the decharacterization works, it is important to consider the impact of vibrations induced by heavy equipment traffic. However, this study is limited to the analysis of static liquefaction; thus, dynamic effects are beyond its scope.

7.1.1- BUTTRESS STRATEGY 1

The scenario referred to as Buttress Strategy 1 represents the condition where the stabilizing fill and backfill would be executed in separate stages, i.e., a non-simultaneous condition. The embankments were subdivided into layers with thicknesses corresponding to the dam raises. In this scenario, the construction of the stabilizing fill was first simulated in 13 stages, followed by the backfill in an additional 11 stages, totaling 24 stages. Figure 7.2 presents some of the stages of the simulation.

7.1.2- BUTTRESS STRATEGY 2

The scenario involving the simultaneous construction of the stabilizing fill and backfill is referred to as Buttress Strategy 2. In this scenario, 13 simulation stages were applied, some of which are shown in Figure 7.3. It is noted that the layer thicknesses and the final condition are the same as those presented in the previous strategy (Section 7.1.1), with only the construction sequence being altered.

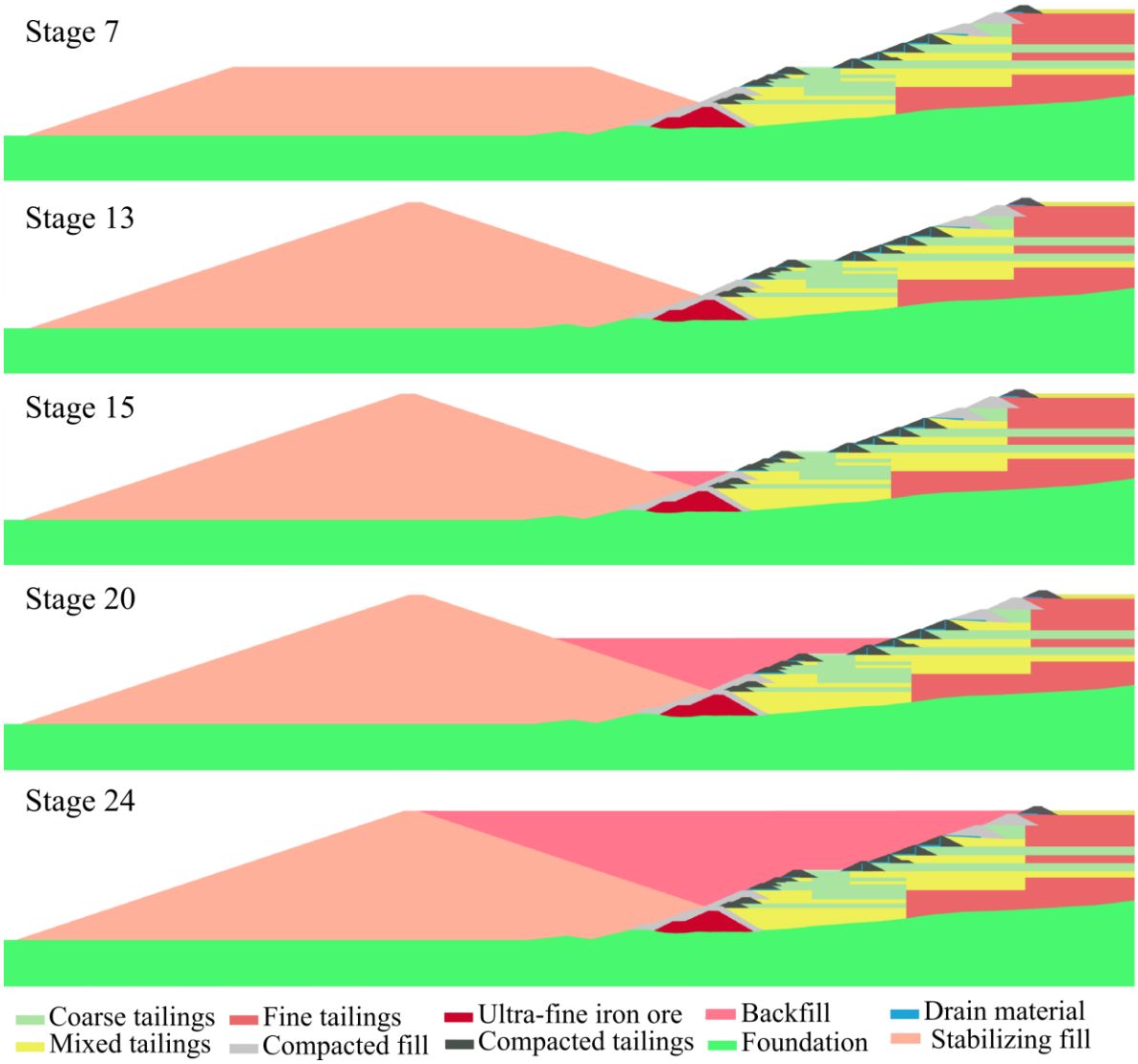

Figure 7.2 - Simulation stages for buttress strategy 1.

7.1.3- EXCAVATION

The excavation of the reservoir and raises were simulated with a downstream-to-upstream slope of approximately 3.5%, subdivided into steps with slopes ranging from 4 to 6 m in height. The simulation was discretized into 13 stages, each dedicated to excavating at least one raise. Some of the simulation stages are presented in Figure 7.4.

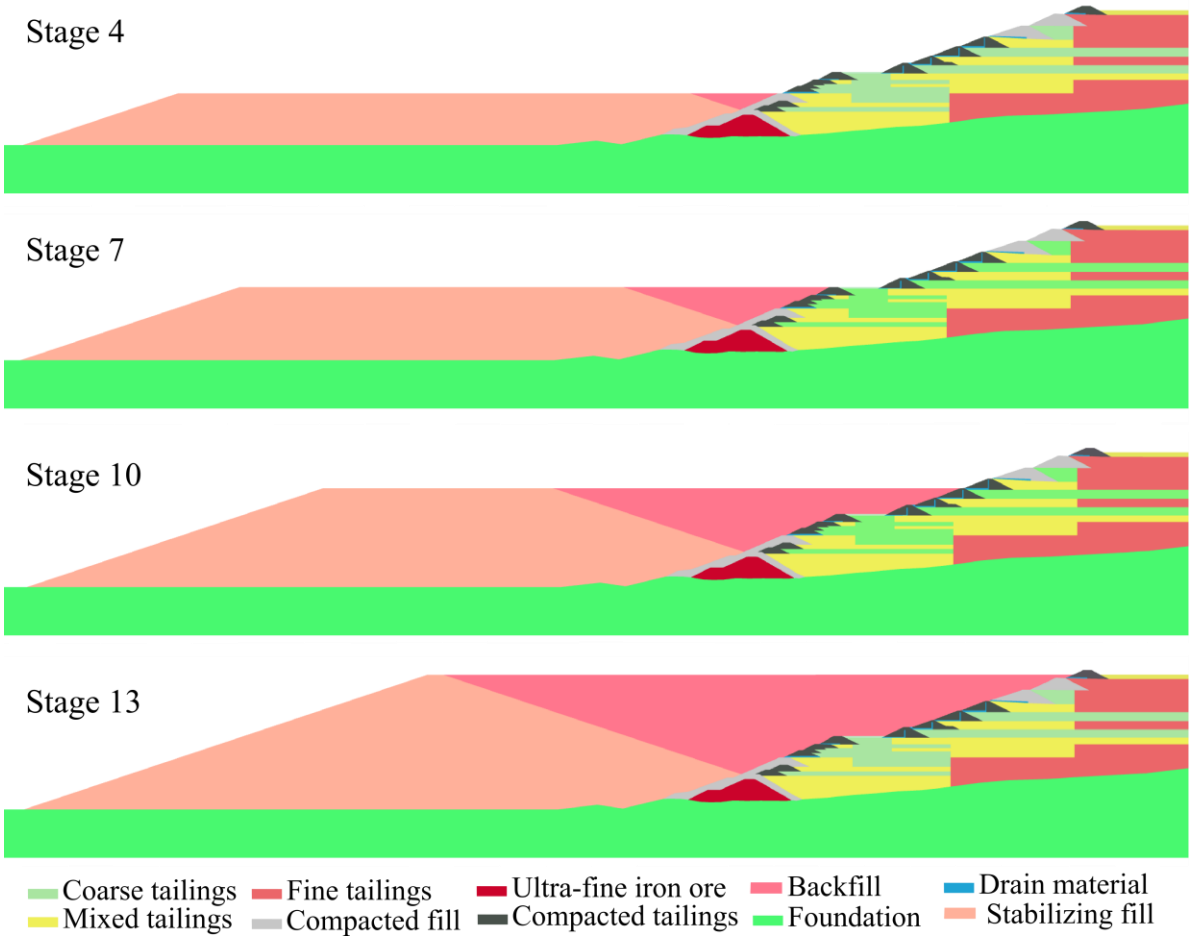

Figure 7.3 - Simulation stages for buttress strategy 2.

7.1.4- HYBRID BUTTRESS-EXCAVATION

In the hybrid solution combining buttress construction with the excavation of raises and the reservoir, the same stage configurations presented in the previous sections (Sections 7.1.2 and 7.1.3) were applied, with only the order of interventions changed. Initially, the construction of the buttress was simulated following the same stages outlined in Section 7.1.2. Subsequently, the raises and reservoir excavation proceeded up to the buttress elevation using the same excavation stages described in Section 7.1.3. These simulations aimed to determine the minimum height of the buttress required to carry out the excavation process without triggering static liquefaction, even considering the undrained condition for the saturated tailings. Figure 7.5 presents an example scenario with the buttress up to approximately 910.0 m.

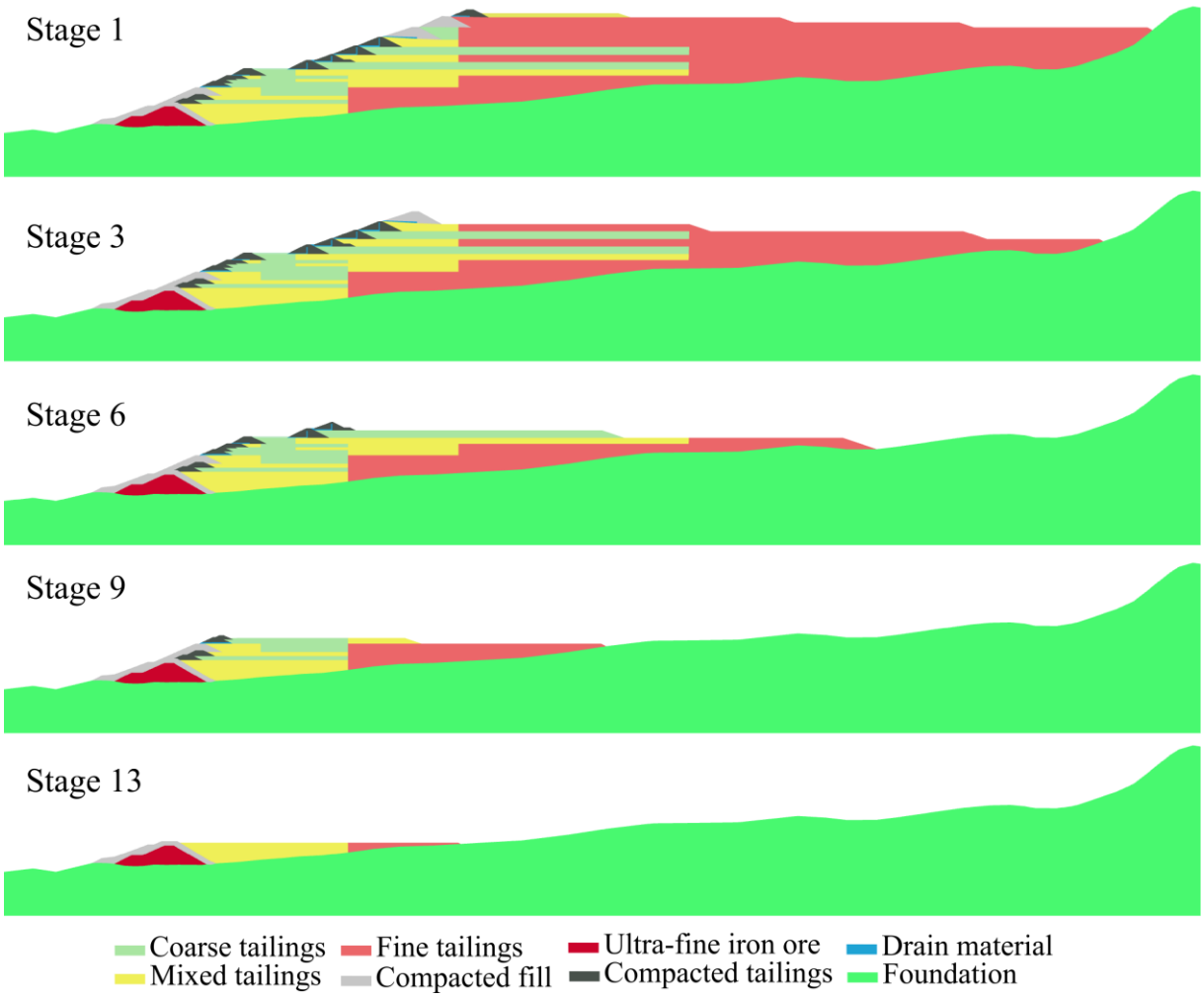

Figure 7.4 - Simulation stages for excavation of the reservoir and raises.

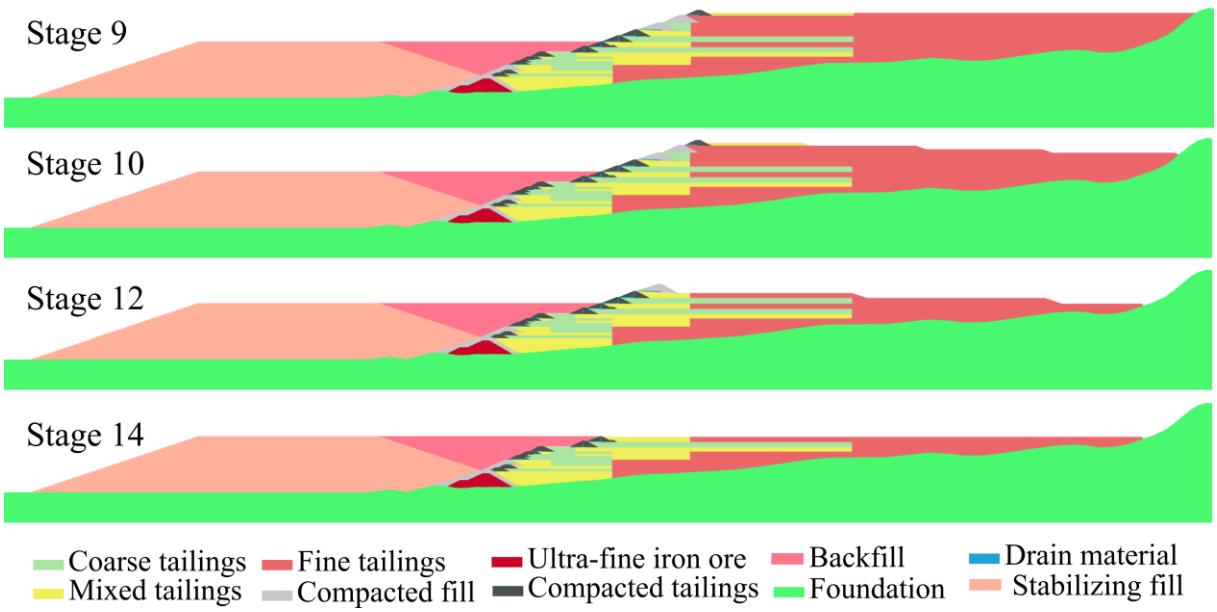

Figure 7.5 - Simulation stages for hybrid buttress-excavation strategy.

7.2 - RESULTS AND DISCUSSIONS

The following sections provide a detailed presentation and analysis of the simulation results corresponding to the decharacterization strategies that were previously introduced and described.

7.2.1- BUTTRESS STRATEGY 1

The simulation results considering an undrained behavior of the saturated tailings are presented in terms of the mobilized stress ratio in Figure 7.6. As the buttress is constructed, the tailings near the toe become mobilized due to the earth pressure exerted by the embankment on the starter dam. The mobilization increases until, at Stage 10, a portion of the tailings reaches the critical state ($\eta/M_\theta = 1$). From this point, the mechanism propagates slowly until the final stage of stabilizing fill construction (stage 13). However, the failure mechanism is fully triggered upon initiating the first back filling stage (Stage 14), and the model no longer achieves equilibrium.

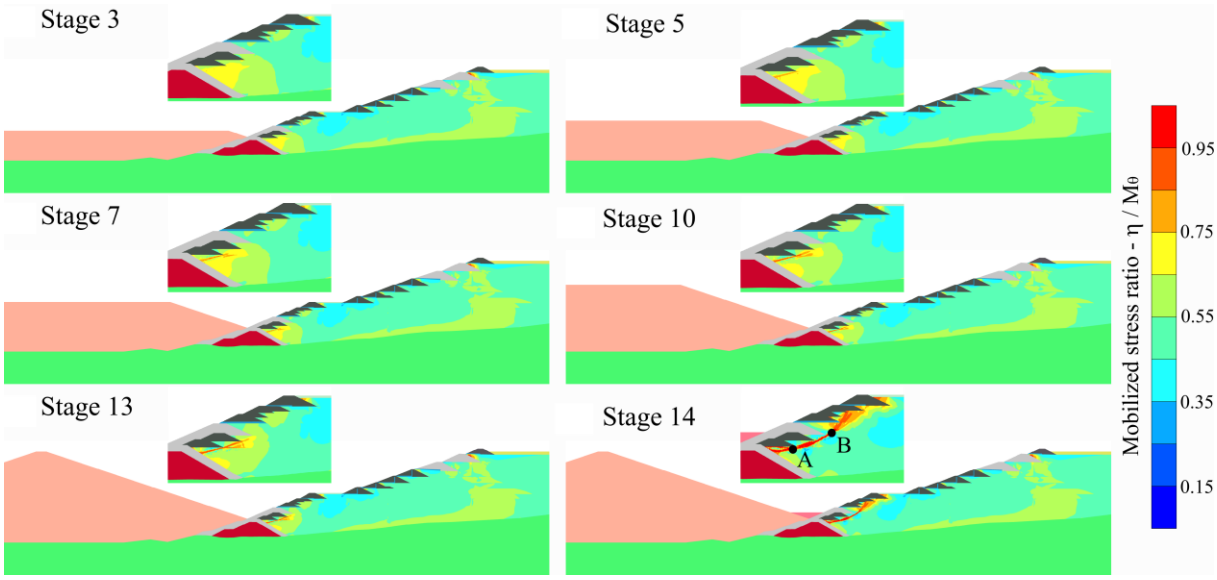

Figure 7.6 - Mobilized stress ratio resulting from buttress strategy 1 under undrained condition.

The failure occurs in the initial raises to the setback berm at an elevation of 899 m. The mechanism initiates in the lower part of the wedge, near the starter dam, and propagates toward the dam setback. Figure 7.7 presents the evolution of shear strain when static liquefaction was triggered, while Figure 7.8 shows the resulting displacements. It should be noted that the triggering of static liquefaction due to buttress construction is consistent with the actual failure of the Cadia dam (Jefferies et al., 2019).

It is important to highlight that the previously presented scenario corresponds to an undrained condition. This extreme case is likely far from reality, given that constructing the buttress structures would take considerable time. This underscores the importance of conducting transient analyses with hydromechanical coupling.

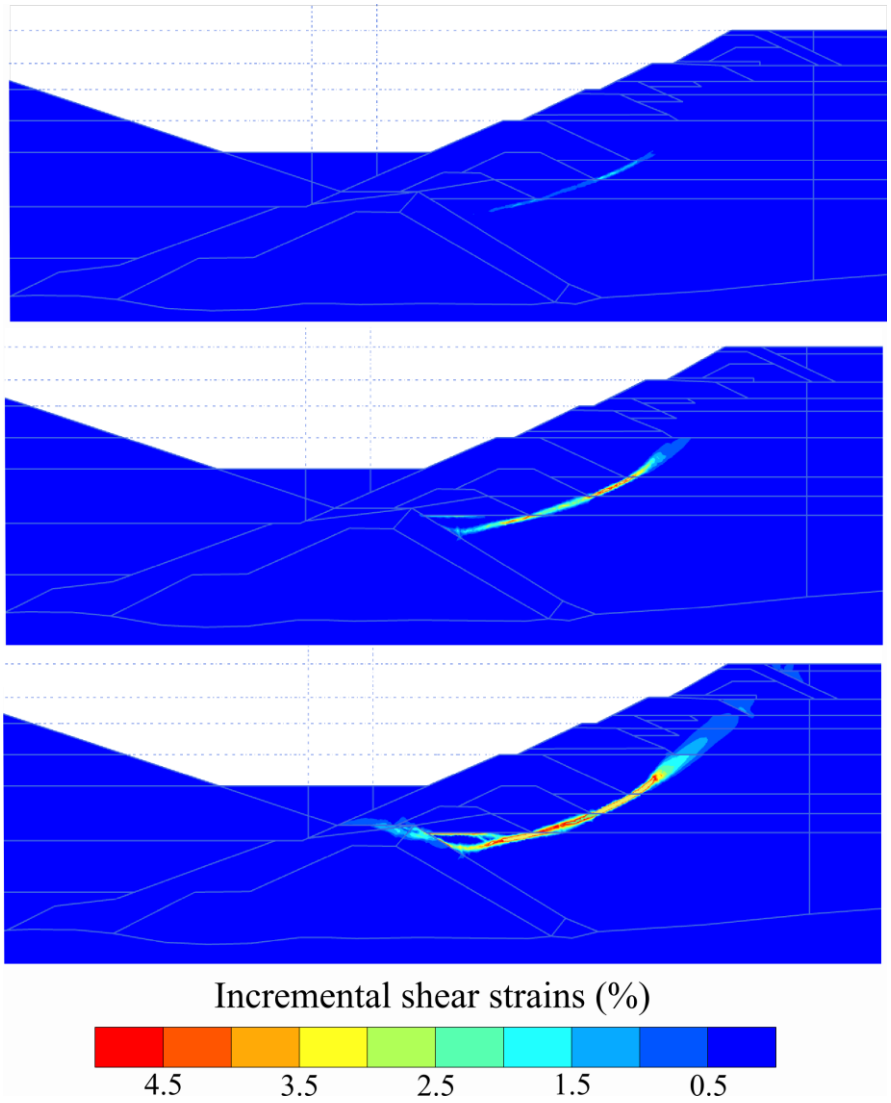

Figure 7.7 - Incremental shear strains resulting from Buttress strategy 1 under undrained condition at stage 14.

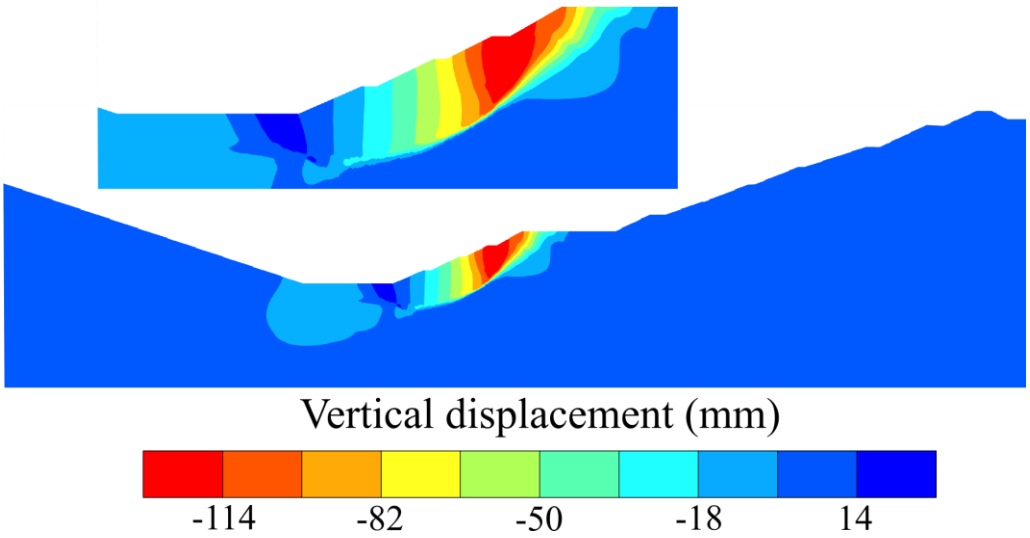

Figure 7.8 - Vertical displacement resulting from Buttress strategy 1 under undrained condition at Stage 14. Of note, negative values mean settlement.

For the transient analyses, one month per stage was considered, corresponding to an average buttress construction rate of approximately 7 m/month and a total duration of 24 months. It is important to emphasize that assuming a constant time per stage is a simplification and is not intended to represent a construction schedule accurately. However, it should be noted that the adopted rate is significantly higher than those observed in buttress-based decharacterization projects. For structures around 100 m high, recorded rates suggest that these processes take approximately 10 years, primarily due to the need for remotely operated equipment, given the risk of failure (Vale, 2025; Vale, 2024a; Vale, 2024c).

The simulation results for the hydromechanical coupled condition, in terms of the mobilized stress ratio, are presented in Figure 7.9. Unlike the undrained condition, the tailings near the toe are not significantly mobilized during the stabilizing fill construction stages (stages 1 to 13). Similarly, the static liquefaction mechanism is not triggered during the back filling stages (stages 14 to 24). As the back filling process is completed, the tailings at the dam toe become confined, reducing the mobilized stress ratio. No failure mechanism develops, and the structure remains stable, allowing for the completion of the decharacterization process (Stage 24). These results highlight the importance of accounting for time-dependent effects in analyzing interventions in critically stressed structures.

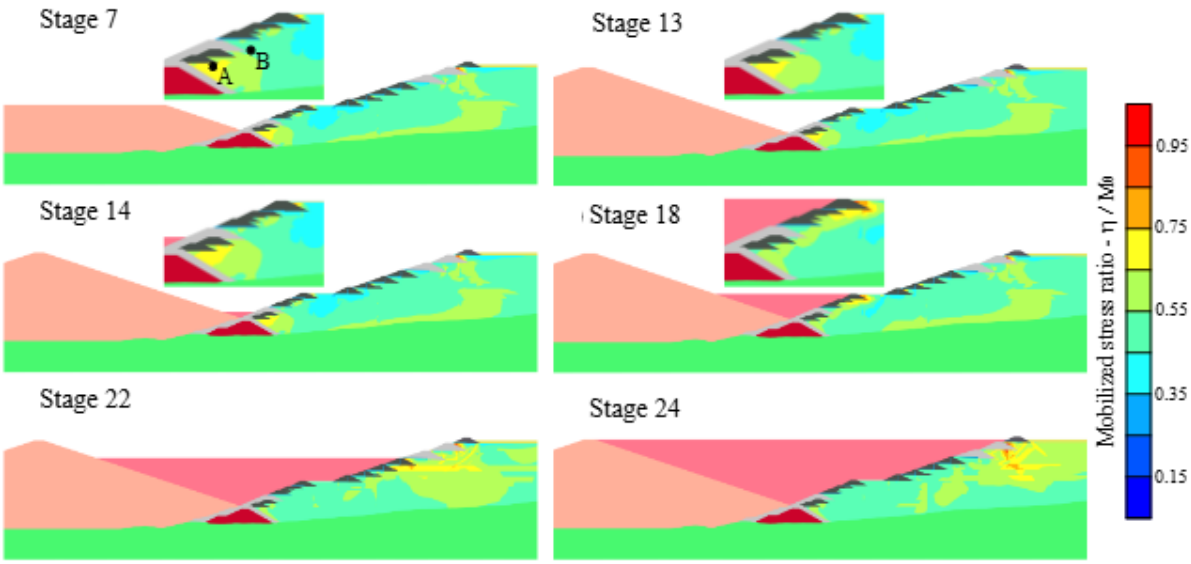

Figure 7.9 - Mobilized stress ratio resulting from Buttress strategy 1 under hydromechanical coupled condition.

Stress paths were recorded at control points, as shown in Figure 7.6 and Figure 7.9. The results are presented in Figure 7.10a for the undrained condition and in Figure 7.10b and Figure 7.10c for the hydromechanical coupled condition.

Point A, located near the starter dam, exhibits a higher initial mobilization state (η = 0.85) than Point B (η = 0.65), which is positioned within the raised embankments. In the undrained scenario (Figure 7.10a), both points are influenced by the stabilizing fill construction due to their proximity to the dam toe. Given its highly mobilized initial stress state, Point A undergoes softening from the early stages of construction. In contrast, Point B experiences a gradual increase in shear stress until Stage 14, when failure is triggered, causing the curve to shift left and reach a maximum, at which point static liquefaction occurs. Notably, even in the later stages of embankment construction (from Stage 6 onward), both points continue to experience mobilization. This behavior is linked to the spreading tendency of the stabilizing fill, which increases the lateral earth pressure on the dam toe. Consequently, the induced stresses are not limited to the initial construction stages.

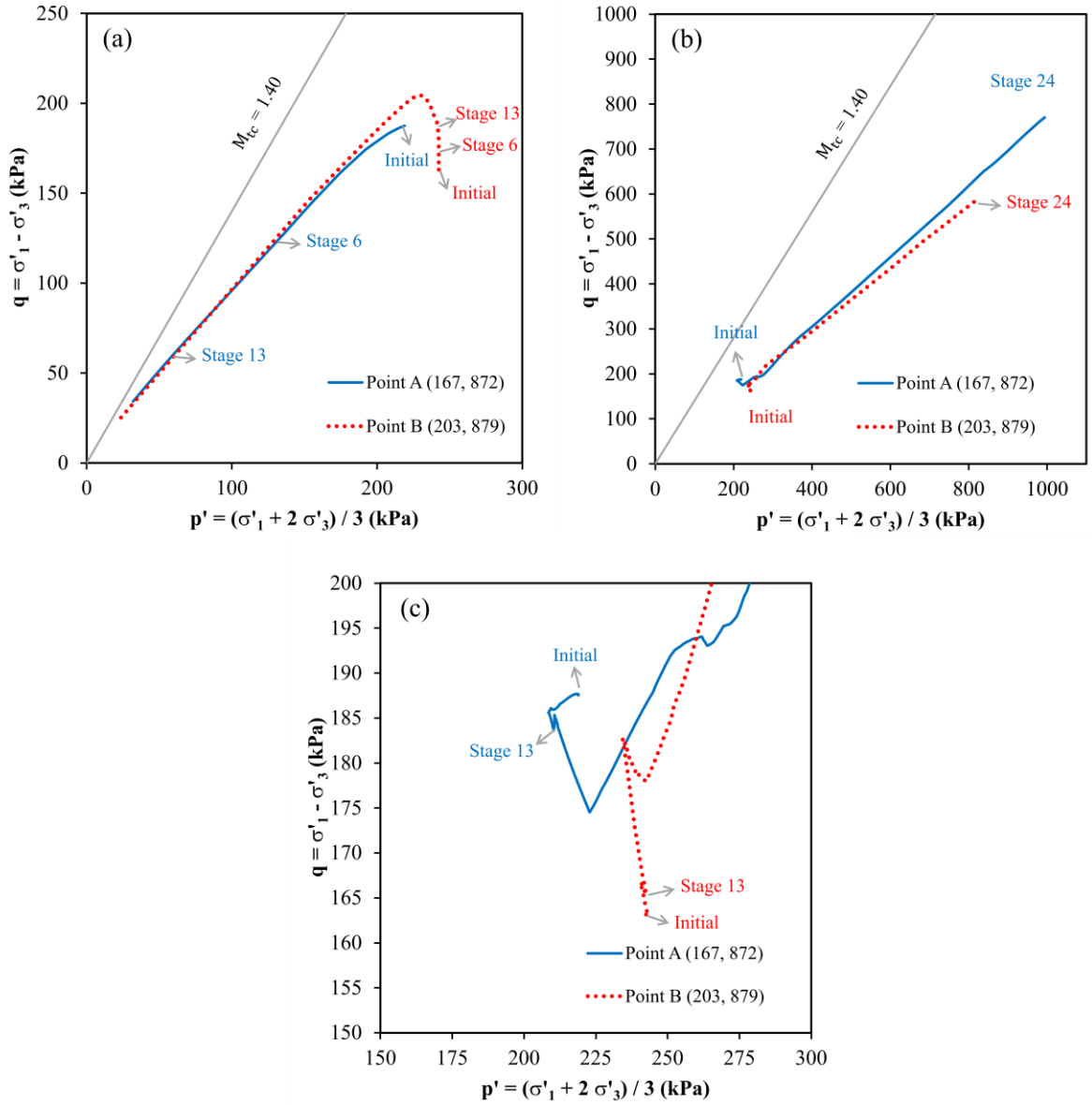

Figure 7.10 - Local soil response for decharacterization by buttress strategy 1: (a) undrained, (b) and (c) hydromechanical coupled. Representative points are located on the failure surface (see Figure 7.6 and Figure 7.9). The coordinates of the points, in meters, are indicated in the plot legends.

The coupled analysis (Figure 7.10b and c) shows slight variations in the stress state throughout the buttress construction (from the initial stage to Stage 13). This result indicates that insufficient pore pressures are generated when time effects are considered to trigger the static liquefaction process. This highlights that pore pressure generation was the main factor responsible for the significant mobilization observed in the undrained analysis. As the back filling process begins (from Stage 13 onward), the stress on the tailings increases. However, the stress paths approach the oedometric condition ($\eta = 0.75$), and no static liquefaction triggering is observed.

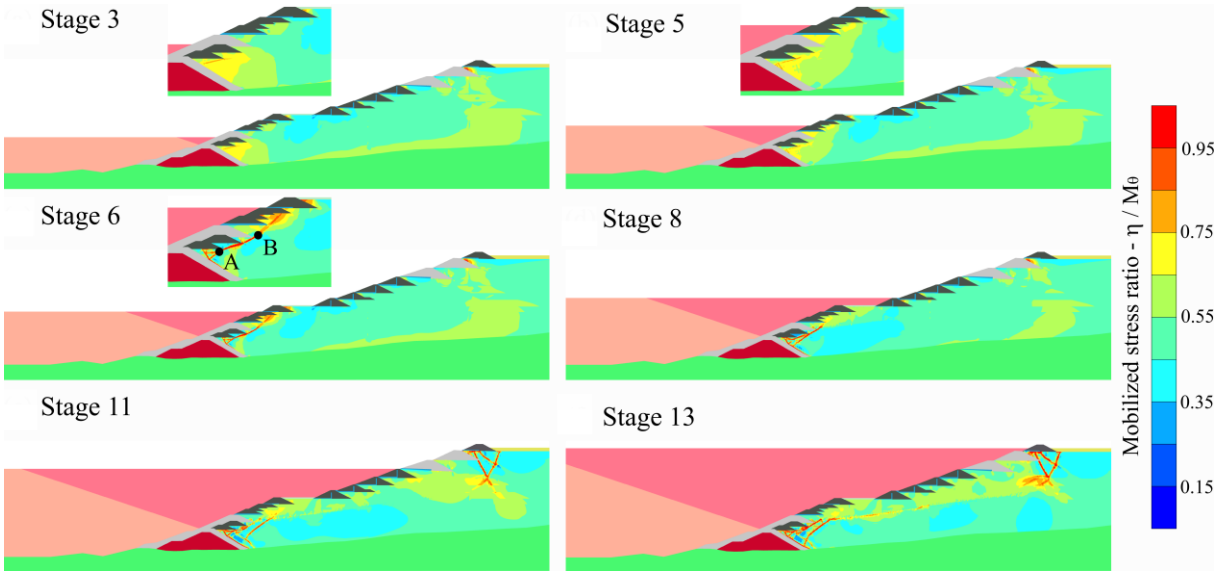

Figure 7.11 - Mobilized stress ratio resulting from Buttress strategy 2 under undrained condition.

7.2.2- BUTTRESS STRATEGY 2

The results for the undrained scenario, considering the simultaneous execution of the stabilizing buttress and back filling, are presented in Figure 7.11. The tailings near the starter dam continue to experience mobilization, similar to the non-simultaneous condition (Section 7.2.1), but the failure mechanism does not propagate (Stage 3). As the buttress construction progresses, a generalized failure surface develops; however, the counterbalancing effect of the back filling is sufficient to maintain equilibrium (stages 5 and 6), preventing the onset of a failure process (Figure 7.12). Notably, the localized mobilization in the initial embankments near the dam toe was insufficient to trigger liquefaction in other regions of the reservoir.

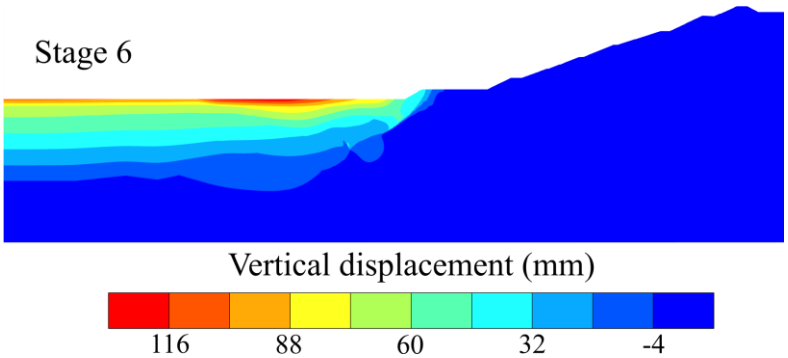

Figure 7.12 - Vertical displacement resulting from Buttress strategy 2 under undrained condition at stage 6. Of note, negative values mean settlement.

Based on these results, the simultaneous execution of the buttress and back filling is a safer strategy than the non-simultaneous condition. Liquefaction occurs in a localized region but does not propagate sufficiently to compromise the stability of the structure.

Hydromechanical coupled analyses were also performed, considering one month per stage. The results are presented in Figure 7.13 and show a similar trend to that reported for the non-simultaneous strategy (Figure 7.9). The tailings near the dam toe experience minor disturbances, and the material becomes confined as the buttress construction progresses.

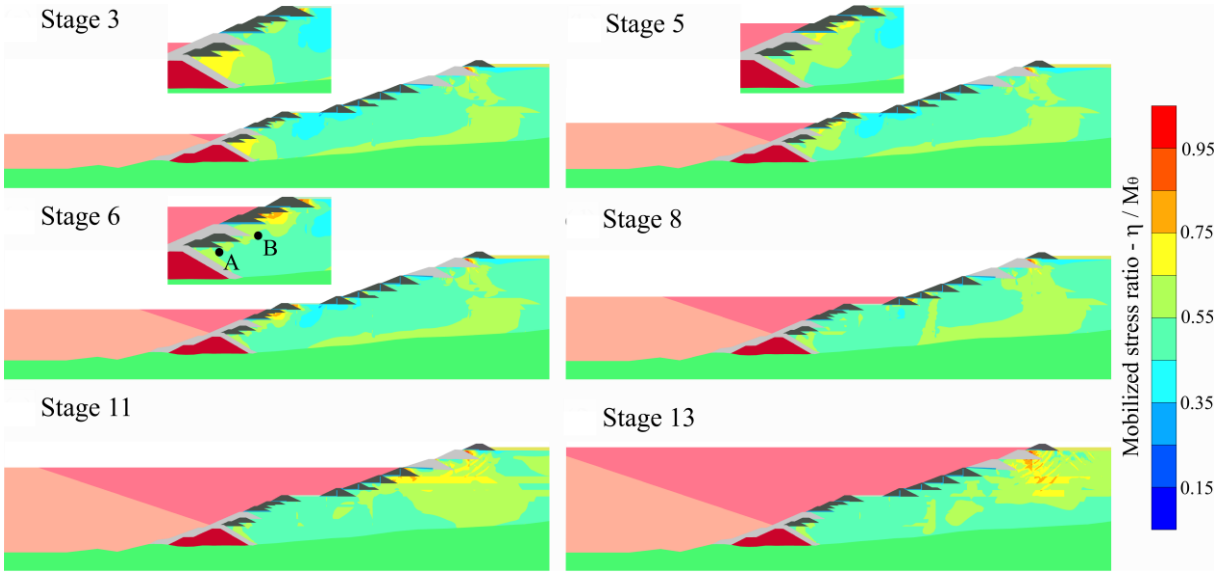

Figure 7.13 - Mobilized stress ratio resulting from buttress strategy 2 under hydromechanical coupled condition.

Stress paths were recorded at control points, as illustrated in Figure 7.11 and Figure 7.13, with the results presented in Figure 7.14. The results for buttress strategy 2 are labeled M2 (model 2), while those for buttress strategy 1 are designated M1 (model 1), allowing for a direct comparison between the scenarios.

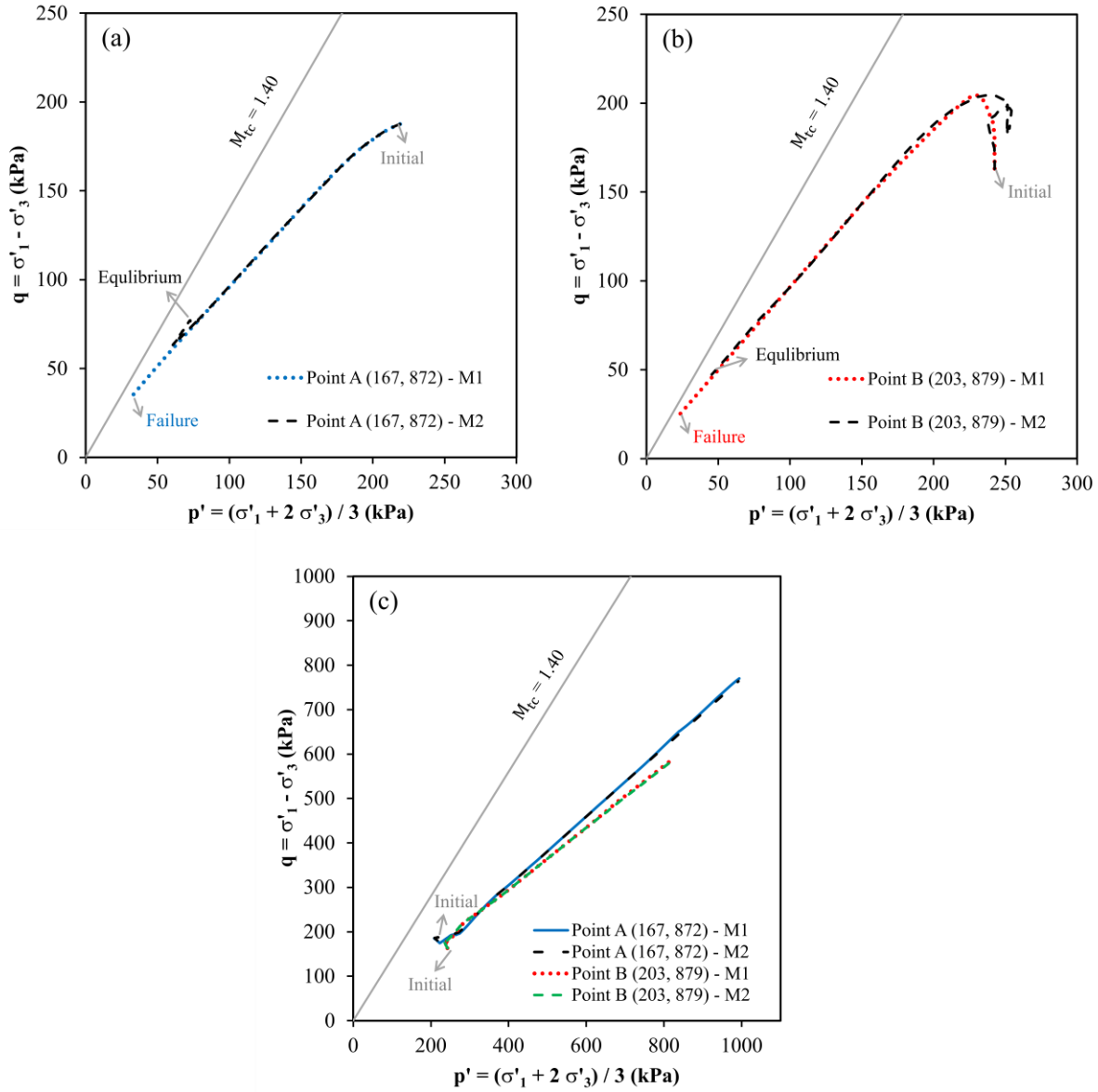

Figure 7.14 - Local soil response for decharacterization by buttress: (a) and (b) undrained, and (c) hydromechanical coupled. Of note, M1 refers to the non-simultaneous reinforcement and fill, while M2 refers to the simultaneous condition. Representative points are located on the failure surface (see Figure 7.6, Figure 7.9, Figure 7.11 and Figure 7.13). The coordinates of the points, in meters, are indicated in the plot legends.

For the undrained condition (Figure 7.14a and Figure 7.14b), the stress responses at the control points are nearly identical for both models. However, as illustrated by the failure mechanism in Figure Figure 7.11c, the key difference between the scenarios lies in the residual strength. In the simultaneous construction scenario (M2), the residual strength tends to stabilize, reaching equilibrium due to the confinement provided by the concurrently executed backfill. In contrast, in the non-simultaneous scenario (M1), the residual strength is lower, as equilibrium

is not achieved. For the hydromechanical coupled condition, no significant differences are observed between the simultaneous and non-simultaneous scenarios, as shown in Figure 7.14c.

7.2.3- EXCAVATION

The simulation results for the undrained scenario are presented in Figure 7.15 and Figure 7.16. In the first excavation stage, the development of a global failure mechanism was observed. The failure initiates at the reservoir surface and propagates through deeper tailings layers. The displacements induced by this initial mechanism trigger a second failure surface near the raised embankments at the dam toe, similar to the behavior observed in the buttress reinforcement strategy (Section 7.2.1). Ultimately, the global mechanism propagates, forming a third failure surface extending from the crest to the dam toe. At this point, the model loses convergence and fails to reach equilibrium.

The complete excavation of the reservoir is only feasible when considering a hydromechanical coupled analysis. For this analysis, one month per stage was maintained, corresponding to an excavation rate of approximately 5 m/month, resulting in a total duration of thirteen months. Once again, it is emphasized that adopting a constant time per stage is a simplification without the intent to represent an execution schedule precisely. Additionally, the applied rate is significantly higher than those observed in decharacterization projects, where recorded rates suggest an expected duration of approximately two years for structures 50 m in height, mainly due to the predominant need for remotely operated equipment given the risk of failure (Vale, 2025; Vale, 2024b). The results obtained from the coupled model are presented in Figure 7.17.

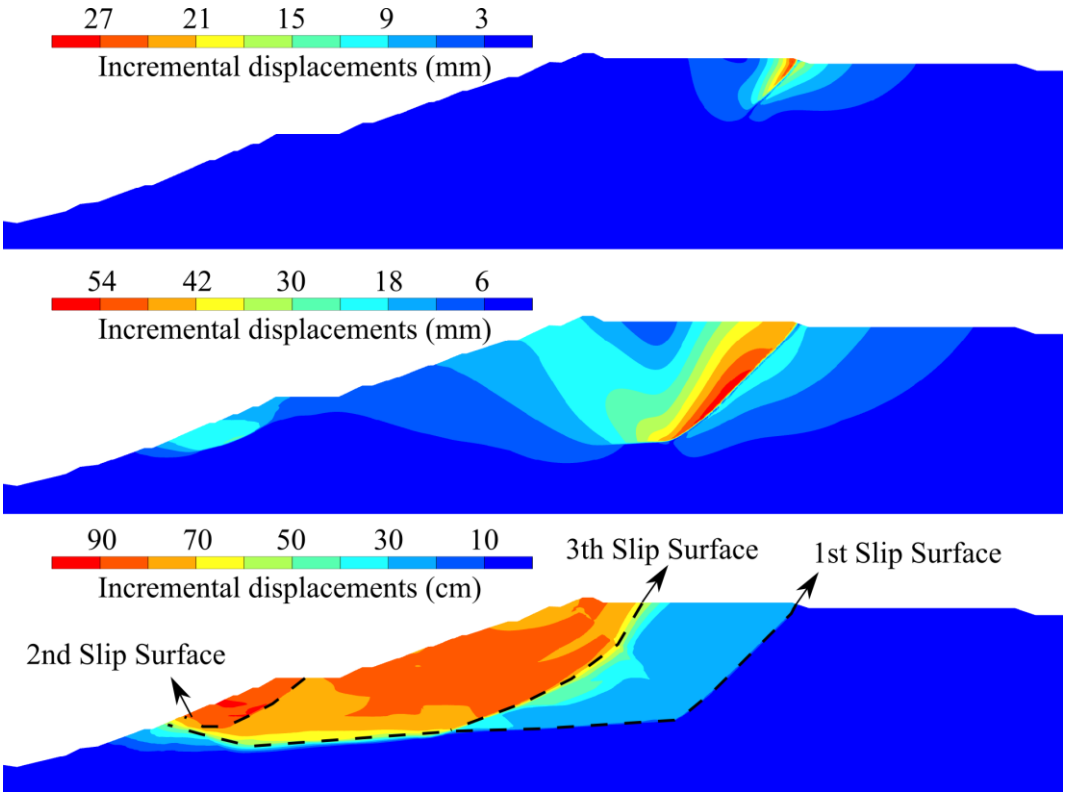

Figure 7.15 - Numerical results for excavation simulation under undrained condition: incremental displacements per step.

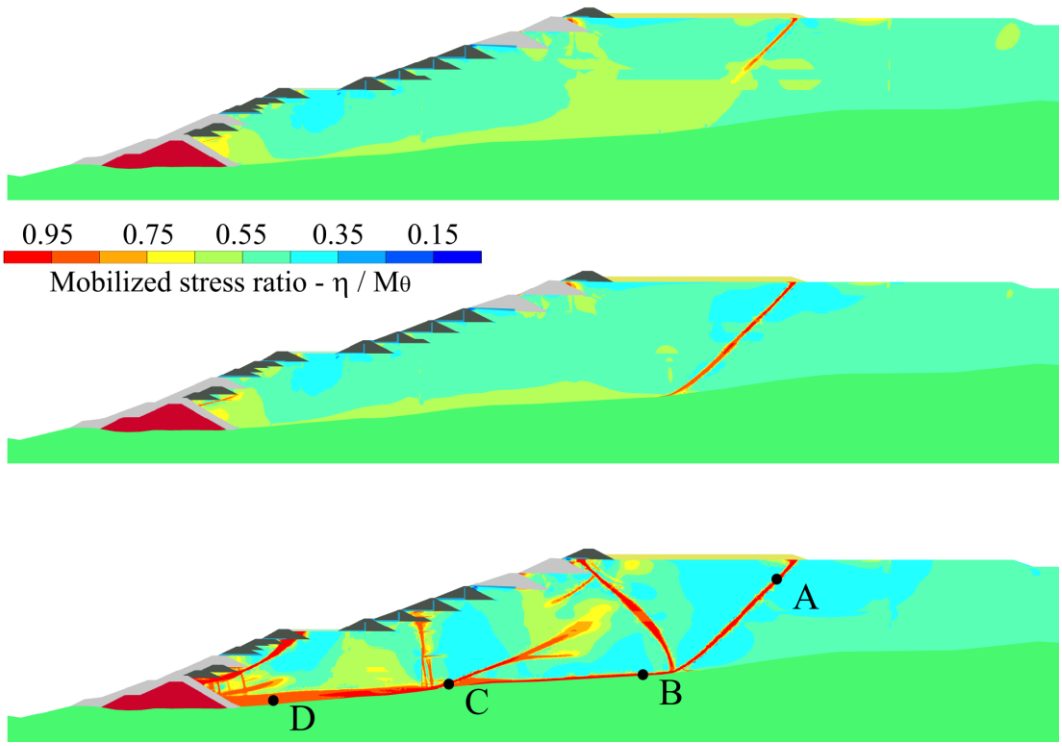

Figure 7.16 - Numerical results for excavation simulation under undrained condition: mobilized stress ratio.

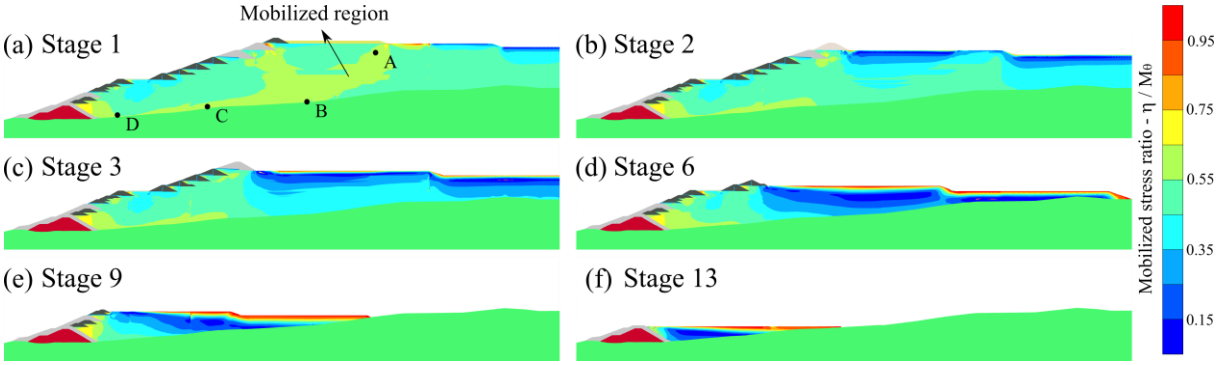

Figure 7.17 - Mobilized stress ratio resulting from excavation strategy under hydromechanical coupled condition.

In the first stage, tailings mobilization is observed in the region where failure previously occurred in undrained simulation. However, in the coupled analysis, this mechanism does not propagate. From the second stage onward, a reduction in mobilization is noted, resulting from the unloading induced by material removal. This behavior highlights that the initial excavation stages represent the most critical phase of the process. In the subsequent stages, mobilization is limited to surface materials, a phenomenon associated with low confinement. Although this may pose challenges for equipment movement, it does not develop into a dam instability mechanism. No failure mechanism was identified, and the observed vertical displacements are predominantly expansive after the initial stages, as shown in Figure 7.18.

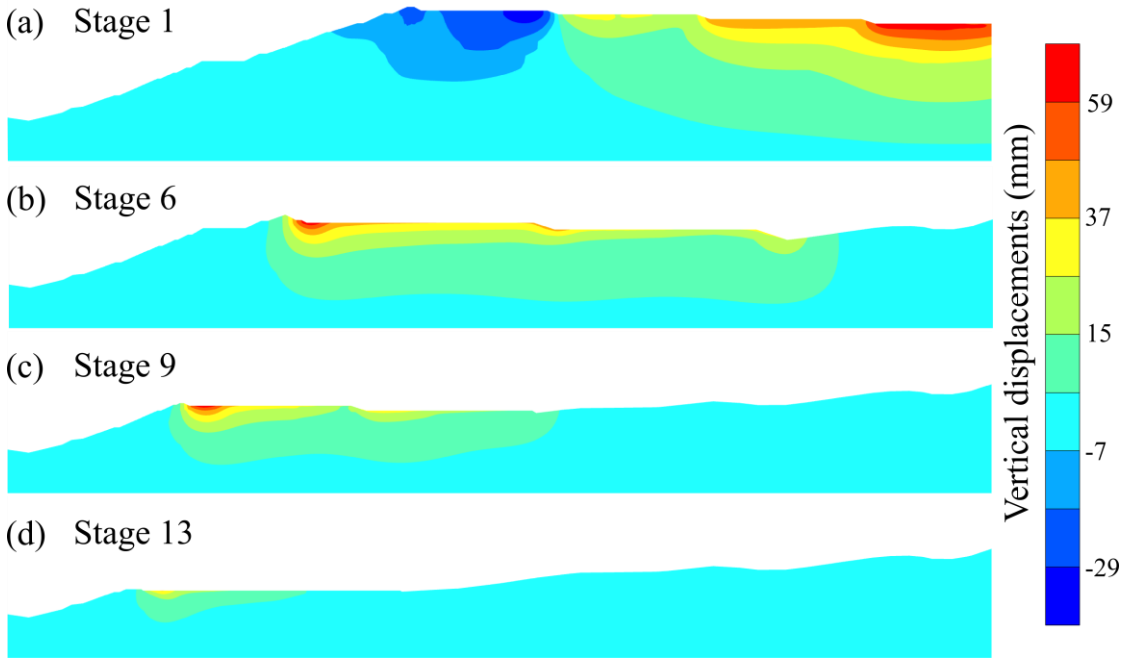

Figure 7.18 - Vertical displacement per stage induced by excavation under hydromechanical coupled condition. Of note, negative values mean settlement.

Stress paths were recorded at control points, as shown in Figure 7.16 and Figure 7.17, and their results are illustrated in Figure 7.19. The analysis of Point A's behavior (Figure 7.19a and Figure 7.19b) indicates that during the initial excavation stages, stress mobilization occurs, triggering failure in the undrained model and propagating to deeper regions (Figure 7.19c). This behavior highlights the structure's sensitivity to minor disturbances due to its low safety factor (Rógenes et al., 2024a; Whittle et al., 2022).

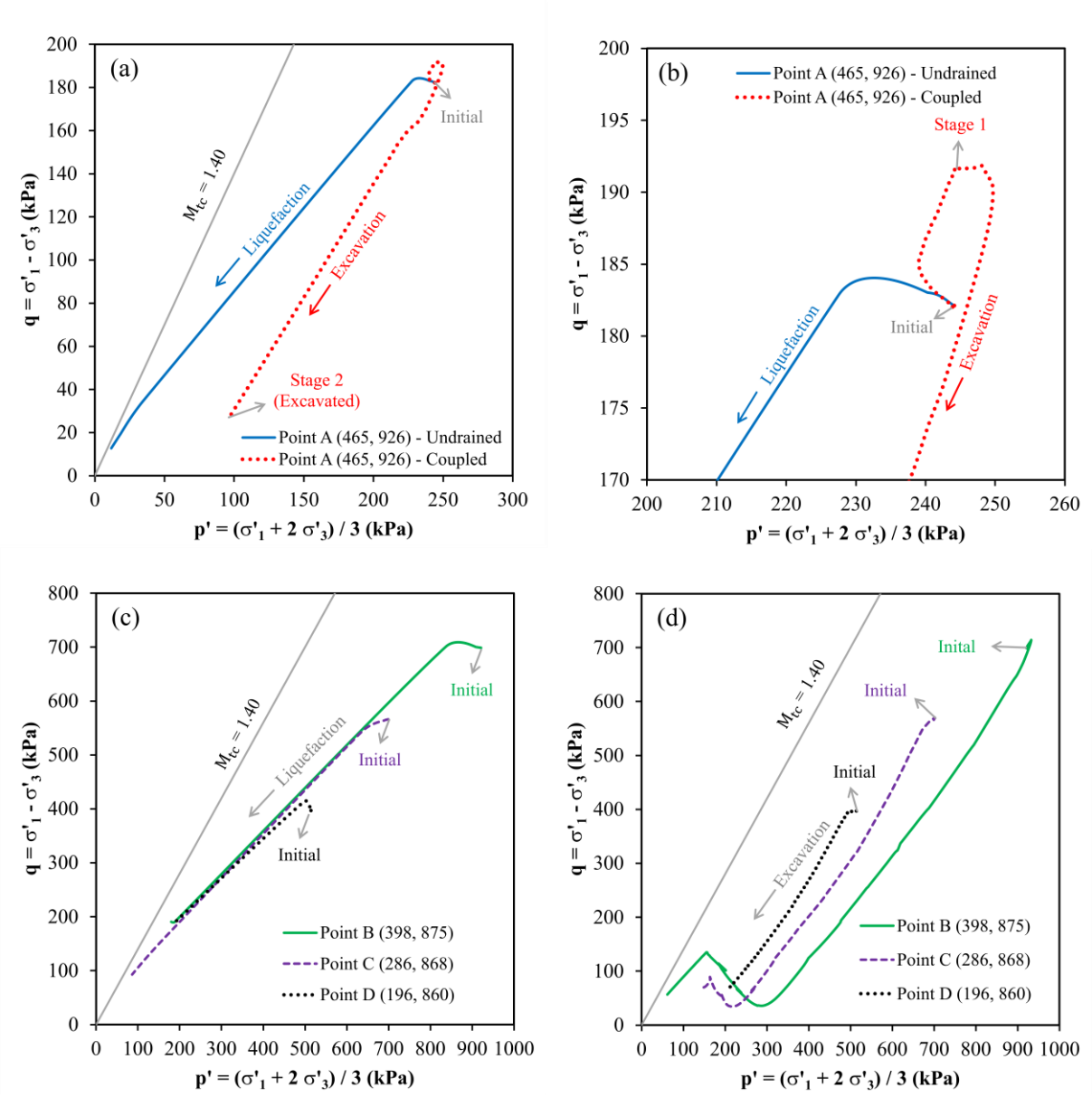

Figure 7.19 - Local soil response for decharacterization by excavation: (a) undrained and coupled at point A, (c) undrained (d) coupled. Representative points are located on the failure surface (see Figure 7.16 and Figure 7.17). The coordinates of the points, in meters, are indicated in the plot legends.

Mobilization is most intense during Stage 1, as the coupled model indicates (Figure 7.19). Beyond this stage, a gradual reduction in stress mobilization occurs, leading to a less critical condition. This finding further reinforces that the initial phases of excavation are the most vulnerable to liquefaction onset, as previously observed.

Figure 7.19d shows that as the excavation approaches the control point, an extension demand arises due to the reduction in confinement, as seen at points B and C. In contrast, Point D does not exhibit this behavior, as it remains confined. Finally, considering the time effect in the coupled analyses, excess pore pressure generation is insufficient to trigger a static liquefaction process that could lead to global failure (Figure 7.19a and Figure 7.19d).

7.2.4- HYBRID BUTTRESS-EXCAVATION

Based on the results presented in Sections 7.2.1 to 7.2.3, it is evident that under a hydro-mechanical coupled scenario, decharacterization can be achieved through either the reinforcement or excavation strategy. Therefore, only the results under undrained conditions will be discussed for the hybrid strategy. This assessment aims to determine the minimum reinforcement height required to safely proceed with excavation while maintaining stability in an undrained scenario.

The analyses of the hybrid buttress-excavation solution began with the simulation of buttress strategy 2, as this scenario did not trigger the liquefaction mechanism under undrained conditions. Consequently, the results obtained during the buttress construction are the same as those presented in Figure 7.11.

Initially, the excavation was simulated when the buttress reached an elevation of 899.0 m, corresponding to the setback region of the dam raises. The results are presented in Figure 7.20 and Figure 7.21. It is observed that liquefaction is triggered in the first excavation stage. The failure initiates at the reservoir surface, propagates through the deeper tailings, and emerges near the setback zone due to the confinement of the buttress at the dam toe. This result highlights the necessity of constructing the buttress to a height exceeding the setback elevation.

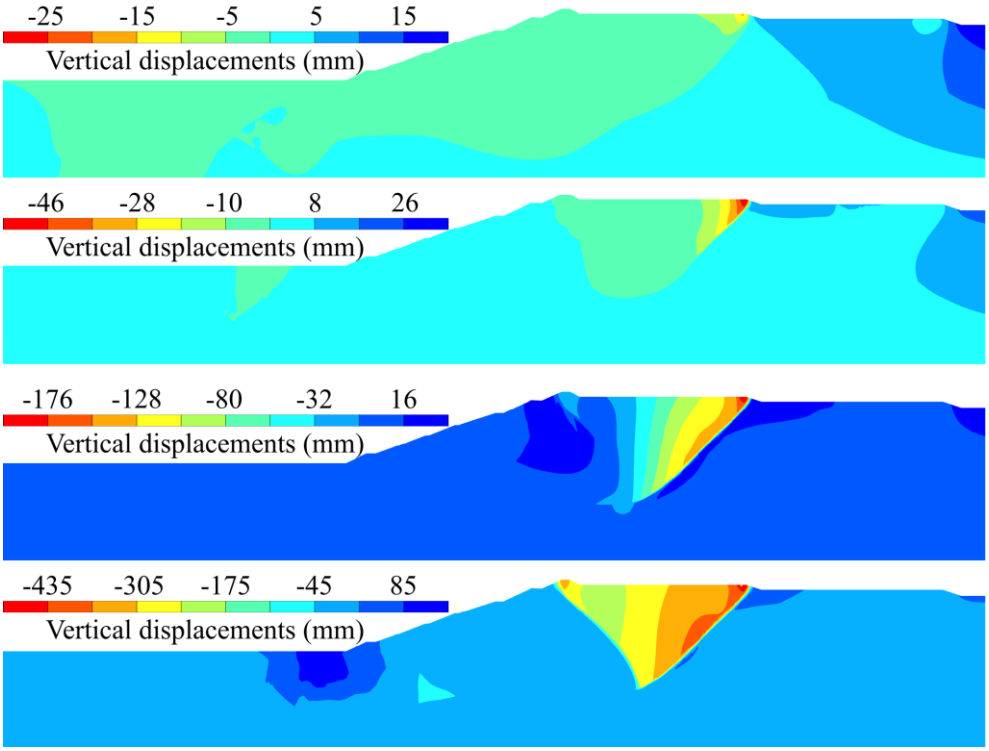

Figure 7.20 - Numerical results for buttress at elevation 899.0 m follow by excavation: incremental vertical displacements per step. Of note, negative values mean settlement.

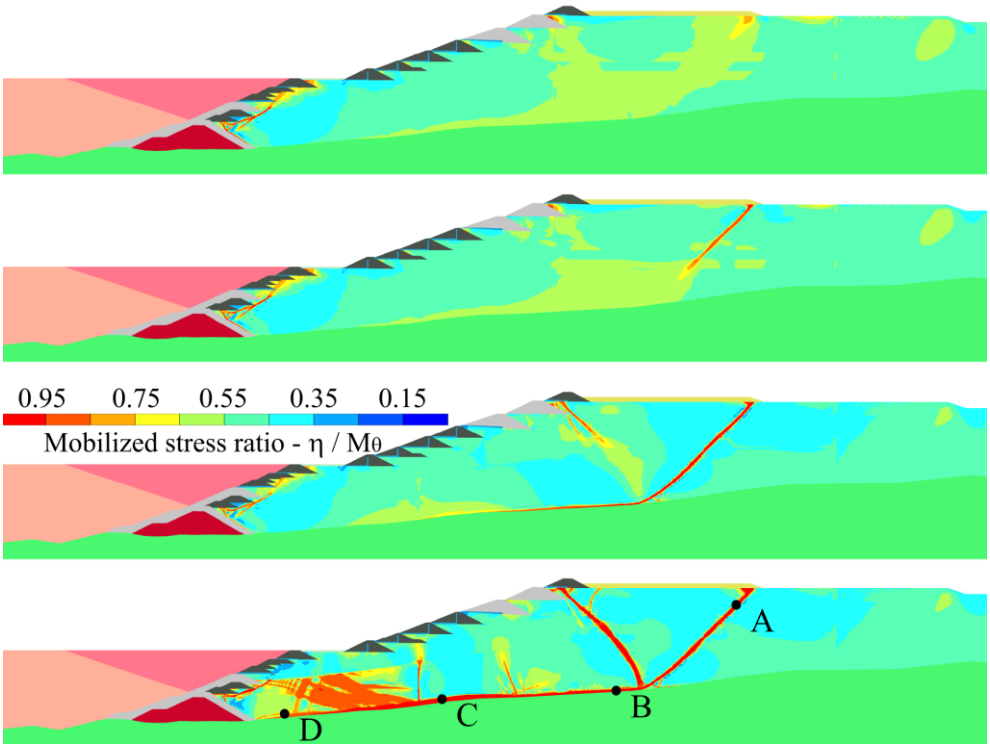

Figure 7.21 - Numerical results for buttress at elevation 899.0 m follow by excavation: mobilized stress ratio.

The minimum buttress height that allowed excavation without triggering failure was 910.0 m. The results are presented in Figure 7.22 and Figure 7.23. It is observed that the tailings continue to be mobilized in the initial excavation stage (Stage 10); however, the counterbalancing effect provided by the buttress prevents failure propagation, maintaining model stability and achieving convergence. In the subsequent stages, the tailings undergo unloading, with predominantly expansive vertical displacements due to material removal.

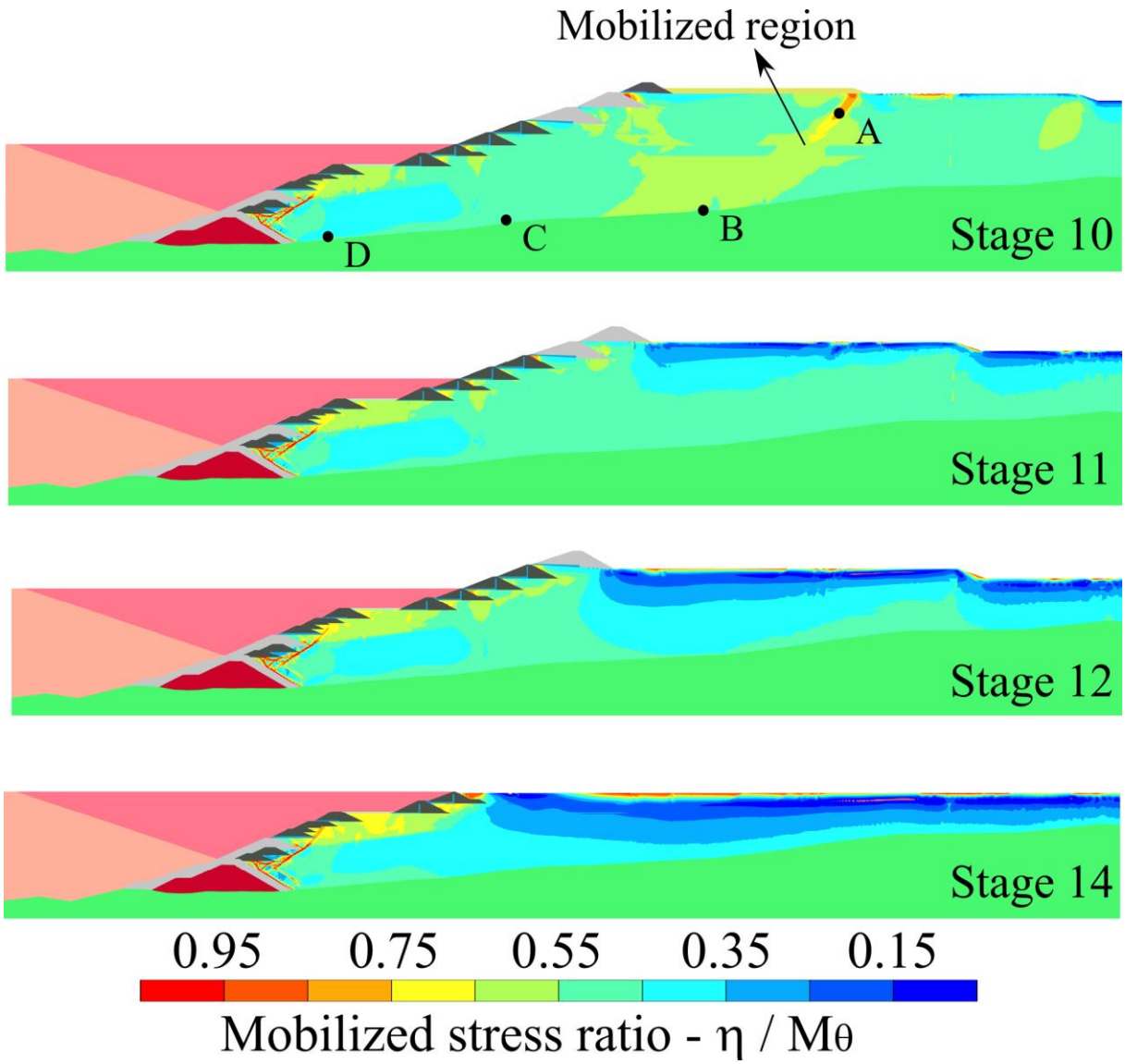

Figure 7.22 - Numerical results for buttress at elevation 910.0 m follow by excavation: mobilized stress ratio.

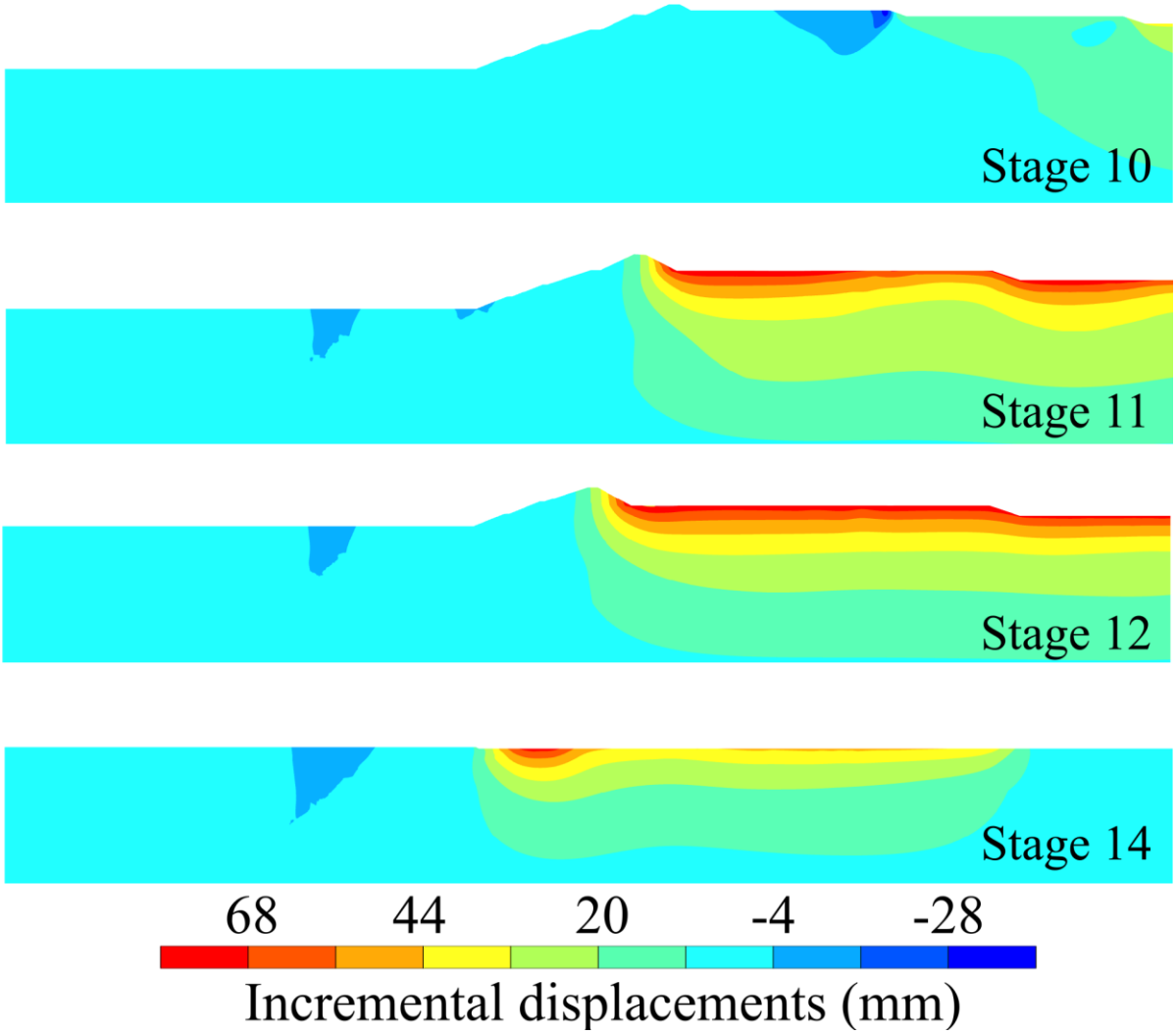

Figure 7.23 - Numerical results for buttress at elevation 910.0 m follow by excavation: vertical displacements per stage. Of note, negative values mean settlement.

Stress paths were recorded at control points, as shown in Figure 7.21 and Figure 7.22, and the results are illustrated in Figure 7.24. The results for the buttress up to an elevation of 899.0 m are designated as M2 (Model 2), while those for the buttress at 910.0 m are represented as M3 (Model 3). For comparison purposes, the results for excavation without a buttress under undrained conditions (Section 7.2.3) were also included, designated as M1 (Model 1).

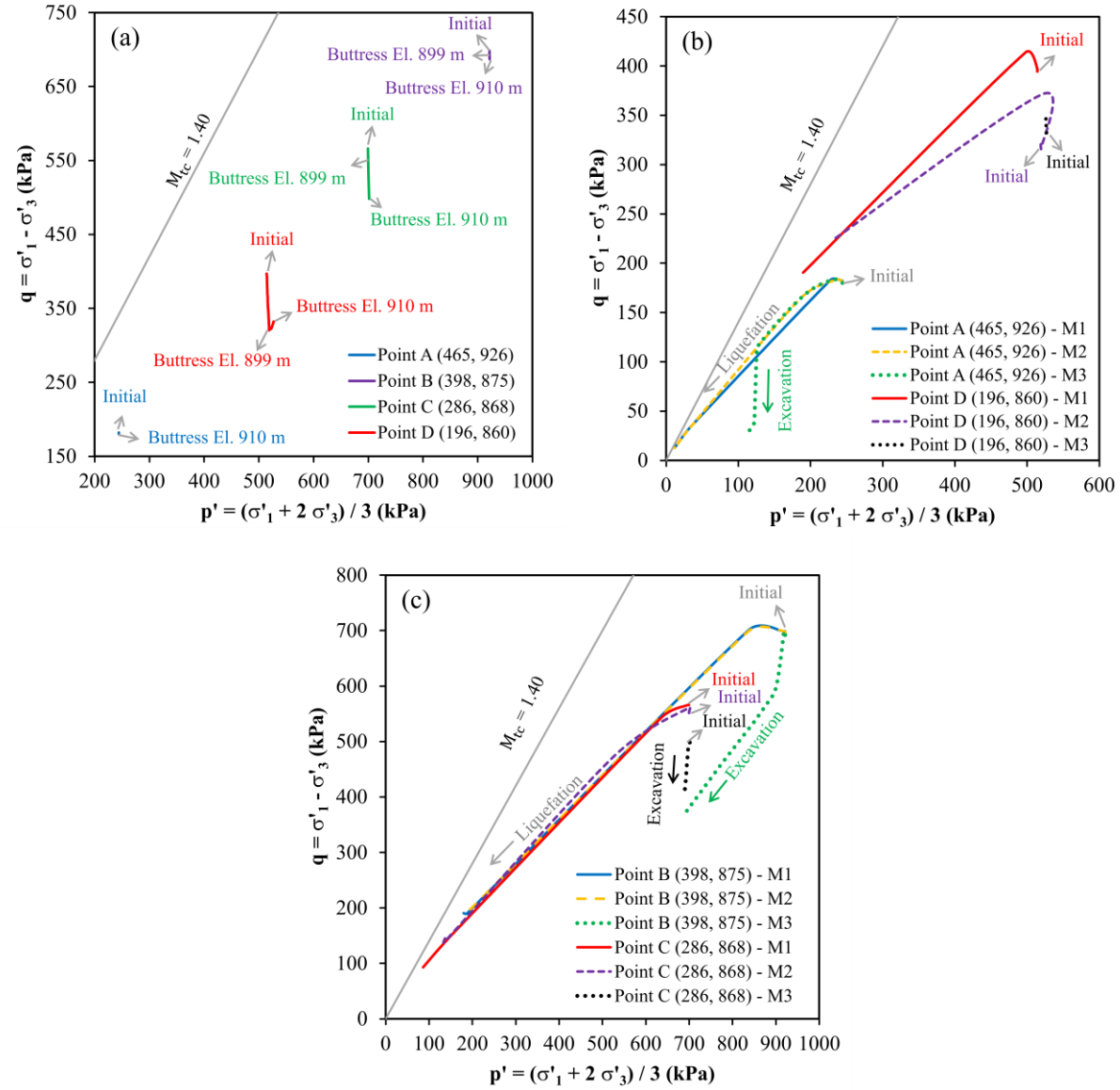

Figure 7.24 - Local soil response for de-characterization by buttress and excavation: (a) buttress stages; (b) and (c) excavation stages. Notably, M1 refers to excavation without a buttress, M2 to a buttress at elevation 899 m, and M3 to a buttress at elevation 910 m. Representative points are located on the failure surface (see Figure 7.21 and Figure 7.22). The coordinates of the points, in meters, are indicated in the plot legends.

8 - CONCLUSIONS

In this work, the influence of the constitutive model on assessing the liquefaction susceptibility of upstream-raised tailings dams, as well as the effectiveness of different decharacterization strategies, was investigated.

For this purpose, the CASM and NorSand models were applied to analyze a tailings dam failure. Initially, the model was calibrated for pre-failure conditions, and the stress state was defined through a simulation of the construction process using CASM. Subsequently, a back-analysis of the failure was carried out, simulating the static liquefaction triggering due to a borehole. Other analyses were performed by simulating hypothetical triggers: crest loading and gravity increase. The influence of the adopted constitutive model was analyzed through the generated failure mechanisms, stress paths, and levels of disturbances necessary to trigger liquefaction.

The calibrated model was then used to investigate various decharacterization strategies were simulated to assess their implications for dam stability and identify the most suitable approach that minimizes structure disturbances.

The primary questions this work seeks to address are:

- **Question 1:** How does the choice of constitutive model influence the analysis?
- **Question 2:** Would it be possible to implement a decharacterization strategy without triggering static liquefaction failure?
- **Question 3:** What impact does time have on the triggering mechanisms during decharacterization?

From the simulations conducted to answer question 01, it is observed that both analyzed constitutive models yielded failure mechanisms consistent with field observations in the scenario where the liquefaction was triggered by borehole investigation. Minor disturbances proved sufficient to initiate liquefaction-induced failure, underscoring the dam's unstable condition.

The dam loading simulation represents a potential dam raise. Both models produced a global failure, with a similar failure surface predominantly passing through the region with mobilized stresses in the pre-failure stage. This result shows that the initial stress state indicates the regions prone to liquefaction development.

The simulations of the increase in gravity allow for a thorough examination of the most vulnerable liquefaction zones. The initiation of the mechanism primarily occurred within the fine tailings, underscoring the pivotal role of these layers in the initiation and propagation of liquefaction.

The hypothetical triggers tested served to estimate safety factors based on the critical height of the dam and the increase in gravity, which ranged between 1.05 and 1.10. These results confirm the critical condition of the dam under the hypothesis of a liquefaction trigger occurrence. These safety factors are intended to assess the vulnerability of the structure; they should not be interpreted as equivalent to other traditional methodologies to assess safety factors.

Comparing the results obtained with the CASM and NorSand models, it is possible to observe that NorSand requires slightly more pronounced disturbances to activate the failure mechanism. These results could be associated with variations in residual undrained strength, which are linked to differences in state parameters. However, it should be noted that the differences in triggering were not significant, possibly because both calibrations captured similar instability lines.

Despite the different peak and residual strengths observed throughout the monitored stress paths, which are due to the calibrations used in the analyses, both models produced compatible failure mechanisms across all scenarios. The results obtained from the tailings dam failure indicate that the most important constitutive aspect in assessing structures susceptible to static liquefaction lies in the constitutive model's capacity to represent the sudden strength loss due to pore pressure generation, while the specific formulations employed tend to affect the analysis to a lower degree. This conclusion aligns with the findings of Liu et al. (2024) for the Fundão dam, suggesting potential for a broader generalization.

Given the inherent uncertainties associated with constraining the actual materials behaviors and parameters in the field, the differences observed in the overall responses of the models to the different constitutive models are well within an acceptable range. In the authors' opinion, this showcases for the first time that either constitutive model can be used without influencing trigger analyses results significantly, as the same triggers were developed using two different constitutive models, which were calibrated in different ways. This has important implications to tailings dams safety assessment, freeing the analyst from the burden of experimenting with multiple models, and allowing them to focus on better site and materials

characterization. Despite the similarities observed during trigger simulations, it is important to recognize that NorSand has limitations when applied to construction simulations due to its limited control of geostatic stress paths. Nonetheless, NorSand has been validated in various forensic analyses of dam failures, and, as a result, it is available in most commercial software.

Four main decharacterization strategies were also analyzed to answer question 02: buttressing with stabilizing fill and backfill (both with and without simultaneity), reservoir excavation, and a combined buttress-excavation approach. The analyses were conducted under both undrained and hydromechanical coupling conditions, allowing for the assessment of the time effect on the decharacterization process and addressing question 03.

Undrained analyses represent extreme and potentially conservative scenarios, especially considering the scale of the works required for decharacterization. When hydromechanical coupling analyses were considered, all interventions proved feasible, even when applying construction rates higher than those achieved in practice.

Although it represents an extreme condition, the undrained analysis is valuable for identifying the most favorable strategies. The simultaneous execution of stabilizing fill and backfill, as well as the hybrid buttress-excavation solution, demonstrated superior performance, as they did not trigger the liquefaction mechanism, even under these extreme conditions.

In contrast, the non-simultaneous buttress and the isolated reservoir excavation strategy resulted in the development of the static liquefaction mechanism. Static liquefaction induced by the construction of a buttress is consistent with real failures, such as the Cadia dam failure Jefferies et al. (2019). However, there are no historical records of failures caused exclusively by reservoir excavation, highlighting the need for future research using physical models to investigate this scenario further.

Regarding the buttress, the backfill contributes to the confinement of the tailings, ensuring stability even in areas where localized liquefaction may occur. Regarding excavation, the initial stages represented the most critical phase of the process. For the excavation strategy to be viable under undrained conditions, adequate buttressing is essential, providing significant confinement at the structure's base.

The results of this study emphasize the importance of considering transient analyses when evaluating decharacterization strategies for tailings dams. Implementing buttresses and a detailed assessment of loading conditions can minimize the risk of triggering liquefaction and ensure structural safety during interventions.

The authors acknowledge that the conclusions drawn in this study are limited to the case adopted. To enable broader generalization, further research is needed to better understand the influence of different decharacterization strategies and the impact of varying execution rates on liquefaction triggering. Future studies should investigate additional cases with diverse geometric and geological conditions, and physical modeling should be employed to validate the mechanisms observed in numerical analyses. As decharacterization projects advance, monitoring data will support the evaluation of applied strategies. Moreover, we recommend that future research include statistical comparisons, involve a wider range of constitutive models, and test them against a broader set of well-documented failure cases. Additionally, the spatial variability of tailings within the reservoir is recognized as a critical factor influencing dam behavior, but it was beyond the scope of this study and should be addressed in future work. These efforts will help extend and solidify the conclusions presented in this work.

Finally, it is emphasized that the objective of this study was to enhance the understanding of numerical simulations in representing the phenomenon of static liquefaction. Thus, the research does not aim to determine the cause of the rupture in the case study used as a basis, nor does it question the analyses previously conducted by Arroyo and Gens (2021) and Robertson et al. (2019). It is also noted that the authors do not make any judgment regarding whether the presented models accurately represent the actual conditions of the dam before and during the rupture.

8.1 - SUGGESTIONS FOR FUTURE RESEARCH

As suggestions for future work, the following are proposed:

- Investigate other cases with different geometric and geological conditions to broaden generalization;
- Investigate the spatial variability of tailings properties within the dam reservoir to better understand its impact on stability and deformation behavior;
- Study the influence of varying execution rates in decharacterization strategies on liquefaction triggering;
- Develop and use physical models to validate the mechanisms observed in numerical analyses;
- Collect and analyze monitoring data from decharacterization projects as they progress to evaluate the performance of applied strategies;
- Test a broader range of constitutive models, beyond CASM and NorSand;

- Compare results against a larger set of well-documented tailings dam failures to improve generalization;
- Investigate the liquefaction potential associated with reservoir excavation alone, using physical modeling;
- Analyzing dynamic triggers caused by equipment operations during the decharacterization process;
- Application of the Discrete Element Method to model liquefaction at field scale;
- Modeling the run-out of dam failures using large-strain methods, such as Smoothed Particle Hydrodynamics (SPH) and the Material Point Method (MPM).

REFERENCES

ADAMO, N., AL-ANSARI, N., SISSAKIAN V. K., & LAUE, J. (2020). Dam Safety: The Question of Tailings Dams. Journal of Earth Sciences and Geotechnical Engineering, 11(1): 1-26.

ANCOLD. (2019). Australian National Committee on Large Dams - Guidelines on tailings dams– planning, design, construction, operation and closure—revision 1.

ANM (2022). National Mining Agency Law N. 95.20 - Consolidates the normative acts that provide for the safety of mining dams (in Portuguese). Technical Report. URL: https://www.gov.br/anm/pt-br/assuntos/barragens/legislacao/resolucao-no-95-2022.pdf.

ARROYO, M. & GENS, A. (2021). Computational Analyses of Dam I Failure at the Córrego de Feijão Mine in Brumadinho - Final Report. Technical Report. Independent Technical Review Board.

BAECHER, G. (1987). Error analysis for geotechnical engineering. Final Report Nexus Associates, Wayland, MA.

BEEN, K. & JEFFERIES, M.G. (1985). A state parameter for sands. Géotechnique, 35(2), 99–112.

BEER, G. & WATSON, J. O. (1994). Introduction to finite and boundary element methods for engineers. West Sussex, England: John Wiley & Sons Ltd.

BEDIN, J., SCHNAID, F., VIANA DA FONSECA, A. & COSTA FILHO, L.M. (2012). Gold tailings liquefaction under critical state soil mechanics. Géotechnique 62, 263–267.

BIOT, M. A. (1941). General theory of three-dimensional consolidation, Journal of Applied Physics, vol. 12, no. 2, pp. 155–164.

BORJA, R.I. (2006). Condition for liquefaction instability in fluid-saturated granular soils. Acta Geotechnica 1.

BRINKGREVE, R.B.J., KUMARSWAMY, S., SWOLFS, W.M., ENGIN, E., FONSECA ARÉVALO, F., RAGI MANOJ, N., ZAMPICH, L. & ZALAMEA, N. (2020). Plaxis Connect Edition V20.03 Manuals. Bentley Systems.

CACCIUTTOLO, C. & VALENZUELA, F. (2022). Efficient Use of Water in Tailings Management: New Technologies and Environmental Strategies for the Future of Mining. Water. 14. 1741.

CARVALHO, F.P. (2017). Mining industry and sustainable development: time for change. Food and Energy Security; 6(2): 61–77

CASAGRANDE, A. (1936). Characteristics of cohesionless soils affecting the stability of earth fills. Journal of Boston Society of Civil Engineers, 23, 257–276.

CASTONGUAY, V. & KONRAD, J.M. (2016). Prediction of the fraser river sand response to oedometric loading using the norsand soil model. 69th Canadian Geotechnical Conference.

CHEN, J., HAWLADER, B., ROY, K. & PIKE, K. (2023). Comparison of local and nonlocal regularization approaches in eulerian-based finite element analyses. Computers and Geotechnics 162, 105617.

CHU, J. & LEONG, W. (2002). Effect of fines on instability behaviour of loose sand. Geotechnique 52, 751–755.

CIRONE, A. (2020). Theory and implementation of constitutive models for geomaterials. Thesis, Publication 50647, Pontifícia Universidade Católica do Rio de Janeiro - PUC-RIO, Rio de Janeiro, RJ, 164 p.

CONSOLI, N.C., DE AZAMBUJA CARVALHO, J.V., WAGNER, A.C., SCHEUERMANN FILHO, H.C., CARVALHO, I., CACCIARI, P.P. & DE SOUSA SILVA, J.P. (2024). Determination of critical state line (CSL) for silty-sandy iron ore tailings subjected to low-high confining pressures. Journal of Rock Mechanics and Geotechnical Engineering 16, 1684–1695.

COSTA, F., DELGADO, B. & CASTILHO, B. (2023). Numerical sensitivity analysis for stress-strain simulation and flow liquefaction assessment of tailings storage facilities using the NorSand constitutive model. Soils and Rocks 47.

VIANA DA FONSECA, A., CORDEIRO, D., MOLINA GÓMEZ, F., BESENZON, D., FONSECA, A. & FERREIRA, C. (2022). The mechanics of iron tailings from laboratory tests on reconstituted samples collected in post-mortem dam I in Brumadinho. Soils and Rocks 45, 1–20.

VICK, S. G. (1990). Planning, Design, and Analysis of Tailings Dams. BiTech Publishers Ltd. Vancouver, Canadá, 369 p.

FÁVERO, A. H., OLIVEIRA, G. R. A., RASMUSSEN, L. L., RÓGENES, E. (2025). Large Deformation and Critical State Analysis of the Fundão Tailings Dam. Geoextreme, California, United States of America.

FOURIE, A., VERDUGO, R., BJELKEVIK, A., TORRES-CRUZ, L. A., ZNIDARCIC, D. & (2022). 20ICSMGE state of the art - tailings. 20th International Conference on Soil Mechanics and Geotechnical Engineering.

GOMES, A. S. (2022). Analysis of static liquefaction triggers in a tailing dam. Master Thesis, University of Brasilia – UnB.

GOMES, A. S., CORDAO-NETO, M., FARIAS, M. M. & RÓGENES, E. (2022). Calibration of the NorSand constitutive model for tailings dam decommissioning analysis. Proceedings of the Brazilian Congress on Soil Mechanics and Geotechnical Engineering - COBRAMSEG 22.

GOMES, A.S., RÓGENES, E., CRUZ, F., PAES, P. & FÁVERO NETO, A. (2024). A parameter calibration methodology for the clay and sand model (CASM) constitutive model. Proceedings of the Tailings and Mine Waste Conference 2024.

HODGE, R.A., ERICSSON, M., LÖF, O. (2022). The global mining industry: corporate profile, complexity, and change. Miner Econ 35, 587–606.

HU, C.M., YUAN, Y.L., MEI, Y., WANG, X.Y. & LIU, Z. (2019). Modification of the gravity increase method in slope stability analysis. Bulletin of Engineering Geology and the Environment 78, 4241–4252.

ISHIHARA, K. (1993). Liquefaction and flow failure during earthquakes. Géotechnique 43, 351–451.

ITASCA. (2019). FLAC Version 8.1 Manuals. Itasca Consulting Group, Inc.

JEFFERIES, M. (1993). Nor-sand: a simple critical state model for sand. Geotechnique 43, 91–103.

JEFFERIES, M. & BEEN, K. (2015). Soil Liquefaction: A Critical State Approach, Second Edition.

JEFFERIES, M., MORGENSTERN, N.R., ZYL, D.V. & WATES, J. (2019). Report on NTSF Embankment Failure Cadia Valley Operations for Ashurst Australia. Technical Report. International Centre for Numerical Methods in Engineering.

JEFFERIES, M. & SHUTTLE, D. (2005). Norsand: Features, calibration and use. Geotechnical Special Publication, 204–236.

KRAMER, S.L. (1996). Geotechnical Earthquake Engineering. Prentice Hall, Upper Saddle River, New Jersey, USA.

LADE, P. & PRADEL, D. (1990). Instability and plastic flow of soils. i: Experimental observations. Journal of Engineering Mechanics-ASCE - J ENG MECH-ASCE 116.

LADE, P. & YAMAMURO, J. (2011). Evaluation of static liquefaction potential of silty sand slopes. Canadian Geotechnical Journal 48, 247–264.

LEDESMA, O., MANZANAL, D. & SFRISO, A. (2021). Formulation and numerical implementation of a state parameter-based generalized plasticity model for mine tailings. Computers and Geotechnics 135, 104158.

LEDESMA, O., SFRISO, A. & MANZANAL, D. (2022). Procedure for assessing the liquefaction vulnerability of tailings dams. Computers and Geotechnics 144, 104632.

LALOUI, L. & LORIA, A. R. (2020). Deformation in the context of energy geostructures. 10.1016/B978-0-12-816223-1.00004-7.

LI, L., TANG, C., ZHU, W. & LIANG, Z. (2009). Numerical analysis of slope stability based on the gravity increase method. Computers and Geotechnics 36, 1246–1258.

LIU, H., NAGULA, S., PETTER JOSTAD, H., PICIULLO, L. & NADIM, F. (2024). Considerations for using critical state soil mechanics based constitutive models for capturing static liquefaction failure of tailings dams. Computers and Geotechnics 167, 106089.

LYU, Z., JUNRUI, C., ZENGGUANG, X., QIN, Y. & CAO, J. (2019). A comprehensive review on reasons for tailings dam failures based on case history. Advances in Civil Engineering 2019, 1–18.

LÜ, X., HUANG, M. & ANDRADE, J.E. (2017). Predicting the initiation of static liquefaction of cross-anisotropic sands under multiaxial stress conditions. International Journal for Numerical and Analytical Methods in Geomechanics 41, 1724–1740.

MARAIS, L., KEMP, D., VAN DER WATT, P., MATEBESI, S., CLOETE, J., HARRIS, J., ERN, M. A. L. & OWEN, J. R. (2024). The catastrophic failure of the Jagersfontein tailings dam: An industrial disaster 150 years in the making, International Journal of Disaster Risk Reduction, 109,104585.

MARTIN, T. & MCROBERTS, E. (1999). Some considerations in the stability analysis of upstream tailings dams. Tailings and Mine Waste, Proceedings 13th International Conference On Tailings and Mine Waste.

MOFRAD, M., POURAGHA, M. & SIMMS, P. (2023). Constitutive modelling of unsaturated gold tailings subjected to drying and wetting cycles. International Journal for Numerical and Analytical Methods in Geomechanics 47, 1936–1949.

MORGENSTERN, N.R., VICK, S.G., VIOTTI, C.B. & WATTS, B.D. (2016). Fundão tailings dam review panel: Report in the Immediate Causes of the Failure of the Fundão Dam. Technical Report. Cleary Gottlieb Steen & Hamilton LLP.

MORGENSTERN, N. R., VICK., S. G. & ZYL, D.V. (2015). Report on Mount Polley Tailings Storage Facility Breach. Technical Report. Independent Expert Engineering Investigation and Review Panel.

MÁNICA, M., ARROYO, M., GENS, A. & MONFORTE, L. (2021). Application of a critical state model to the Merriespruit tailings dam failure. Geotechnical Engineering 175.

MÁNICA, M.A., GENS, A., VAUNAT, J. & RUIZ, D.F. (2018). Nonlocal plasticity modelling of strain localisation in stiff clays. Computers and Geotechnics 103, 138–150.

NAZARETH, M., CIRONE, A., PAES, I., RÓGENES, E.S.S., RASMUSSEN, L. L., & Delgado., B. (2025). CASM model: strength, instability line, and brittleness index in undrained triaxial compression. Canadian Geotechnical Journal. 62: 1-11. https://doi.org/10.1139/cgj-2025-0011

NEVES, A.C. & FELITTI,W. (2024). The importance of hydrogeological models for closure of tailings dams. Proceedings of the Tailings and MineWaste Conference 2024 , 1439–1450.

NG, C.W., CROUS, P.A., ZHANG, M. & SHAKEEL, M. (2022). Static liquefaction mechanisms in loose sand fill slopes. Computers and Geotechnics 141, 104525.

OLSON, S.M. & STARK, T.D. (2003). Yield strength ratio and liquefaction analysis of slopes and embankments. Journal of Geotechnical and Geoenvironmental Engineering 129, 727–737.

ORESKES, N., SHRADER-FRECHETTE, K. & BELITZ, K. (1994). Verification, validation, and confirmation of numerical models in the earth sciences. Science 263, 641–646. URL: https://www.science.org/doi/abs/10.1126/science.263.5147.641.

OWEN, J., KEMP, D., LEBRE, E., SVOBODOVA, K. & MURILLO, G.P. (2020). Catastrophic tailings dam failures and disaster risk disclosure. International Journal of Disaster Risk Reduction 42, 101361.

PEREIRA, M.P.C., ALMEIDA, M.T.d.S.d., COSTA, C.S.R., CASTRO, H.M.C., AGUILAR, F.P. & VICENTE, M. (2024). Decharacterization of tailings and sediment dams in brazil – hydrological and hydraulic aspects. Proceedings of the Tailings and Mine Waste Conference 2024 , 1419–1428.

PICIULLO, L., STORROSTEN, E.B., LIU, Z., NADIM, F. & LACASSE, S. (2022). A new look at the statistics of tailings dam failures. Engineering Geology 303, 106657.

REID, D., DICKINSON, S., FANNI, R., FOURIE, A. & MITAL, U. (2023). Discussion of "procedure for assessing the liquefaction vulnerability of tailings dams" by Ledesma, O, Sfriso, A, and Manzanal, D. Computers and Geotechnics 153, 105062.

REID, D., DICKINSON, S., MITAL, U., FANNI, R. & FOURIE, A. (2022). On some uncertainties related to static liquefaction triggering assessments. Proceedings of the Institution of Civil Engineers - Geotechnical Engineering 175, 1–53.

REID, D. & FOURIE, A. (2024). Development and outcomes of a tailings slope stability comparative design exercise. Canadian Geotechnical Journal 61, 1683–1704.

ROBERTSON, P.K., DE MELO, L., WILIAMS, D.J. & WILSON, G.W. (2019). Report of the expert panel on the technical cause of the failure of Feijão Dam I. Technical Report.

RÓGENES, E., PAES, I.T., DELGADO, B.G., BITTAR, R.J., GOMES, A.d.S., CIRONE, A., FÁVERO NETO, A.H. & RASMUSSEN, L.L. (2024b). Assessing Static Liquefaction Triggers in Tailings Dams Using the Critical State Constitutive Models CASM and NorSand. Int J Numer Anal Methods Geomech.

RÓGENES, E., PAES, I., DELGADO, B.G., GOMES, A.d.S., CRUZ, F., LANZIERI, D., FÁVERO NETO, A. & RASMUSSEN, L.L. (2024a). Plaxis and CASM: formulation, implementation, and verification. Proceedings of the Tailings and Mine Waste Conference 2024.

ROSCOE, K., SCHOFIELD, A.N. & WROTH, C.P. (1958). On the yielding of soils. Géotechnique, 8(1), 22–53.

SADREKARIMI, A. (2014). Static liquefaction-triggering analysis considering soil dilatancy. Soils and Foundations 54, 955–966.

SANTAMARINA, J., TORRES-CRUZ, L.A. & BACHUS, R. (2019). Why coal ash and tailings dam disasters occur. Science 364, 526–528.

SCHOFIELD, A. & WROTH, C.P. (1968). Critical State Soil Mechanics. London, U.K.: McGraw-Hill.

SCHANZ, T., VERMEER, P. & BONNIER, P. (1999). Formulation and verification of the hardening-soil model. Beyond 2000 in Computational Geotechnics.

SCHAPER, D., LESSA, R., FREITAS, A., WEEKS, B. (2021). De-characterization and closure of tsf: concepts of the brazilian legislation and international criteria .

SHENG, D., SLOAN, S.W. & YU, H.S. (2000). Aspects of finite element implementation of critical state models. Computational Mechanics 26, 727–737.

SHUTTLE, D. & JEFFERIES, M. (2010). Norsand: description, calibration, validation and applications.

SHUTTLE, D. & JEFFERIES, M. (2016). Determining silt state from cptu. Geotechnical Research 3, 90–118.

SHUTTLE, D., MARINELLI, F., BRASILE, S. & JEFFERIES, M. (2022). Validation of computational liquefaction for tailings: Tar island slump. Geotechnical Research 9, 32–55.

SILVA, J.P.S., RISSOLI, A.L.C., CACCIARI, P.P., VIANA DA FONSECA, A.J.P., SCHEUERMANN FILHO, H.C., WAGNER, A.C., de AZAMBUJA CARVALHO, J.V., FESTUGATO, L. & CONSOLI, N.C. (2024). Triaxial testing response of compacted iron ore tailings considering a broad spectrum of confining pressures. Soils and Foundations 64, 101438.

SLOAN, S. W.; ABBO, A. J.; SHENG, D. (2001). Refined explicit integration of elastoplastic models with automatic error control. Engineering Computations, 18(1/2):121–194.

SOTTILE, M., CUETO, I., SFRISO, A., LEDESMA, O. & LIZCANO, A. (2021). Flow liquefaction triggering analyses of a tailings storage facility by means of a simplified numerical procedure. Proceedings of the 20th International Conference on Soil Mechanics and Geotechnical Engineering.

SUN, Z., CHU, J. & XIAO, Y. (2021). Formulation and implementation of an elastoplastic constitutive model for sand-fines mixtures. International Journal for Numerical and Analytical Methods in Geomechanics 45, 2682–2708.

VALE (2024a). Quarterly report period: august to october 2024 - Forquilha I dam, (accessed 19/02/2025. Technical Report. URL: https://vale.com/pt/programa-de-descaracteriza%C3%A7%C3%A3o.

VALE (2024b). Quarterly report period: august to october 2024 - Forquilha III dam. Technical Report. URL: https://vale.com/pt/programa-de-descaracteriza%C3%A7%C3%A3o.

VALE (2024c). Quarterly report period: august to october 2024 - Grupo dam. Technical Report. URL: https://vale.com/pt/programa-de-descaracteriza%C3%A7%C3%A3o.

VALE (2025). Decharacterization program (accessed 19/02/2025). URL: https://vale.com/pt/programa-de-descaracteriza%C3%A7%C3%A3o.

VERGARAY, L., MACEDO, J. & ARNOLD, C. (2023). Static and cyclic liquefaction of copper mine tailings. Journal of Geotechnical and Geoenvironmental Engineering 149, 04023021.

VICK, S. G. (1990). Planning, Design, and Analysis of Tailings Dams. BiTech Publishers Ltd. Vancouver, Canadá, 369 p

WAGNER, A.C., DE SOUSA SILVA, J.P., DE AZAMBUJA CARVALHO, J.V., CEZAR RISSOLI, A.L., CACCIARI, P.P., CHAVES, H.M., SCHEUERMANN FILHO, H.C. & CONSOLI, N.C. (2023). Mechanical behavior of iron ore tailings under standard compression and extension triaxial stress paths. Journal of Rock Mechanics and Geotechnical Engineering 15, 1883–1894.

WHITTLE, A., EL-NAGGAR, H., AKL, S. & ABDELAAL, A. (2022). Stability analysis of upstream tailings dam using numerical limit analyses. Journal of Geotechnical and Geoenvironmental Engineering 148.

WILLIAMS, D. (2021). Lessons from Tailings Dam Failures—Where to Go from Here?. Minerals. 11. 853.

WOOD, D.M. (1990). Soil Behaviour and Critical State Soil Mechanics. Cambridge University Press.

WOOD, D.M. (2017). Geotechnical Modelling. CRC Press.

YOSHIMINE, M., ROBERTSON, P. & WRIDE, C. (1999). Undrained shear strength of clean sands to trigger flow liquefaction. Canadian Geotechnical Journal - CAN GEOTECH J 36, 891–906.

YU, H.S. (1998). CASM: a unified state parameter model for clay and sand. International Journal for Numerical and Analytical Methods in Geomechanics 22, 621–653.

YU, H.S. (2006). Plasticity and geotechnics. New York: Springer.

ZHU, M., GONG, G., XIA, J., LIU, L. & WILKINSON, S. (2021). Effects of deviator strain histories on liquefaction of loose sand using dem. Computers and Geotechnics 136, 104213.